FREE-STANDING EPITAXIAL GRAPHENE ON SILICON CARBIDE AND TRANSPORT BARRIERS IN LAYERED MATERIALS

A Dissertation

Presented to the Faculty of the Graduate School

of Cornell University

In Partial Fulfillment of the Requirements for the Degree of

Doctor of Philosophy

by

Shriram Shivaraman

August 2013

FREE-STANDING EPITAXIAL GRAPHENE ON SILICON CARBIDE AND TRANSPORT BARRIERS IN LAYERED MATERIALS

Shriram Shivaraman, Ph. D.

Cornell University 2013

This thesis is based on the topic of layered materials, in which different layers interact with each other via van der Waals forces. The majority of this thesis deals with epitaxial graphene (EG) obtained from silicon carbide (SiC). Free-standing epitaxial graphene (FSEG) structures are produced from EG using a photoelectrochemical (PEC) etching process developed for making suspended graphene structures on a large-scale. These structures are investigated for their mechanical and electrical properties. For doubly-clamped FSEG structures, a unique U-beam effect is observed which causes orders of magnitude increase in their mechanical resonance frequency compared to that expected using simple beam theory. Combined magnetotransport and Raman spectroscopy studies reveal that FSEG devices produced from nominally monolayer graphene on the Si-face of SiC exhibit properties of an inhomogeneously doped bilayer after becoming suspended. This suggests that the buffer layer which precedes graphene growth on the Si-face of SiC gets converted to a graphene layer after the PEC etching process.

In the second theme of this thesis, transport barriers in layered materials are investigated. The EG-SiC interface is studied using a combination of electrical (*I-V*, *C-V*) and photocurrent spectroscopy techniques. It is shown that the interface may be

described as having a Schottky barrier for electron transport with a Gaussian distribution of barrier heights. Another interface explored in this work is that between different layers of MoS_2, a layered material belonging to the class of transition metal dichalcogenides. This interface maybe thought of as a one-dimensional junction. Four-point transport measurements indicate the presence of a barrier for electron transport at this interface. A simple model of the junction as a region with an increased threshold voltage and degraded mobility is suggested.

The final chapter is a collection of works based on the topic of layered materials, which are not related to the main theme of the thesis. They include fabrication and characterization details of a dual-gated bilayer graphene device, an investigation of the graphene-Si interface and hexagonal boron nitride-based membranes. These are presented in the hope that they may be useful for further investigations along those directions.

BIOGRAPHICAL SKETCH

Shriram Shivaraman was born in India in 1984. He earned his B. Tech. in Electrical Engineering from the Indian Institute of Technology (IIT), Bombay in May 2006. He joined Cornell University in August 2006 for the MS/PhD program in the School of Electrical and Computer Engineering and conducted research on layered materials for his doctoral dissertation.

To my Mother, Geetha

And

The Indomitable Spirit within

ACKNOWLEDGMENTS

I would like to thank my committee chair, Prof. Michael Spencer, for giving me the opportunity to work at the Cornell Center for Materials Research (CCMR). I am grateful to him for his support and encouragement during my research. I would also like to thank my committee member Prof. Farhan Rana for his mentorship and for including me as part of his research group. He was a source of inspiration for me through his work ethic, excellent teaching and counsel. I am thankful to Prof. Paul McEuen for serving on my committee and for his advice during my various projects.

I would also like to thank Profs. Jiwoong Park, Harold Craighead, Jeevak Parpia and Dr. Bill Schaff for allowing me access to their lab facilities during my research. Thanks are also due to the facility support staff at CCMR – Prof. Kit Umbach, Jonathan Shu and Steve Kriske – and the staff at the Cornell Nanofabrication Facility. Nate, Rodney and Chris at the Physics Machine shop were very helpful in my machining projects.

I would also like to acknowledge the extremely collegial student and post-doc members of the CCMR-IRG on Atomic Membranes who collaborated with me on various projects and were extremely willing to share and learn – Jahan Dawlaty, Rob Barton, MVS Chandrashekhar, Arend van der Zande, Jonathan Alden, Lihong Herman, Virgil Shields, Wei Tsen, Robin Havener, Matt Graham, Jared Strait, Haining Wang and Wei Min Chan. I would also like to thank our collaborators at the Universität Erlangen-Nürnberg, Germany – Johannes Jobst, Daniel Waldmann and Prof. Heiko Weber – and Dr. John Boeckl at the Air Force Research Laboratory.

The work in this thesis was conducted with the support of NSF MRSEC program (DMR-1120296) and the AFOSR-MURI (Grant: FA9550-09-1-0705) and I am thankful to the funding agencies.

The acknowledgements would not be complete without thanking my dear friends in Ithaca and elsewhere who were there to share my happiness and stood by me through difficult times. Finally, I am grateful to my parents and my brother, Ravi, for their love, support and encouragement and for enabling me to get this education.

TABLE OF CONTENTS

LIST OF FIGURES

LIST OF TABLES

CHAPTER 1

INTRODUCTION

1.1 Layered Materials

This thesis is broadly based on the topic of layered materials. Layered materials are those in which separate layers interact via van der Waals forces. The prototypical layered material is graphite which consists of stacked layers of two-dimensional honeycomb lattices of carbon atoms as depicted in Figure 1.1. A single layer of graphite is called graphene. A major portion of this thesis is based upon this material.

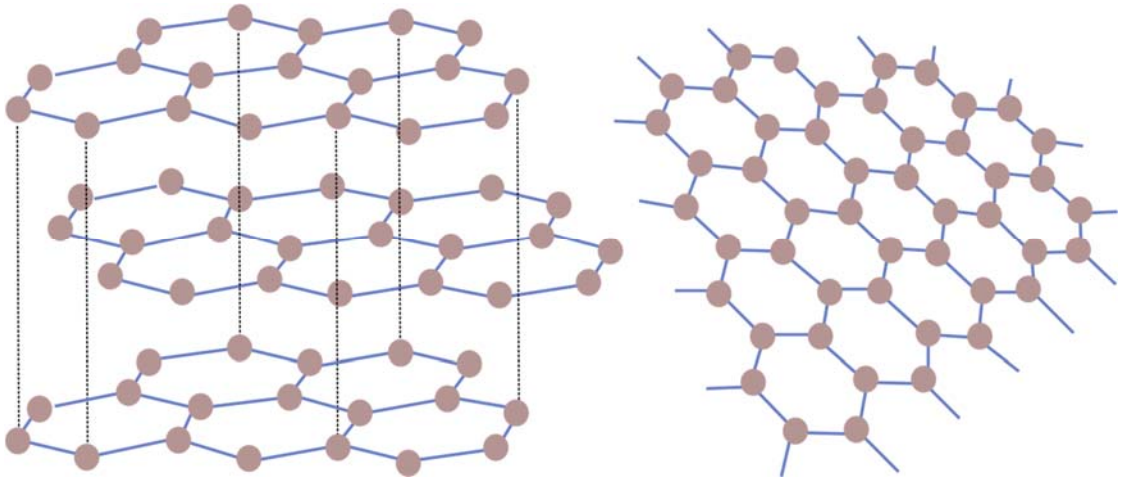

Figure 1.1: (Left) Three-dimensional graphite – the prototypical layered material. (Right) Graphene – a single layer of graphite. The different layers in graphite interact via van der Waals forces.

The other layered materials explored briefly in this thesis are hexagonal boron nitride (h-BN) and molybdenum disulfide (MoS_2). Their structures are shown in Figure 1.2(a) and Figure 1.2(b) respectively. h-BN consists of a honeycomb lattice of alternating B and N atoms, analogous to graphene. MoS_2 belongs to a class of materials called

layered transition metal dichalcogenides (LTMDs) and consists of a trigonal prismatic arrangement of Mo and S atoms inside a unit cell.

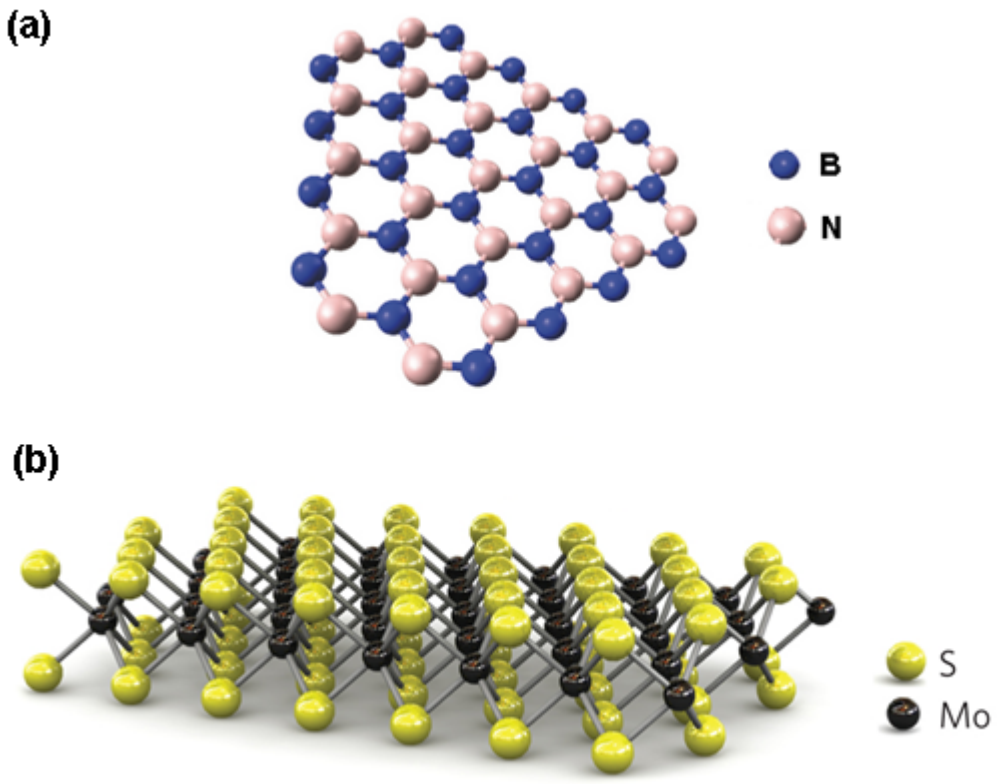

Figure 1.2: (a) Hexagonal boron nitride (Adapted from [1]) (b) Molybdenum disulfide (Adapted from [2])

1.2 Outline of the Thesis

There are two major themes in this work: (1) Free-standing epitaxial graphene (FSEG) (2) Transport barriers in layered materials. Epitaxial graphene (EG) refers to graphene grown by an epitaxial method on silicon carbide (SiC) substrates. A major contribution of this thesis is study of the mechanical and electrical properties of free-standing graphene membranes produced from this material. The second theme refers to barriers for electron transport at the interface of layered materials. In this context,

two materials systems are explored: (1) transport barrier at the interface of EG and SiC (2) transport barrier at the interface of different layers of MoS_2.

Chapter 2 gives an introduction to EG on SiC and various characterization techniques used to discern the nature and quality of the material. An approximate thickness estimation technique using Raman spectroscopy is presented. Chapter 3 outlines fabrication of FSEG doubly-clamped beams and documents study of their mechanical properties using optical interferometry and atomic force microscopy. In chapter 4, the characterization of FSEG devices using a combination of Raman spectroscopy and magnetotransport is presented. The remaining two chapters explore barriers in layered materials. Chapter 5 investigates the graphene-SiC interface using current-voltage *I-V*, capacitance-voltage *C-V* and photocurrent spectroscopy. Chapter 6 presents work documenting the presence of a transport barrier at the interface of different layers of MoS_2. Finally, in chapter 7, we present three loosely related projects on layered materials:

1. Fabrication and characterization of dual-gated bilayer graphene devices
2. Characterization of the graphene-Si interface
3. h-BN balloons

CHAPTER 2

EPITAXIAL GRAPHENE ON SILICON CARBIDE

Graphene was isolated in 2004 by the Nobel-prize winning team of Novoselov and Geim [3]. It has been the subject of intensive research because of its unique electronic [4], optical [5], thermal [6] and mechanical [7] properties. This chapter begins with a brief discussion of some of these distinctive attributes. Methods to obtain graphene are discussed next. The subsequent section focuses on epitaxial graphene (EG) on the Si and C faces of SiC. After an introduction to Raman spectroscopy for characterization of graphene, a method to estimate graphene thickness based on Raman signal intensity is discussed. Finally, electrical characterization of devices obtained from EG on SiC is presented.

2.1 Graphene: Unique properties

The crystal structure of graphene is shown in Figure 2.1(a). The unit cell consists of two carbon atoms, which may be labeled as belonging to sublattices A and B respectively. The first Brillouin zone is shown in Figure 2.1(b). It consists of two inequivalent zone corners denoted by *K* and *K'*. Figure 2.1(c) presents the electronic band structure of graphene. As indicated, the band structure near the *K* and *K'* points may be approximated by a linear dispersion relationship $E = \hbar k v_F$, where v_F is the Fermi velocity. Thus, the conduction and valence bands are degenerate at the zone corners. These special points in reciprocal space are referred to as Dirac points. In

addition, the wavefunction of graphene is a two-component vector, the elements of which denote the relative amplitudes of the wavefunction on the A and B sublattice sites. This gives rise to a unique spin-like attribute to the wavefunction and is denoted by the term "pseudospin". The pseudospin, in combination with the linear dispersion, is the basis of many exotic electronic and optical properties of graphene.

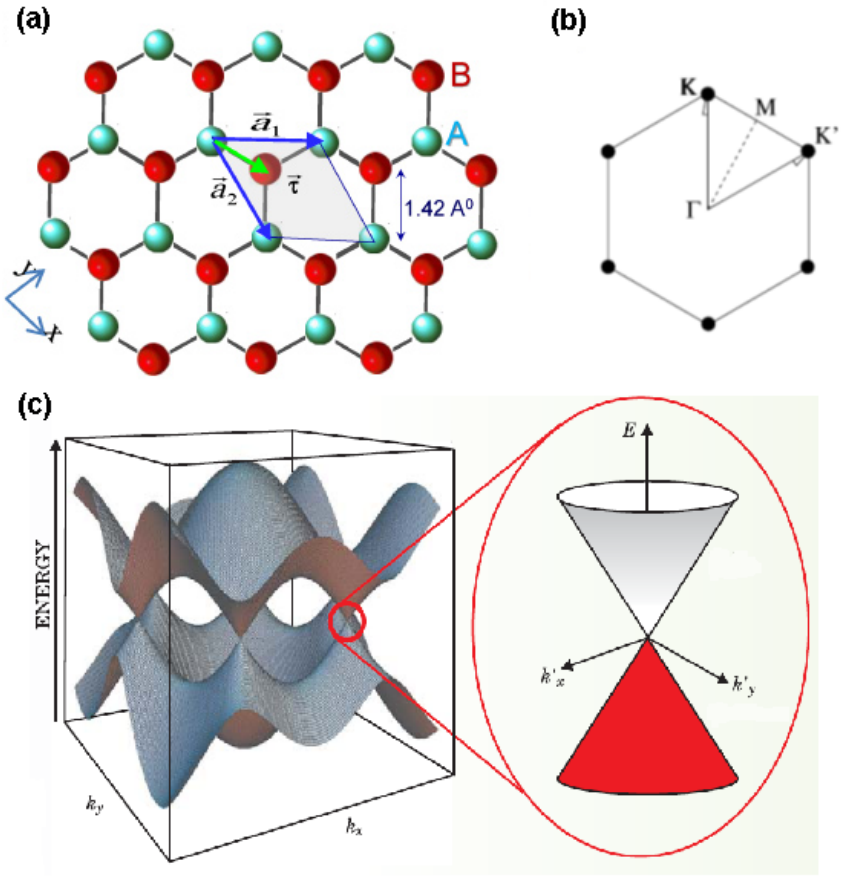

Figure 2.1: (a) Crystal structure of graphene showing A and B sublattices (Adapted from [8]). (b) First Brillouin zone of graphene. (c) Graphene bandstructure showing linear dispersion near the *K* and *K'* points (Adapted from Physics Today 2006).

The first manifestation of the extra-ordinary electronic properties of graphene is the extremely high carrier mobility. Carrier mobilities of ~15,000 $cm^2/V\text{-}s$ under

ambient conditions were reported early on in the literature [9]. These mobilities were mostly limited by charged impurities on the SiO_2/Si substrate. Further studies showed that suspended graphene [10] or graphene on hexagonal boron nitride (h-BN) substrates [11] exhibit mobilities of ~100,000 $cm^2/V\text{-}s$. Moreover, because of the Dirac points, graphene is a semi-metal and exhibits ambipolar behavior. For example, Figure 2.2 shows the resistance of graphene reaches a maximum at the Dirac point. The resistance decreases for positive and negative gate voltages as the material is electrostatically doped with electrons and holes respectively.

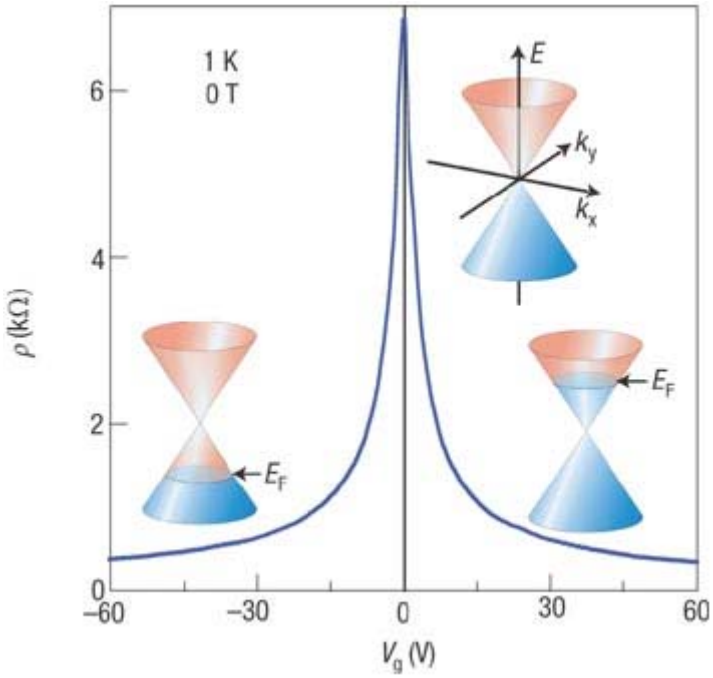

Figure 2.2: Ambipolar behavior of graphene [12]

In addition, because of the strong C – C bonds in graphene, the optical phonon energies are quite large (~0.2 eV) enabling high-field transport. Saturation velocities in graphene up to 5.5×10^7 *cm/s* at low carrier densities have been observed [13]. Also, graphene exhibits exceptional thermal conductivity $\kappa \sim 5 \times 10^3$ *W/m-K* [6],

approximately 40 times that of Si. This combined with the high current-carrying capacity of graphene (~ 1×10^8 $A\text{-}cm^{-2}$) [3] holds promise for graphene-based nanoelectronics.

The special relationship between the pseudospin and momentum of charge carriers in graphene gives rise to unique signatures in its magnetotransport. The wavefunction of the electron in graphene gains an added phase of π when the carrier completes one cyclotron orbit in a magnetic field. This is referred to as Berry's phase. This results in an unusual "half-integer" quantum Hall effect and a phase shift in the Shubnikov-de Haas oscillations (SdHO) [14,15], which are discussed in more detail in Chapter 4.

Another remarkable feature of graphene is that it is simultaneously the lightest, thinnest and strongest (Young's modulus ~1 TPa [16]) crystalline material known to man. Despite being just one atom thick, it has been shown to be impermeable to helium [17]. The small mass of graphene enables extremely sensitive nanomechanical sensors for the purposes of sensing mass or force [18]. Ultrasensitive gas sensors have also been demonstrated by modulating the conductance of graphene [19]. The ultrathin nature of graphene may additionally be exploited for its ability to act as an electron transparent support material in transmission electron microscopy studies [1].

Finally, we discuss the unique optical properties of graphene engendered by its bandstructure. The interband absorption of graphene is flat in the near infrared to visible region of the electromagnetic spectrum and is a constant 2.3% per monolayer (see Figure 2.3) [20]. This coupled with the conductive nature of graphene could lead to graphene being a potential replacement for transparent conductive oxides in

touchscreens. Secondly, the collective free carrier excitations in graphene, viz. plasmons, occur in the microwave to mid-infrared regime, which opens up possibilities in terahertz plasmonics [21].

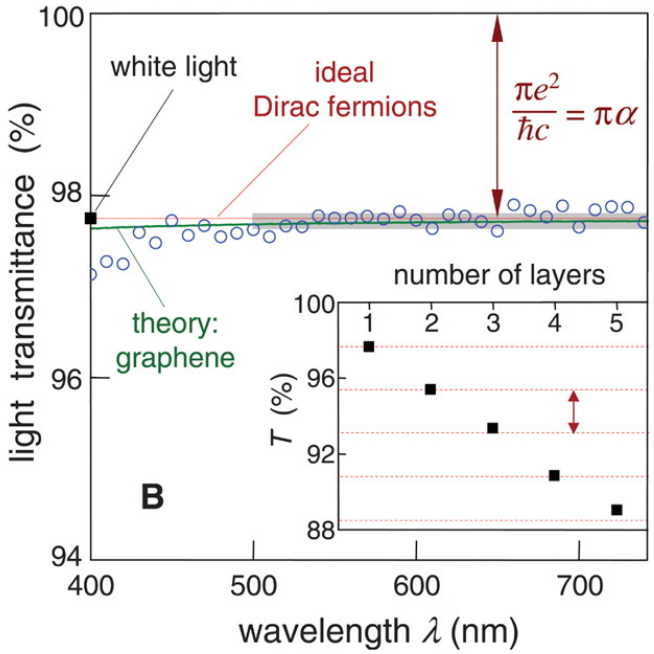

Figure 2.3: Transmission spectrum of graphene in the visible to near infrared range. Inset shows how transmission changes as a function of number of graphene layers [20]

2.2 Methods of producing graphene

In this section, a few important methods of producing graphene are dicussed.

2.2.1 Exfoliated graphene

The original work of isolating graphene employed the tedious procedure of mechanical exfoliation. In this technique, bulk graphite (in the form of kish graphite or highly oriented pyrolytic graphite) was rubbed onto scotch tape and thinned down by repeated peeling. Once sufficiently thinned down, the flakes were deposited onto a suitably oxidized silicon substrate. A significant breakthrough was recognition of the

fact that for certain thickness of the SiO_2, a monolayer of graphite could be optically detected. Figure 2.4 shows a picture of graphene deposited on 285 nm of SiO_2 obtained by the exfoliation technique. Though this technique results in high-quality films, a major disadvantage is the limited yield and the cumbersome nature of the identification process.

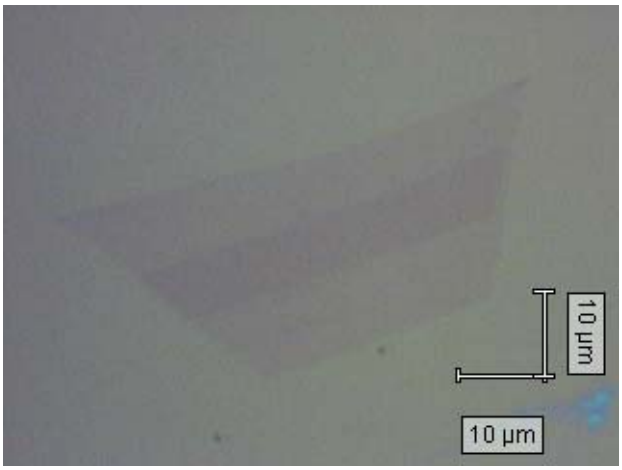

Figure 2.4: Monolayer graphene deposited on 285 nm SiO_2/Si by mechanical exfoliation. The thicker portion in the center is bilayer graphene.

2.2.2 Epitaxial graphene (EG)

2.2.2.1 EG on silicon carbide by sublimation

A promising method for large-scale production of graphene is by epitaxial growth on SiC [22-24]. This technique (see Figure 2.5) involves heating the SiC substrate under vacuum or an argon atmosphere to high temperatures in the range of 1200 ^{o}C to 1600 ^{o}C. Since the sublimation rate of silicon is higher than that of carbon, excess carbon is left behind on the surface, which rearranges to form graphene. The rest of this chapter is devoted to the growth and characterization of this material.

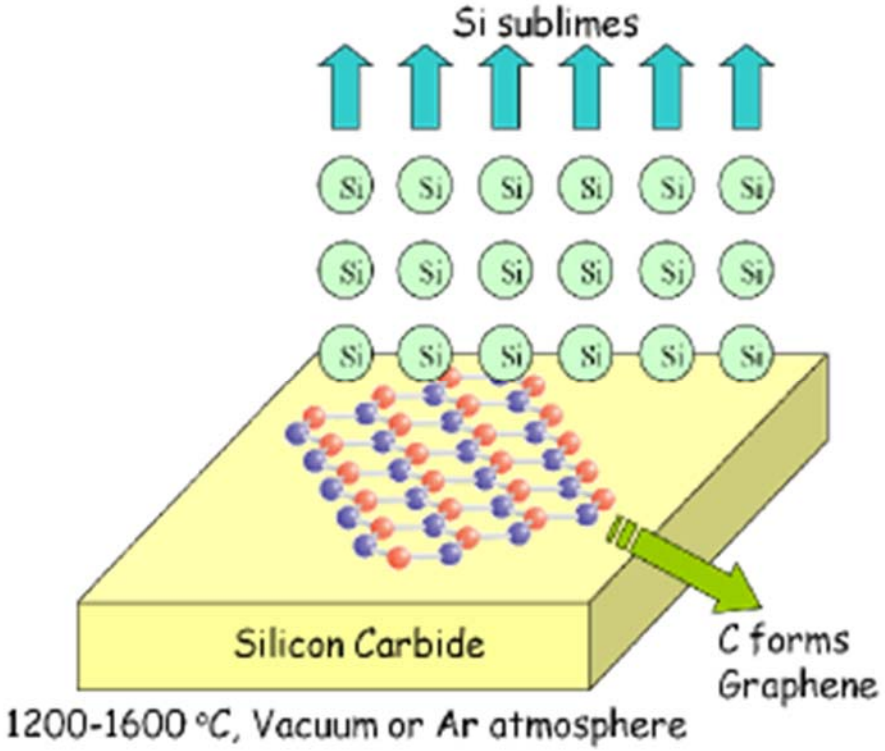

Figure 2.5: Cartoon depicting the sublimation and epitaxial growth process of graphene on SiC

2.2.2.2 EG on sapphire by chemical vapor deposition (CVD)

More recently, large area graphene has also been grown using chemical vapor deposition (CVD) on sapphire substrates using hydrogen and either propane or methane as the carbon source and argon as the carrier gas [25-27].

2.2.3 Growth of graphene on Ni/Cu by CVD

Another large scale technique to grow graphene is by chemical vapor deposition on Ni [28] or Cu [29]. This method also uses a CH_4/H_2 mixture as the carbon source. On Cu, monolayer graphene can be controllably obtained over large areas.

2.3 Epitaxial graphene on SiC

2.3.1 Growth methods

2.3.1.1 High vacuum growth of graphene

The initial experiments of growing graphene on SiC were performed under conditions of high vacuum. 4H and 6H SiC semi-insulating and n^+-/n-epitaxial substrates were used in the studies. The diced pieces were degreased in acetone and methanol and thoroughly cleaned with a CO_2 snow-gun before loading them into the sublimation chamber (see Figure 2.6(a)). No special surface treatment was employed for most of these samples. Growths were conducted under high vacuum (~ $1x10^{-6}$ – $1x10^{-5}$ torr) at temperatures ranging from 1300-1600 ºC. Films were grown on the CMP-polished C-face of semi-insulating SiC, on the CMP-polished Si-face of n^+-SiC and on the Si-face of n-type (~$3x10^{15}cm^{-3}$) epitaxial SiC.

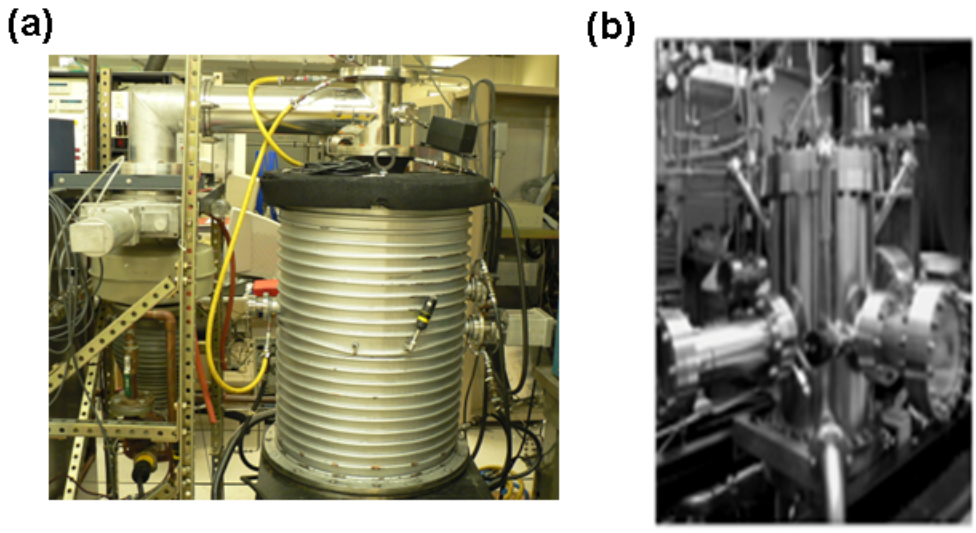

Figure 2.6: Pictures of the sublimation chamber (a) Early version (b) Later version for argon mediated growth.

2.3.1.2 Argon back-pressure mediated growth

In later stages of the project, growth was conducted under an argon back-pressure of ~700 – 900 mbar (see Figure 2.6(b)). Our collaborators at Erlangen also performed a pre-growth hydrogen etch process to clean up the CMP-polished SiC surface. This resulted in formation of wide, highly uniform, atomically flat terraces prior to growth. The argon atmosphere growths required higher temperatures for sublimation and helped achieve better surface morphology. Significantly lower roughening and pitting were observed in these growths. Better quality of growth is aided by the higher over-pressure of Si during evaporation [30] and enhanced surface diffusion of carbon at the higher temperatures.

2.3.2 Comparison of graphene on Si and C and faces

SiC being a polar material has two kinds of crystal faces: the Si-face or (0001) face, which is terminated with Si atoms and the C-face or $(000\bar{1})$ face, which is terminated with C atoms. The growth of graphene on the two faces differs appreciably. This section briefly highlights these differences.

2.3.2.1 Graphene on Si face of SiC

Growth of graphene on the Si face occurs via a step-flow process (Figure 2.7). Initially, a $\left(6\sqrt{3} \times 6\sqrt{3}\right)R30^o$ structure, also known as the "buffer layer" nucleates at the step edges. It is composed of carbon atoms arranged in a honeycomb lattice structure. About 30% of the carbon atoms are bonded with the Si underneath, as depicted in Figure 2.8(a). The first layer of graphene is formed by a second layer of

carbon atoms on top of the buffer layer. The bandstructure of the buffer layer obtained from angle-resolved photoemission spectroscopy (ARPES) has been shown to be unlike graphene (Figure 2.8(b)). An AFM image of graphene grown on the Si face is shown in Figure 2.9(a).

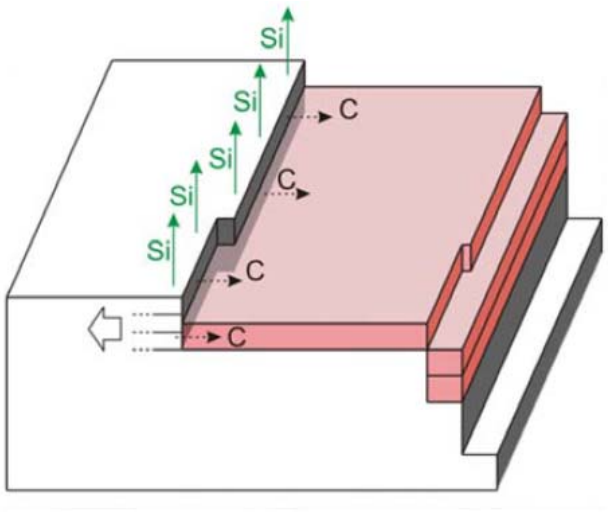

Figure 2.7: Step-flow growth on the Si face. Adapted from [31].

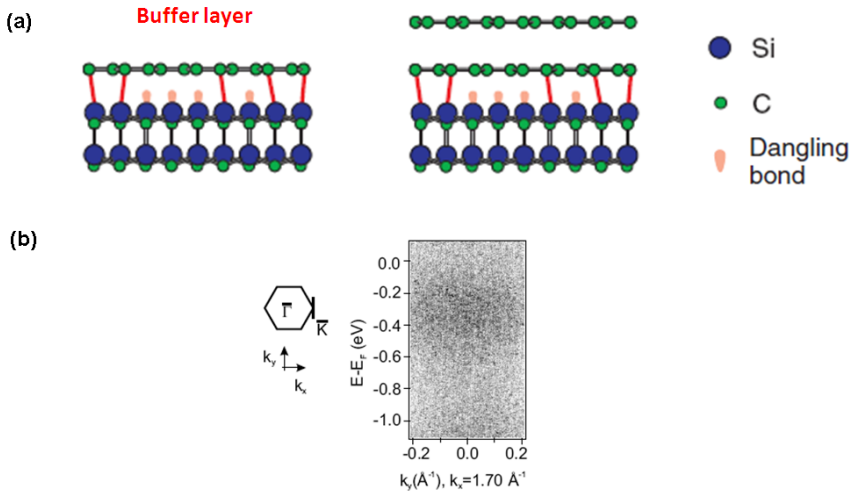

Figure 2.8: (a) Buffer layer and Monolayer graphene on SiC(0001). Adapted from [32]. (b) ARPES bandstructure of the buffer layer. Adapted from [33].

2.3.2.2 Graphene on the C face of SiC

In case of graphene growth on the C face of SiC, no covalently bonded buffer layer exists. Rotated domains of graphene exist which indicate absence of such a buffer layer [34]. Also, the rate of growth of graphene on the C face has been found to be much higher than on the Si face. Graphene "folds" and "wrinkles" may be observed in the AFM image of Figure 2.9 (b).

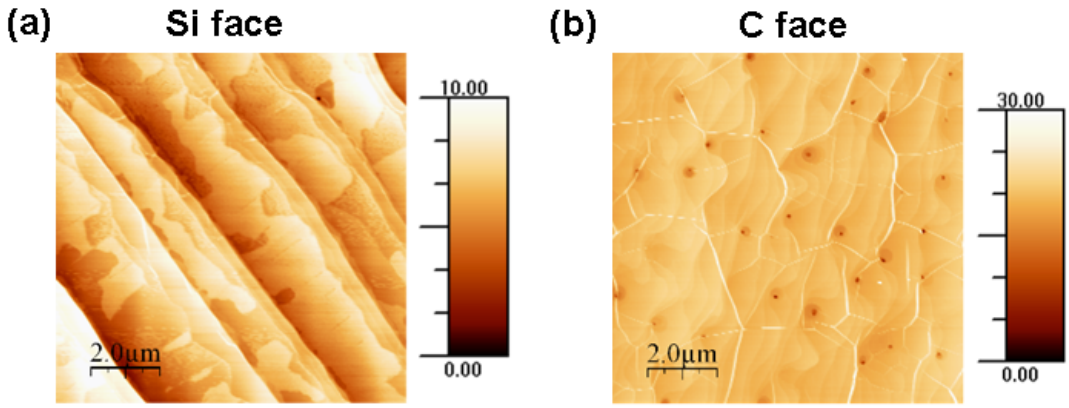

Figure 2.9: Comparison of AFM images of graphene grown on (a) Si face (b) C face. Step bunching is seen on the Si face. Graphene folds and wrinkles are observed on the C face.

2.4 Raman spectroscopy of graphene

2.4.1 Characteristic Raman modes of graphene

Raman spectroscopy is a very versatile technique to characterize carbon materials. In this section, we shall discuss the main peaks exhibited by graphitic materials.

Figure 2.10 shows the phonon bandstructure of graphene. The characteristic bands of graphene are the *G*, *2D* and *D* modes which are shown in Figure 2.11. The *G* peak (~1580 cm^{-1}) is associated with the doubly degenerate zone-center longitudinal and in-plane transverse optical phonon (LO and iTO) modes. The G mode corresponds

to a stretching motion of the carbon bonds. The *2D* peak (~2700 cm^{-1}) corresponds to a two-phonon excitation associated with the zone-boundary iTO phonons and has been found to have unique signatures distinguishing layer number and stacking order for few-layer graphene systems [35]. A small *D* peak (~1350 cm^{-1}), which corresponds to the zone-boundary iTO phonon, may be activated by defects. The *D* mode corresponds to a breathing motion of the carbon rings.

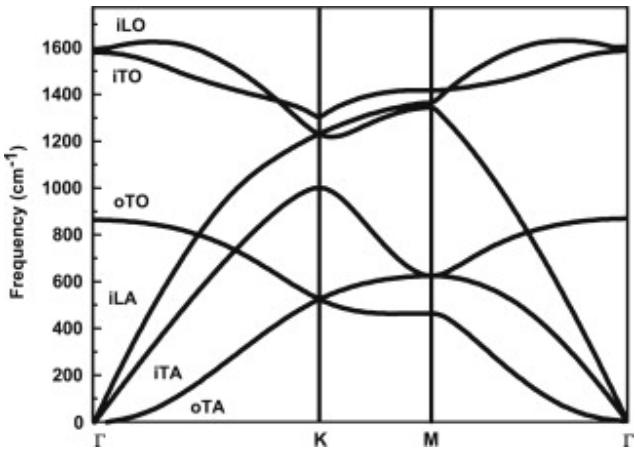

Figure 2.10: Phonon dispersion of graphene. Adapted from [36].

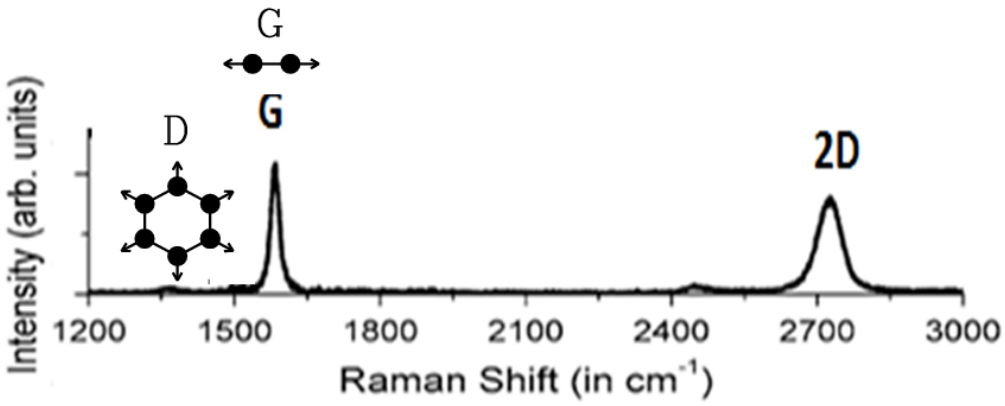

Figure 2.11: Main signatures of the graphene Raman spectrum

A second defect peak, denoted by *D'* (~1620 cm^{-1}), which corresponds to an intra-valley scattering event due to a LO phonon, may sometimes be activated.

2.4.2 Estimation of graphene thickness

This section has been adapted from a paper published in the Journal of Electronic Materials [37]. Estimating thickness of epitaxially grown graphene is an important part of its characterization. Methods for estimating thickness include Auger electron spectroscopy [22], X-ray photoelectron spectroscopy (XPS) [38] and optical transmission measurements using infrared spectroscopy [39]. The first two techniques are limited by the inelastic mean free path of the auger/photo-electrons in the film (~2.1 nm for a kinetic energy of 1200eV [40]) and are limited to less than 12 monolayers. The optical transmission method is suitable only for semi-insulating substrates, as the transmission through doped substrates is very low on account of free carrier absorption.

We developed a method of estimating multilayer graphene thickness grown heteroepitaxially on SiC using Raman spectroscopy at an excitation wavelength of 488 nm. We observe a dependence between the attenuation of the substrate Raman signal and the thickness of the graphene film. We use a simple absorbing overlayer model to explain the observed dependence and extract the absorption coefficient of graphene from the fit.

The refractive index of graphene is 2.6-1.3i [41], which corresponds to an attenuation length of ~30 nm or ~89 monolayers for a 488 nm wavelength optical excitation. Thus, this method can be used to estimate thickness beyond that possible

by XPS and AES. Also, Raman spectroscopy is capable of estimating grain sizes and disorder in graphene [42,43]. So, it is possible to simultaneously map graphene thickness, grain sizes and disorder over a region using this technique. We used XPS and transmission electron microscopy (TEM) as calibration techniques to estimate thickness of unknown graphene samples.

X-ray photoelectron spectroscopy (XPS) of the grown surfaces was performed using a Surface Science Instrument SSX-100 which utilizes monochromated Aluminum K-alpha x-rays (1486.6 eV) to strike the sample surface. The X-ray beam spot was a 2mm x 1mm ellipse. Figure 2.12(a) shows the high resolution C 1s peak scan for one of the samples. A number of components can be identified - SiC (282.9 eV), graphene (284.5 eV), C_xH_y (285.1 eV) and C-O-H (286.2 eV) [44]. The Si 2p peak high resolution scan (Figure 2.12(b)) shows two components corresponding to the substrate (100.5 eV) and SiO_2 (102.4 eV). Comparing the Si 2p substrate peak intensity, I_{SiC}, with the graphene peak intensity, I_G, from the C 1s scan and using the Thickogram method [45], the thickness, *t*, of the graphene overlayer can be estimated. The Thickogram is a nomograph for solving the equation:

$$\ln\left(\frac{I_G}{I_{SiC}}\right) - \left[\left(\frac{E_G}{E_{SiC}}\right)^{0.75} - \frac{1}{2}\right]\frac{t}{\lambda\cos(\theta)} - ln2 = \ln\sinh\left(\frac{t}{2\lambda\, cos(\theta)}\right)$$

where E_G, E_{SiC} are kinetic energies of the photoelectrons emitted at the overlayer and substrate peaks, θ is the emission angle and λ is the inelastic mean free path of the photoelectrons. The thickness estimated from XPS has an error margin of 20% because of the uncertainty in the inelastic mean free path [38].

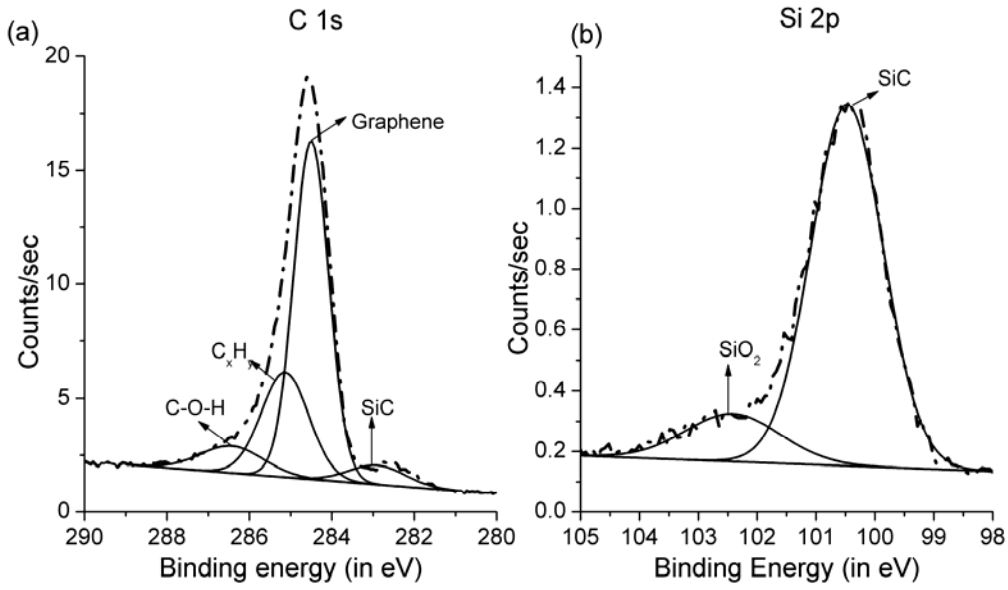

Figure 2.12: XPS high resolution scans for C 1s and Si 2p peaks for a graphene sample with thickness ~10 monolayers.

Alternatively, TEM was used to estimate the graphene thickness. TEM samples were prepared using a Focused Ion Beam (FIB) lift-out technique. Prior to ion milling, the samples were protected with a 5 keV e-beam deposited Pt cap to preserve the initial surface integrity. The samples were then prepared by FIB milling with a Ga ion beam at 30 keV to a thickness of ~1 μm and then finally milled using an Ar ion beam at 500 eV to remove the Ga ion damage and to obtain electron transparency for high resolution imaging. Then the samples were inserted into an FEI Titan TEM operated at 80 keV. Bright-field TEM images for two of the samples, T1 and T2, are shown in Figures 2.13(a) and (b).

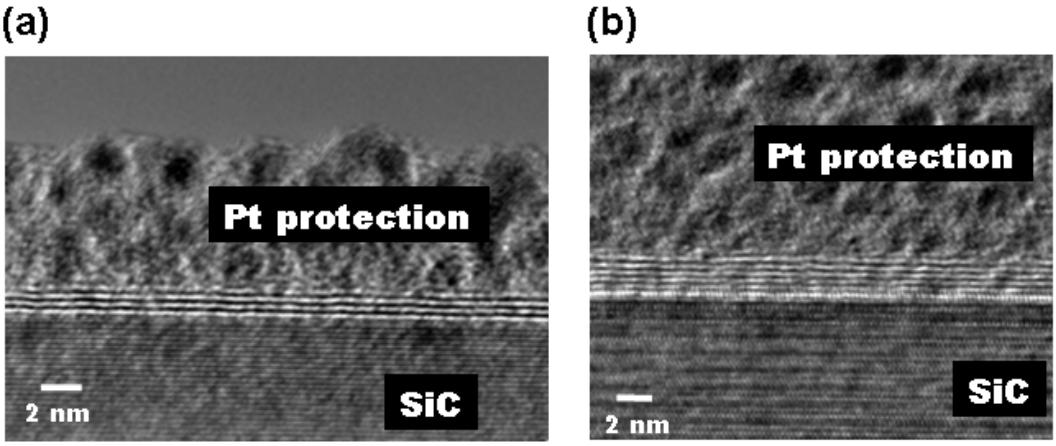

Figure 2.13: Bright-field TEM images for two samples. (a) T1: ~2 monolayers of graphene (b) T2: ~5 monolayers of graphene.

Micro-Raman spectra (Figure 2.14) were recorded using a Renishaw inVia Raman microscope with a 488 nm excitation wavelength. The Raman signals from the films showed prominent characteristic graphene peaks at ~1585 cm^{-1} (G) and ~2720 cm^{-1} (2D). A disorder-induced D peak at ~ 1360 cm^{-1} is also seen for some of the samples. SiC also has several overtone peaks in the 1000-2000 cm^{-1} regime. The peak at ~ 1516 cm^{-1} is considered to be an overtone of the L point optical phonon [46]. This peak is attenuated in intensity on account of the graphene overlayer and is the basis of our thickness estimation technique detailed below.

The remaining fraction of the substrate Raman intensity after attenuation by the graphene overlayer, *S*, is estimated from the sample's Raman spectrum by removing the background corresponding to SiC. This is done by subtracting a scaled reference spectrum of pure SiC substrate. This process is depicted pictorially in Figure 2.15. The same laser power was used for each sample and the corresponding reference spectrum. The fraction, *S*, can be estimated to within ±0.02 by this method.

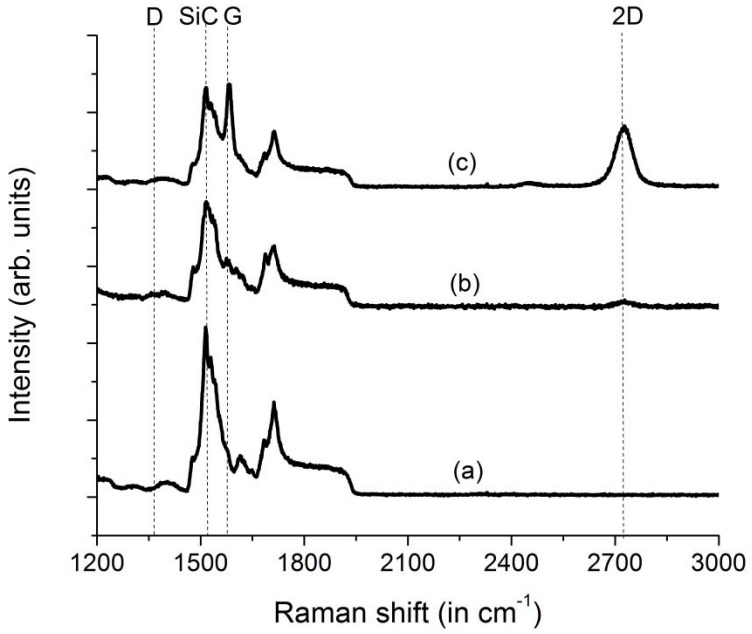

Figure 2.14: Micro-Raman spectra for (a) SiC substrate (b) ~5 monolayers epitaxial graphene on SiC (c) ~10 monolayers EG on SiC. The attenuation of the SiC Raman signal can be seen.

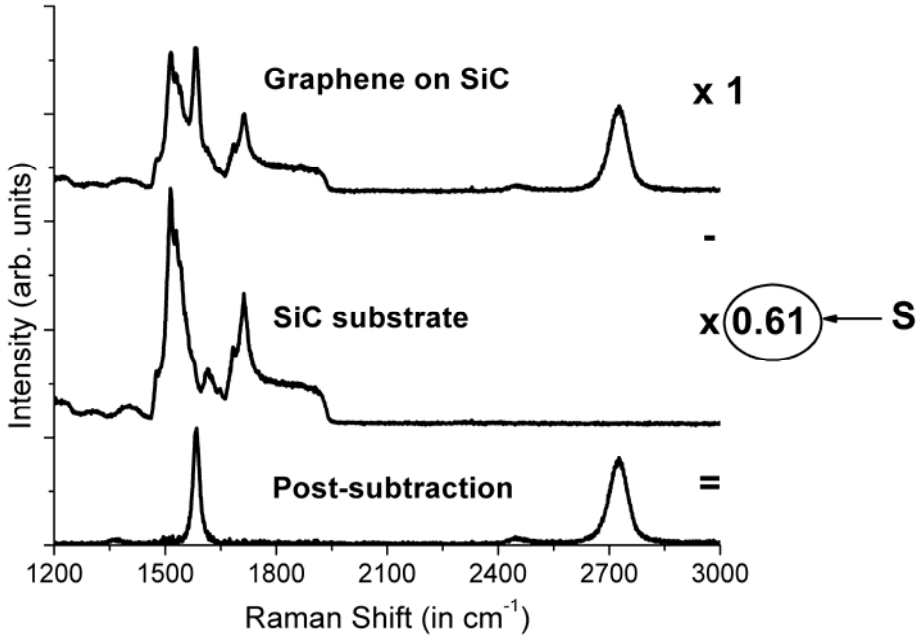

Figure 2.15: Schematic depicting the subtraction procedure by which the substrate Raman signal fraction, *S*, is obtained.

We plot the logarithm of the remaining fraction of the substrate Raman signal, *ln(S)*, against the thickness, *t*, of the film estimated from XPS and TEM in Figure 2.16(a). The samples for which thickness was obtained from TEM are indicated by the labels T1 and T2 on the figure. The errors involved in the data points are indicated by error bars. We find that the points fall on a straight line with slope 0.039±0.005. This dependence can be explained using a simple absorbing overlayer model (Figure 2.16(b)). Assuming graphene thickness to be *t* monolayers, an absorption coefficient α, the fractional Raman signal intensity from SiC post-attenuation by graphene can be written as $S = e^{-2\alpha t}$. From the fit, we extract α = 0.020±0.002 per monolayer for graphene, which translates to 2.0±0.2 % per monolayer. This extracted value is close 2.3% per monolayer reported for graphene. It is to be noted that the XPS, TEM and Raman probes have different lateral resolutions. Thus, the absorption coefficient extracted from the fit is an approximate estimate for the true absorption coefficient of graphene.

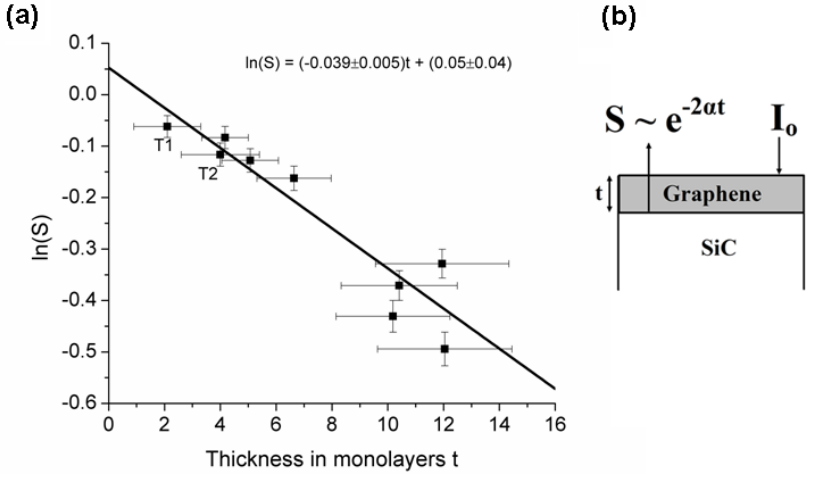

Figure 2.16: (a) Substrate Raman signal fraction versus estimated thickness of graphene. Solid line corresponds to the fit. (b) Schematic for the Raman signal attenuation model.

An error analysis using the error bars in S and α reveals that the percentage error in thickness estimated using this method is high for graphene upto 5 monolayers thick (Fig. 2.17). Beyond that, this model predicts thicknesses within an error bar of 25%. We believe that with better calibration, this error margin can be reduced.

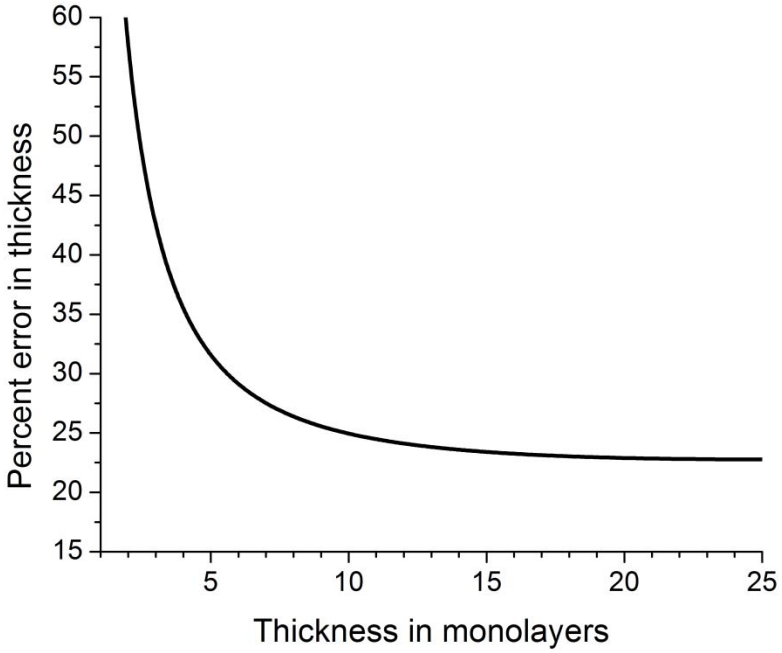

Figure 2.17: Percentage error in the thickness estimated using the Raman technique.

As a proof-of-concept, a thickness mapping was undertaken for an inhomogeneous epitaxially grown graphene sample using the above method. Fig. 2.18 plots the variation in thickness estimated using the Raman technique over a line-scan of ~18 μm. The shaded region represents the error margins in the thickness estimates. The image at the bottom depicts the variation in G peak intensity over the same region. It is seen that a thicker graphene film corresponds to a more intense G-peak signal.

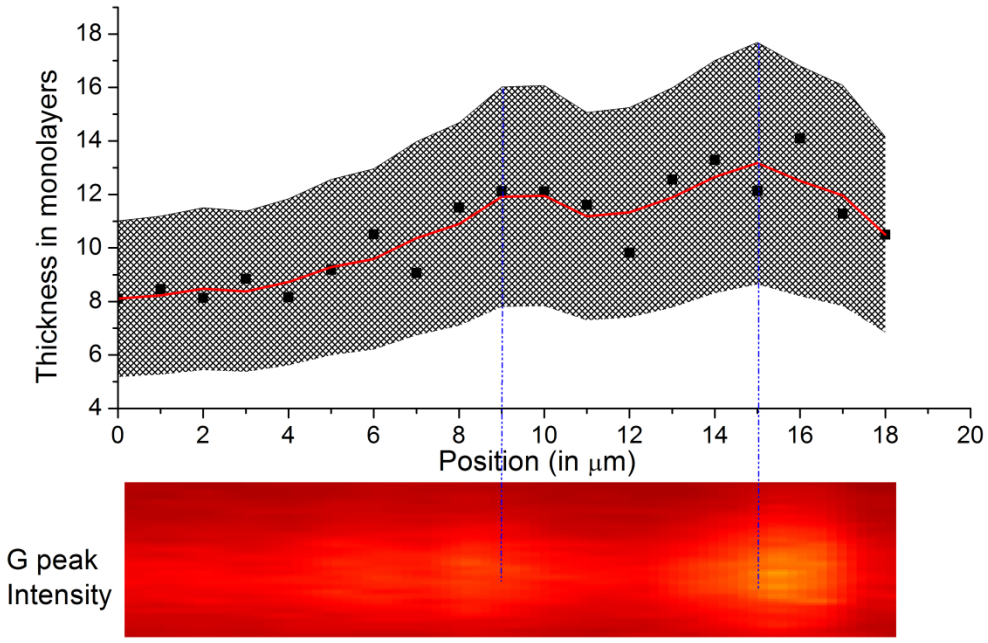

Figure 2.18: Raman thickness map over an 18 μm line region. The shaded area represents the error margin in the thickness estimates. The G peak intensity along the line is shown below.

In conclusion, a simple, non-invasive and convenient method has been outlined for the estimation of the thickness of graphene layers by using the attenuation of the Raman signal from the SiC substrate. This method is capable of estimating thickness of multilayer graphene films beyond that possible by XPS and Auger electron spectroscopy (AES), as it is not limited by the small inelastic mean free path of auger/photo-electrons. Though the method, as we have presented it, has significant error for graphene films upto 5 monolayers thick, we believe that this limitation can be overcome by better calibration. This method can prove to be useful for mapping graphene thickness, grain size and disorder simultaneously over a large region.

2.5 Electrical characterization of graphene

In this final section, a few results on electrical characterization of EG on SiC will be presented. Fabrication of devices followed the general procedure outlined below:

1. Alignment marks were created on the SiC using photolithography, a short oxygen plasma etch and Ti/Au (10 nm/100 nm) deposition using an e-beam evaporator, followed by lift-off in Microposit Stripper 1165.
2. Photolithography and an oxygen plasma etch (70 s, standard O_2 plasma recipe) were used to define the graphene structures.
3. Contacts to the graphene were made using photolithography and Ti/Au deposition, followed by lift-off in acetone. It is important that graphene be patterned before contact metal deposition because adhesion of metal to graphene is poor.
4. In case of field-effect transistors (FETs), the devices were dipped in 1% poly-vinyl alcohol (PVA) and rinsed in DI water prior to deposition of 52 nm of HfO_2 using atomic layer deposition (ALD). The PVA layer helps seed the ALD growth [47]. This was followed by a Ti/Au top gate deposition using photolithography and lift-off.

All lithography steps were performed using the Autostep AS-200. Oxygen plasma etch was performed using the Oxford 80 plasma etch tool.

2.5.1 Hall measurements

Hall measurements were performed on Hall cross structures using a magnet-probe station, under a nominal out-of-plane magnetic field of 0.2 T. Results of the measurements are summarized in Figure 2.19, where carrier density and mobility are

plotted as a function of the device dimension for graphene on Si and C faces. Typical carrier densities were of the order of mid-10^{12} cm^{-2} to low-10^{13} cm^{-2} and typical carrier mobilities were ~ 500-1000 cm^2/V-s. It was observed that C face devices exhibited higher mobility than Si face devices.

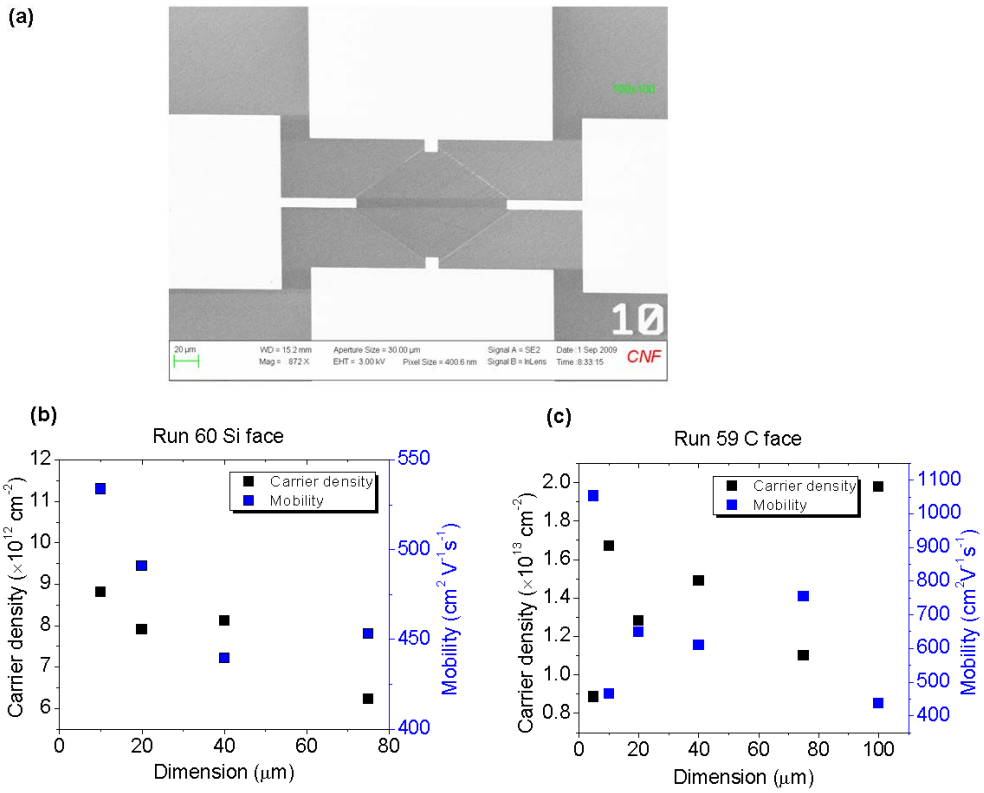

Figure 2.19: (a) SEM image of a 100 $\mu m \times 100\ \mu m$ Hall cross. Carrier density and mobility of graphene on (b) Si face (c) C face.

2.5.2 FET measurements

A typical graphene FET top-gate sweep is shown in Figure 2.20(b). The device exhibits ambipolar behavior as expected. Hysteresis is observed in the $I_d - V_G$ sweep at room temperature and may be reduced by cooling the device to low temperatures. Figure 2.20(c) shows an example curve fit of the gate voltage sweep by employing

three fitting parameters: R_c, the contact resistance, n_0, the residual carrier concentration and μ, the mobility [48].

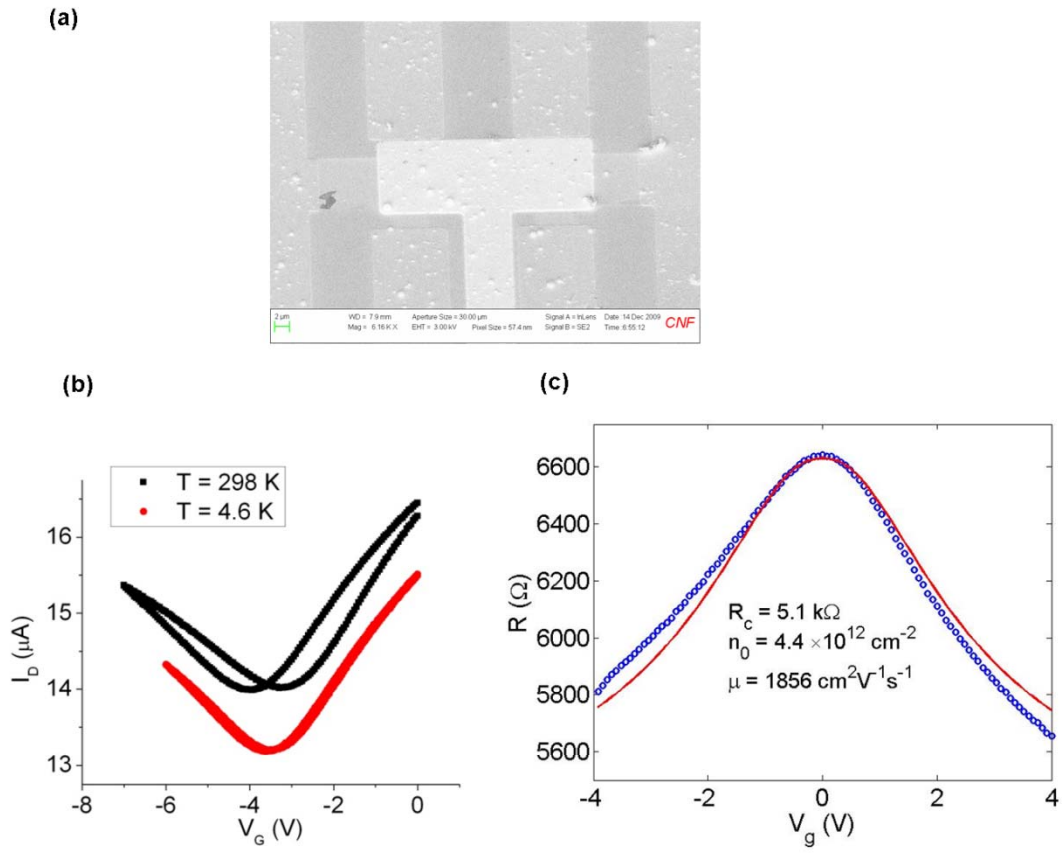

Figure 2.20: (a) SEM image of top-gated graphene FET. (b) Plot of $I_d - V_G$ at room temperature and 4.6 K. Hysteresis is observed in the room temperature sweep. (c) Example curve-fitting performed to extract mobility of a graphene FET device.

CHAPTER 3

FREE-STANDING EPITAXIAL GRAPHENE (FSEG): FABRICATION AND MECHANICAL PROPERTIES

In this chapter, we report on a method to produce free-standing graphene sheets from EG on silicon carbide (SiC) substrate. Doubly-clamped nanomechanical resonators with lengths up to 20 μm were patterned using this technique and their resonant motion was actuated and detected optically. Resonance frequencies of the order of tens of MHz were measured for most devices, indicating that the resonators are much stiffer than expected for beams under no tension. Raman spectroscopy suggests that the graphene is not chemically modified during the release of the devices, demonstrating that the technique is a robust means of fabricating large-area suspended graphene structures. Parts of this chapter have been adapted from a paper published in Nano Letters [49].

3.1 Motivation for free-standing epitaxial graphene (FSEG)

In order to study the properties of epitaxially grown graphene, it would be beneficial to isolate the graphene from the substrate. For example, it has been reported that the electronic mobility of suspended exfoliated graphene is ~ 10 times larger than that of exfoliated graphene supported on a substrate [10]. Also, graphene nanoelectromechanical devices have great potential for ultra-sensitive mass, force and charge sensing [18,50]. Thus motivated, in this chapter, we fabricate nanomechanical

free-standing epitaxial graphene (FSEG) resonators. Resonance measurements using optical interferometry and nano-indentation using an atomic force microscope (AFM) cantilever are employed to probe the mechanical properties of these doubly-clamped structures.

3.2 Fabrication of FSEG

SiC is chemically a highly resistant material and it is typically patterned using dry etching techniques. However, the plasmas involved in the dry etching process will destroy the graphene and are incapable of undercutting. Hence, a wet etching process is necessary to etch the SiC and suspend the graphene.

3.2.1 Photoelectrochemical (PEC) etching of SiC

A literature survey of wet etching techniques for SiC reveals two alternatives: 1. Etching in molten eutectic of NaOH-KOH [51]; 2. Photoelectrochemical etching [52,53]. The former uses high temperatures of 450-570 ^{o}C and is thus quite detrimental to graphene. The latter method of photoelectrochemical etching, on the other hand, may be performed at room temperature and is quite promising.

Initially, dilute HF (1M – 4M) was used to etch n-type SiC [52]. Various optical systems were employed to illuminate the SiC surface using ultraviolet (UV) light including a 325 nm He-Cd laser. However, it was observed that etching using HF did not produce uniform and smooth surfaces. It was suspected that a passivation layer of porous SiC was responsible for the reduction in etch rate with time [54]. Further

details about the early experiments may be found in the Masters thesis of Xun Yu [55].

Dilute KOH (1-2% aq.) was the second electrolyte of choice. An epi-fluorescence microscope equipped with a 100 W mercury arc lamp acted as the source of UV light. The n-type SiC with evaporated Ni as a mask (see Figure 3.1(a)) served as the anode and platinum sheet served as the counter electrode. The anode contact to the SiC was made using double-sided copper tape and magnet wire (Figure 3.1(b)). Silver paint was sometimes used along with the magnet wire when contact needed to be made to the front-side of the SiC die. Everything except the region of interest on SiC was then insulated from the electrolyte using mounting wax (71-10040 Hot Mounting Wax from Allied High Tech).

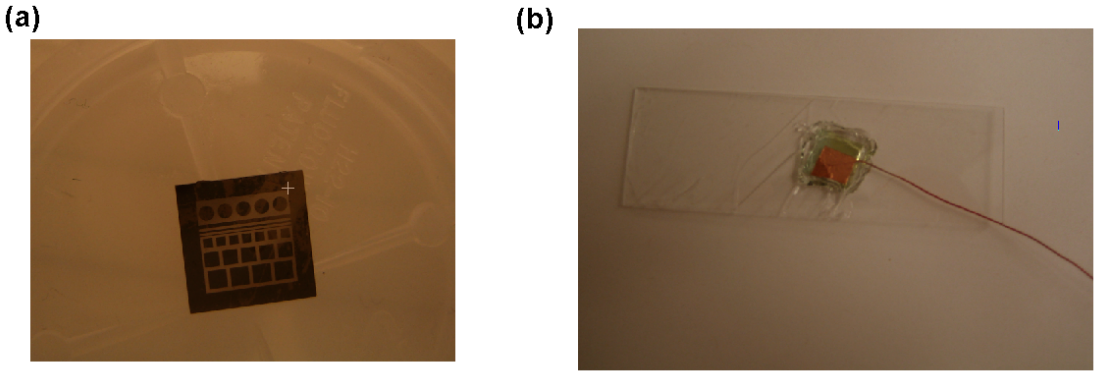

Figure 3.1: (a) n-type SiC with a patterned Ni layer. The Ni acted as a mask to protect the SiC from etching during the PEC process. (b) Picture showing the back contact made to SiC using double-sided Cu tape and magnet wire. The SiC die is place on a glass slide for support. The die is subsequently encapsulated using wax leaving only the region of interest exposed.

A picture of the etch setup is shown in Figure 3.2(a). Preliminary experiments used a petri dish to contain the electrolyte (Figure 3.2(b)). A platinum wire was used as the counter-electrode. Later, a home-built Teflon electrochemical cell having a

platinum sheet as the counter electrode was used (Figure 3.2(c)). The Teflon cell has nozzles which enable its connection to a peristaltic pump in for ensuring circulation of the electrolyte during the etch. A voltage of 700-900 mV was applied for the duration of the etch.

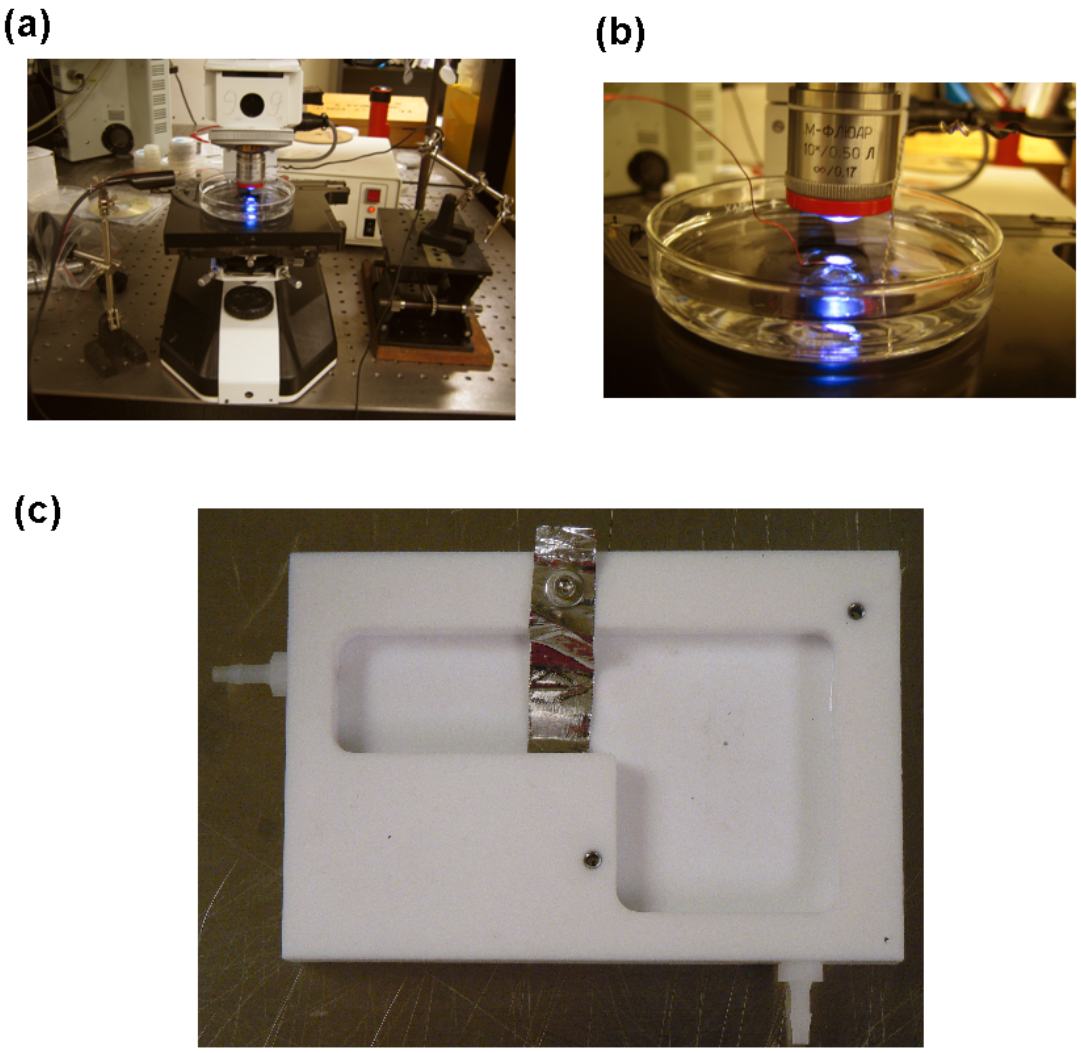

Figure 3.2: (a) Picture of the etch setup showing the epi-fluorescence microscope (b) Close-up of the preliminary etch setup. A 10 × objective was used to focus the light. The Pt wire may be seen to the right. (c) Home-built Teflon electrochemical cell with nozzles for connection to a peristaltic pump and a Pt sheet counter-electrode.

The band diagram at the interface of n-SiC and the electrolyte is shown in Figure 3.3. A depletion region and a consequent electric field exists at the surface. Upon illumination with the above-bandgap light source, electron-hole pairs are generated in SiC. The holes are attracted to the surface because of the electric field and cause dissolution of SiC. The chemical reaction which takes place during the etching process may be described by the equation [56]

$$SiC + 8OH^- + 6h^+(VB) \rightarrow [Si(OH)_2O_2]^{2-} + CO + 3H_2O$$

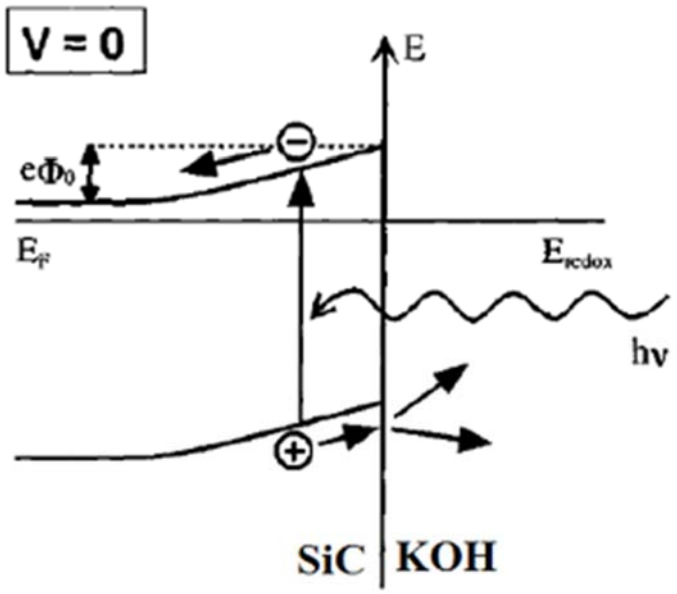

$$SiC + 8OH^- + 6h^+(VB) \rightarrow [Si(OH)_2O_2]^{2-} + CO + 3H_2O.$$

Figure 3.3: Band diagram at n-SiC–KOH interface. Holes generated by the light source accumulate at the surface and cause SiC dissolution (Adapted from [57])

Figure 3.4(a) shows results of the experiment with after the Ni protective mask has been removed. The area on SiC exposed to UV light was successfully etched away. A profilometer scan across the etched region is shown in Figure 3.4(b). Typical

SiC etch rates were 1-2 $\mu m/hr$. The etch depth was fairly uniform over the entire region.

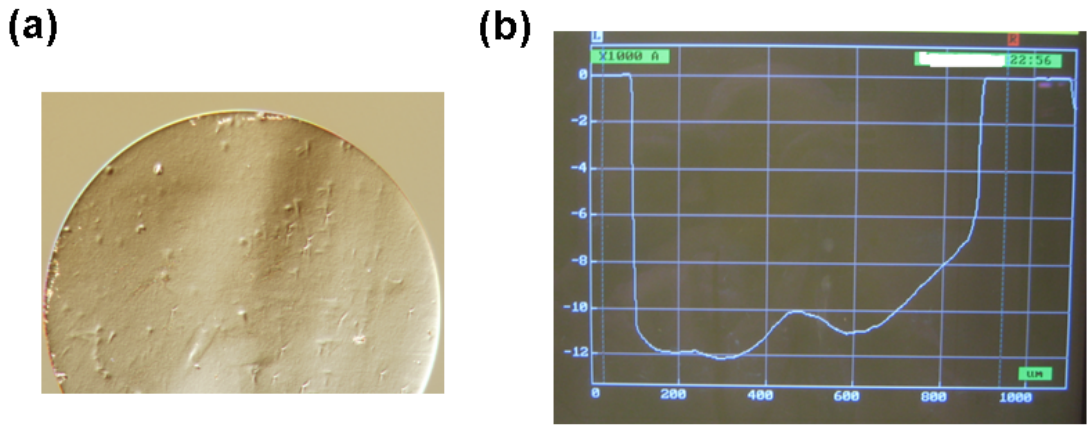

Figure 3.4: (a) Optical micrograph of etched SiC after the PEC process. The circle diameter is 800 μm. (b) Profilometer scan of the etched region. Etch depth is ~ 1.2 μm.

3.2.2 Fabrication of FSEG doubly-clamped beams

With the baseline SiC etch process established, the next step was to adapt this to produce FSEG doubly-clamped beams. A schematic of the fabrication and wet etching process is shown in Fig. 3.5. Fabrication of the devices proceeded by evaporating 100 nm of gold as contact pads, which also served as masks for the PEC process. Graphene was then patterned using standard photolithographic techniques and an oxygen plasma etch. Aqueous potassium hydroxide (1%) was used as the electrolyte and the etch was performed at room temperature. The undercut caused by the isotropic etch was sufficient to release the graphene sheets. The current during the etch process was ~1.2 mA/cm^2 and the etch rate was ~1 μm/hour. The etch was performed for four hours. The etched area is determined by the spot size of the light source and the amount of undercut decreases as the light intensity falls off from the centre of the focused light

spot. Because of the non-uniformity of the light spot, the etch depth over the etched region varies from ~1 μm to ~8 μm, as measured by profilometry. The yield for the devices is 80-90%.

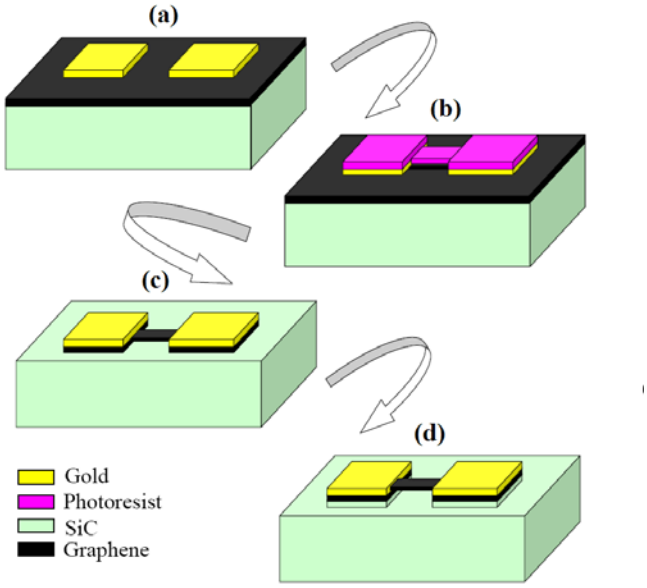

Figure 3.5: Schematic of the fabrication process – (a) 100 nm thick gold pads defined photolithographically using lift-off (b) Photoresist patterned over graphene (c) Oxygen plasma etch to define graphene beams and removal of photoresist (d) Photoelectrochemical etching to release the graphene sheets.

A scanning electron microscope (SEM) image of arrays of doubly-clamped SEG devices produced by this technique is shown in Fig. 3.6(a). This technique works even for extremely thin (few layer) graphene, as evidenced by the electron transparency of the device shown in Fig. 3.6(b). Devices with dimensions ranging from 3 – 20 μm in length and 0.5 – 3.5 μm in width were successfully produced. The thickness of the graphene devices used in this study is estimated to be 1 nm (see Section 3.5.1). The devices were dried using a critical point drying technique to prevent surface tension induced breaking.

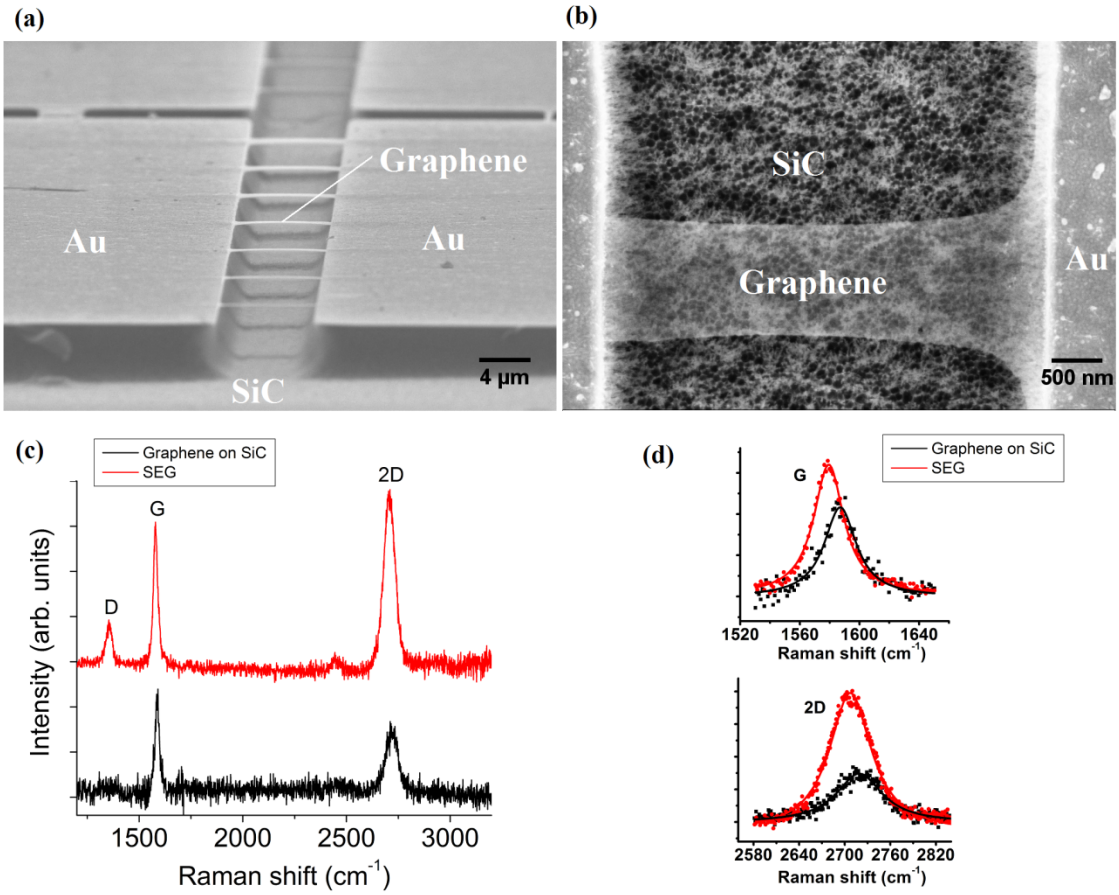

Figure 3.6: (a, b) Scanning electron microscope images of suspended epitaxial graphene (SEG). (a) An array of doubly clamped nanomechanical graphene beams of length 8 μm and widths ranging from 0.5 to 3.5 μm. The beams are clamped down on both ends by gold pads. (b) Top view of a SEG resonator, showing its electron transparent nature at an electron beam energy of 5 keV. (c, d) Raman spectra of graphene grown on SiC (after background subtraction) and suspended epitaxial graphene (SEG). Data for graphene on SiC are shown in black, and data for FSEG are shown in red. G, 2D, and D peaks are seen. The spectrum for the SEG is red-shifted as clearly shown by the zoomed-in spectra in (d). Also, we note that the 2D peak of FSEG is fit well by a single Lorentzian.

3.3 Raman spectroscopy and AFM of FSEG structures – Strain effects

Raman spectroscopy was performed on the graphene before and after the photoelectrochemical etch process (Figures 3.6(c,d)). Raman spectra were collected using a Renishaw InVia micro-Raman system with an excitation wavelength of 488

nm. A blue-shifted G-peak at 1587 cm^{-1} and a 2D peak at 2719 cm^{-1} are observed for graphene on SiC (after background subtraction). This blue shift has been attributed to compressive strain in the graphene grown on SiC [58]. A disorder-related D peak is barely visible. The Raman spectrum of a FSEG device shows the G peak at 1580 cm^{-1} and the 2D peak at 2707 cm^{-1}. These red-shifts for the suspended graphene are consistent with the hypothesis that registry with the substrate is the cause of the original blue shift. After the etch, a prominent D peak is observed at 1354 cm^{-1}. We attribute the D peak to disorder introduced in the graphene either during photolithographic processing or during the etch. However, there is no significant broadening of the G-peak in the suspended devices as has been observed for graphene oxide or functionalized graphene [59]. Thus, we conclude that the chemical structure of the graphene has not been adversely affected by the etching procedure.

AFM images and close-up SEM images of the SEG resonators in Figure 3.7 show that the resonators are buckled along their lengths. AFM line profiles along the lengths of two of the devices in AFM images and close-up SEM images of the SEG resonators in Figure 3.7 show that the resonators are buckled along their lengths. AFM line profiles along the lengths of two of the devices in Figure 3.6(a)-(b) provide a sample of the different configurations assumed by the buckled beams. The buckled shapes in the figure have been fit using sinusoidal waveforms. Indeed, EG on SiC is under compressive stress, as evidenced from the blue shifts in the Raman spectra [58]. The strain is given by $\varepsilon = (\Delta\omega/\omega)/\gamma$, where $\Delta\omega$ is the change in Raman wavenumber from the unstrained value ω, and γ is the Grüneisen parameter, which is 1.8 and 2.7 for the G and 2D modes, respectively [60]. The calculated value of the strain for our

devices is 0.2%. The corresponding compressive stress is orders of magnitude higher than the critical buckling load for the SEG resonators (see Section 3.5.2). Hence, we expect the graphene beams to be buckled. In addition, Figure 3.7(c) shows that the SEG resonators have "side-flanges" and curvature along the width, that make their cross sections look roughly like those of inverted U-channel beams. Also, many devices have local crinkles, as annotated in Figure 3.7(d).

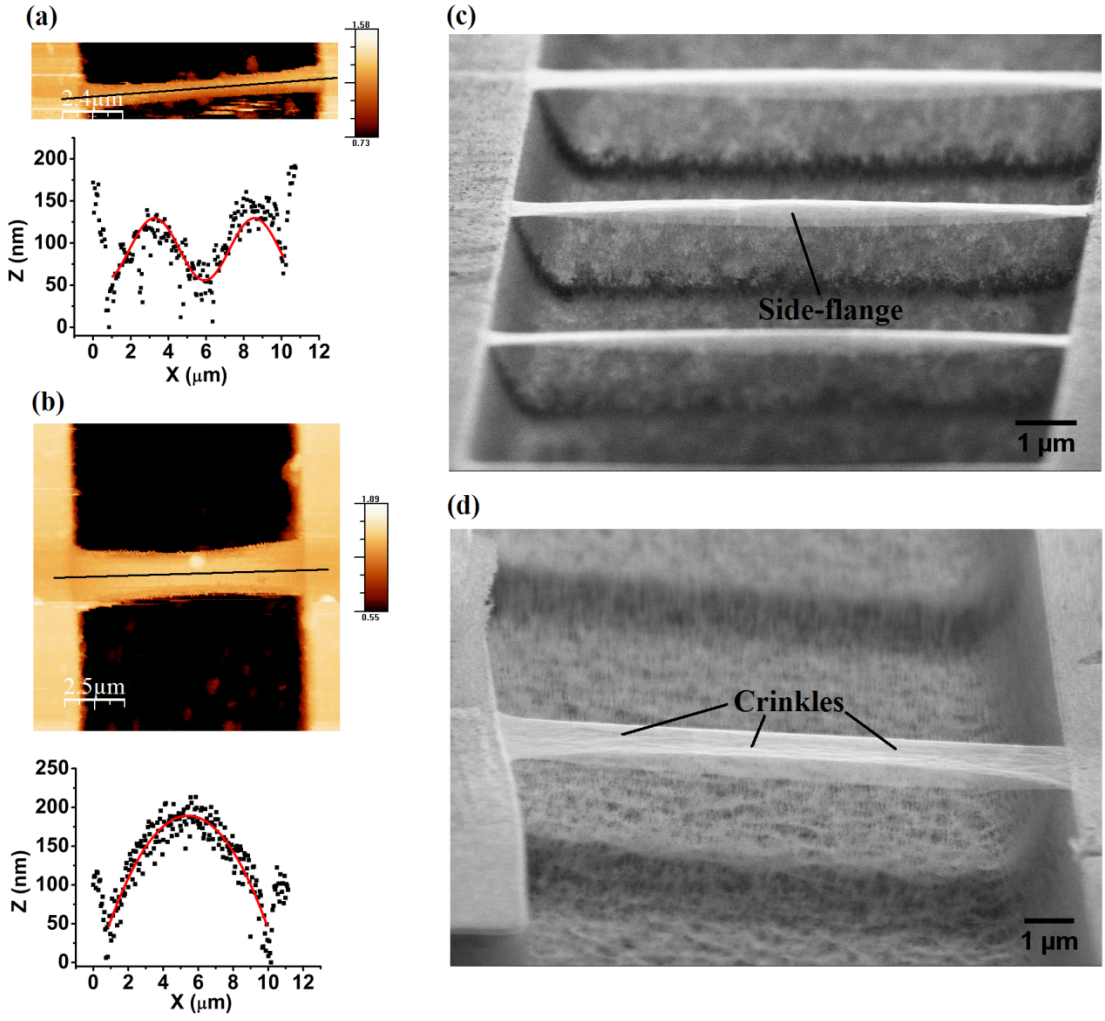

Figure 3.7: (a, b) AFM images of two SEG devices, showing the variability in configuration of the buckled beams. The shapes of the beams have been fit using sinusoidal waveforms. (c, d) SEM images of SEG devices, showing their buckled nature. The side-flanges and curvature along the width giving rise to a roughly inverted U-shaped cross section and local crinkling are annotated.

3.4 Mechanical resonance measurements

Mechanical resonance measurements were performed at room temperature under vacuum (10^{-6} Torr) using an optical actuation and detection technique identical to that described elsewhere and shown in Figure 3.8 [18,61]. In this technique, the intensity of a blue diode laser (405 nm) focused on the device is modulated at a known frequency, leading to periodic thermal expansion and contraction of the graphene layers. This motion of the graphene is detected using reflected light from a red laser (633 nm) coupled to a fast photodiode.

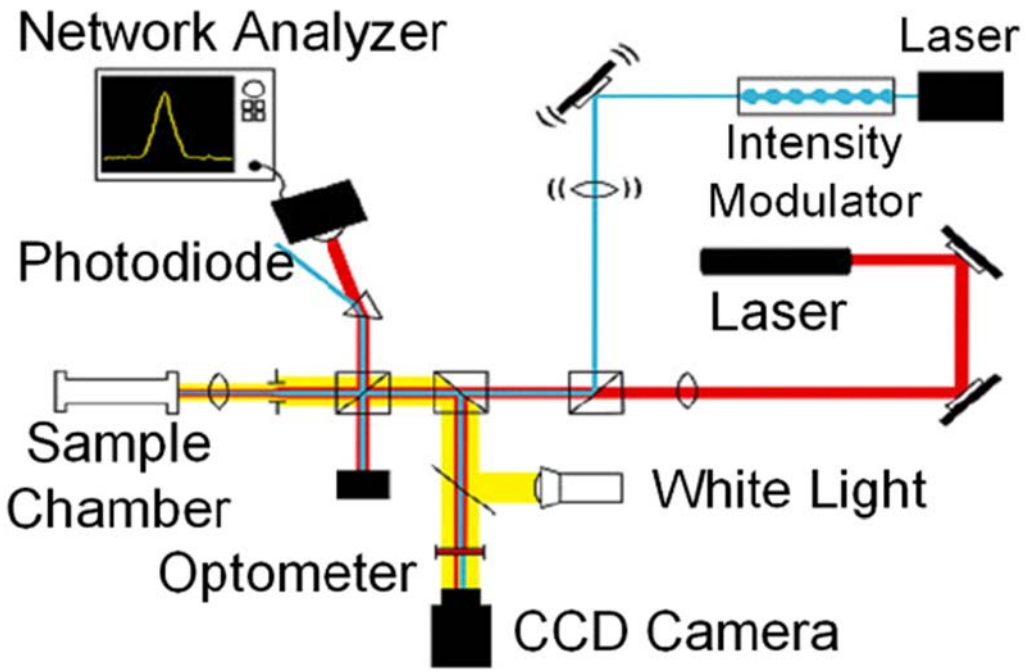

Figure 3.8: Optical interferometry setup to measure the mechanical resonance frequency [62]

The fundamental resonance mode, f_0, for a doubly clamped beam under no tension is given by [63]

$$f_0 = A\left[\left(\frac{E}{\rho}\right)\left(\frac{t^2}{L^4}\right)\right]^{\frac{1}{2}}$$

where E is the Young's modulus, ρ is the mass density, t and L are the thickness and length of the beam respectively, and the clamping coefficient, A, is 1.03. For micrometer-sized graphene beams with lengths in the range 3−20 μm and thickness of 1 nm, the equation predicts fundamental modes in the range 55 kHz to 2.4 MHz. Figure 3.9 shows the measured frequencies for FSEG devices of different lengths. The inset shows the measured resonance for a sample device. Q factors in the range of 50−400 were observed for most devices. Also plotted in Figure 3.9 are the resonances expected from the equation. The measured resonance frequencies are much higher than those predicted by the equation. Built-in tension is one of the factors responsible for increased frequencies in graphene resonators [18,64]. However, as discussed earlier, the FSEG resonators are not under tension and instead are buckled. We hypothesize that their inverted U-shaped cross section contributes to their increased rigidity. A model calculation showing how the U-shaped cross section could explain the increased resonance frequency for a device is included in Section 3.5.3. The scatter of the data for the FSEG resonators suggests that the resonance frequency of the devices depends strongly upon the local geometry. The variability in the configuration of buckled beams, local crinkling, and the inverted U-shaped cross section do not lend themselves easily to analytical modeling. Accurately predicting the resonant frequencies for the devices would require knowledge of the local geometry from a combination of AFM and SEM images and the residual stress in the devices postbuckling. Then, a finite-element analysis, similar to the one performed by

Robinson et al. [65], would be needed to calculate the vibrational modes of the devices.

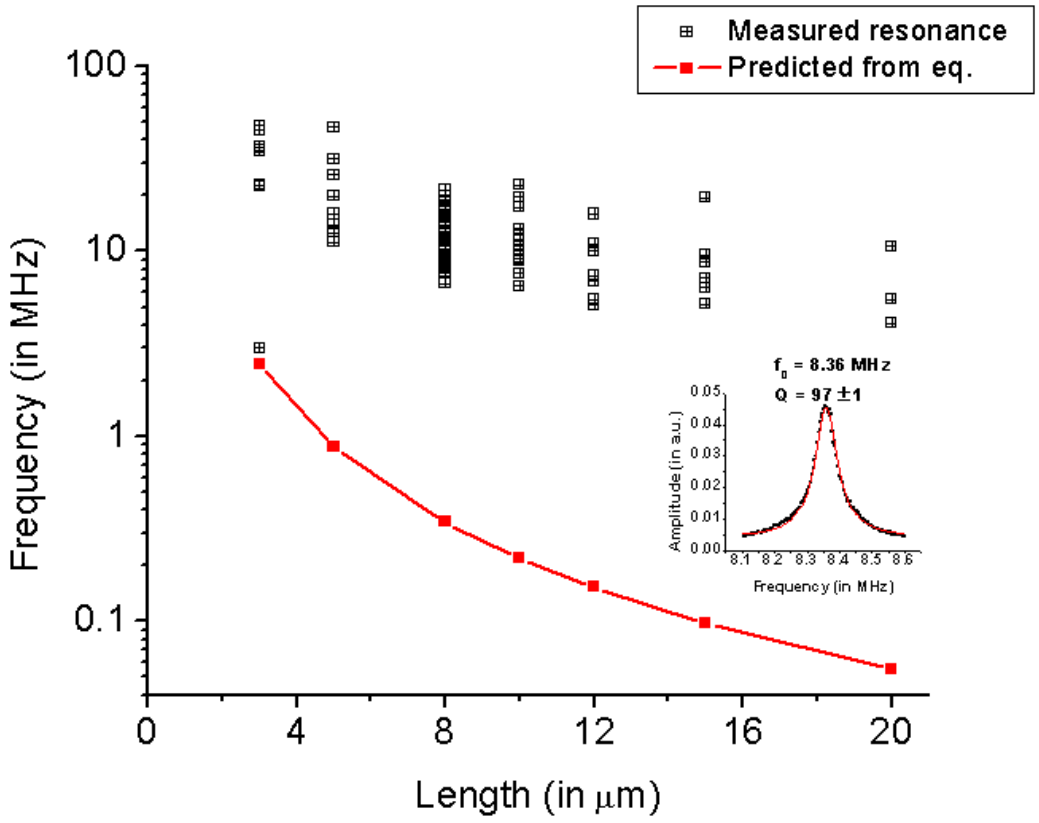

Figure 3.9: Plot of resonances of devices of various lengths measured using laser interferometry. The measured data are shown using filled squares. The frequencies expected from standard theory for a flat beam with no tension are plotted using hollow squares. Inset shows measured resonance of a sample device with length 8 μm.

In order to remove possible photoresist residues, the suspended devices were then annealed in an Ar/H_2 atmosphere (Ar/H_2 flow rates 400/600 sccm) at 400 °C for 1 h [66]. However, the annealing process destroyed many of the devices. The rupture could have been a result of either the high gas flow rates or thermal mismatch/adhesion issues between the gold contact pads and graphene. The FSEG resonators that survived the anneal were again probed using laser interferometry. The

frequencies of all FSEG resonators went up postanneal (Figure 3.10(a)). Also, Q factors close to 103 were observed for some devices (Figure 3.10(b)). Figure 3.10(c) shows SEM images of the same device before and after the annealing process. The reduction in the length of the side-flanges suggests increased tension in the annealed devices. Increased tension and possible residue removal could account for the higher frequencies and Q factors postanneal.

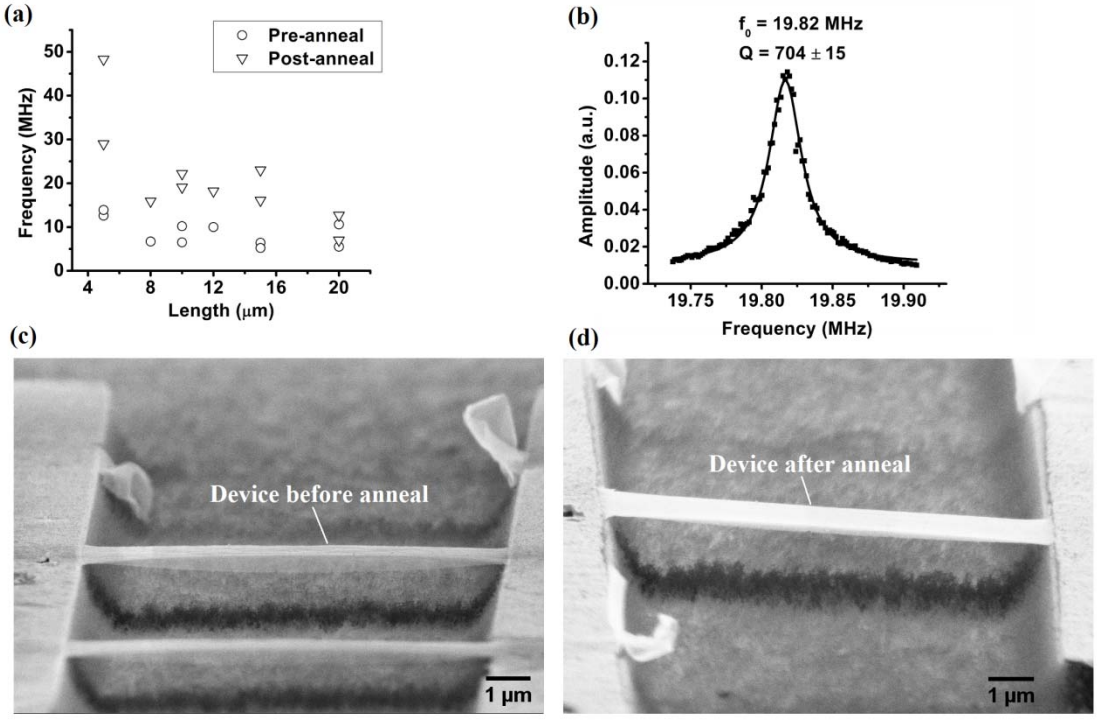

Figure 3.10: (a) Comparison of resonance frequencies of devices before and after anneal. (b) Measured resonance of a device after anneal. (c) SEM images showing a device before and after anneal.

3.5 Parameters and approximate mechanical model of FSEG resonators

3.5.1 Estimation of thickness of FSEG resonators

Graphene thickness was estimated using an atomic force microscope (AFM) by going over the step edge from SiC to graphene. Graphene on SiC was patterned into

strips using an oxygen plasma etch. Measurements were conducted by moving the AFM tip from a graphene-free region of SiC to graphene on SiC. However, thickness determination before the Ar/H_2 anneal was not straightforward because of the following two reasons: 1) oxidation of SiC upon exposure to the oxygen plasma 2) presence of steps on the SiC surface. It was found from AFM measurements that the region from which graphene had been etched away was higher than the region where graphene was present. This is attributed to a thin oxide layer forming on top of the exposed SiC after removal of graphene by the oxygen plasma. The Ar/H_2 anneal caused the oxidation layer to be removed and AFM measurements performed post-anneal suggest a graphene thickness no greater than 2 nm. For the sake of calculations in this work, we assume a graphene thickness of 1 nm.

3.5.2 Critical Buckling Load for FSEG Resonators

The critical buckling stress for a beam of length L and thickness t is given by $\sigma_{cr} = \frac{\pi^2 E t^2}{3L^2}$ [67], where E is the Young's modulus of the material. The corresponding strain is $\epsilon_{cr} = \frac{\pi^2 t^2}{3L^2}$. For a graphene beam of length 10 μm and thickness 1 nm, the critical strain for buckling is 3.3×10^{-6} %, which is five orders of magnitude smaller than the strain estimated from Raman spectra. So, we expect the graphene beams to be buckled.

3.5.3 Analytical model of U-shaped FSEG resonator

A schematic of the inverted U-shaped cross-section is shown in Figure 3.11(a). *w* and *t* are the width and the thickness of the beam respectively, while *y* denotes the length of the side-flange. The position of the neutral axis is given by

$$\bar{y} = \frac{\left(t(w-2y-2t)\right)\left[\frac{t}{2}\right] + 2\times(yt)\left[\frac{y}{2}\right]}{t(w-2y-2t)+2\times(yt)}$$

The moment of inertia of the beam about the neutral axis can be calculated by summing the moments of inertia of three smaller beams (two vertical and one horizontal), which the cross-section may be assumed to be comprised of.

$$I = \left[\frac{1}{12}(w-2y-2t)t^3 + (w-2y-2t)t\left(\bar{y}-\frac{t}{2}\right)^2\right] + 2\left[\frac{1}{12}ty^3 + ty\left(\bar{y}-\frac{y}{2}\right)^2\right]$$

The fundamental resonance frequency of the beam is then obtained using [63]

$$f_0 = \frac{4.73^2}{2\pi}\frac{1}{L^2}\sqrt{\frac{E}{\rho}}\sqrt{\frac{I}{wt}}$$

The resonator shown in Figure 3.11(b) is 20 μm long and from standard beam theory for a beam under no tension, it is expected to have a fundamental resonance at 54.9 kHz. The observed resonance for the device is at 12.7 MHz. The beam has side-flanges which cause it to be narrower in the center than near the clamps. It can also be seen that the cross-section of the beam varies over its length. However, as a simplifying approximation, we model the device with a uniform U-shaped cross-section, as described above. The length of the side-flange at the center of the beam can be estimated as (1572 – 836.7)/2 nm = 367.6 nm. Because of the non-uniform nature of the cross-section, we assume *y* to be uniformly half of this value in our simple

approximation i.e. y = (367.6/2) nm = 183.8 nm. Assuming this value of y and using the known dimensions of the beam and material parameters of bulk graphite, the calculated value for f_0 = 8.97 MHz. Hence, we propose that this simple model can roughly account for the observed increase in stiffness of the resonator.

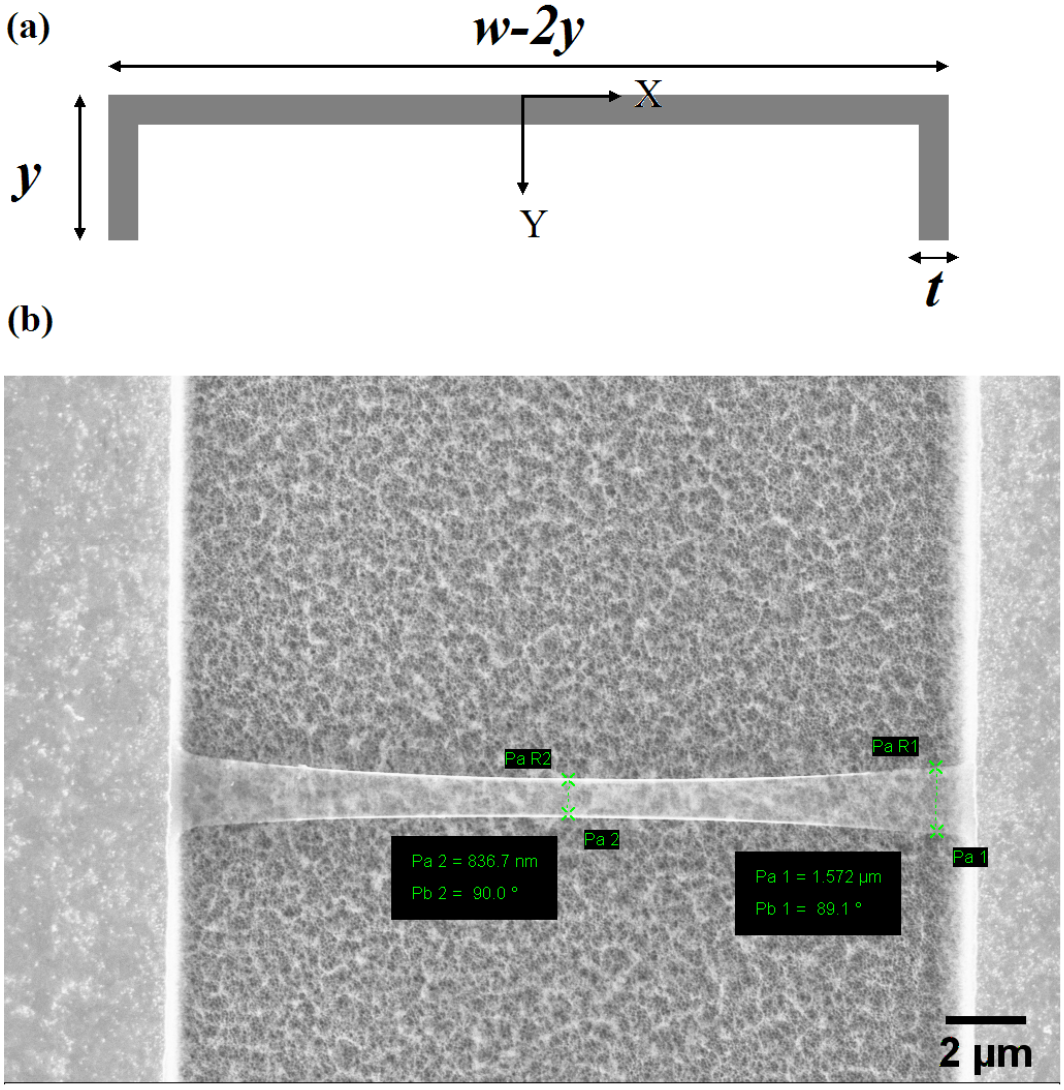

Figure 3.11: (a) Model of a beam with an inverted U-shaped cross-section (b) SEM image of a SEG resonator device. The device is narrower in the center because of the side-flanges.

3.6 Nano-indentation experiments using AFM cantilever

This section describes nanoindentation experiments which were performed using a calibrated AFM cantilever to probe the local stiffness of the devices following the anneal. A schematic of the nanoindentation experiment is shown as an inset in Figure 3.12.

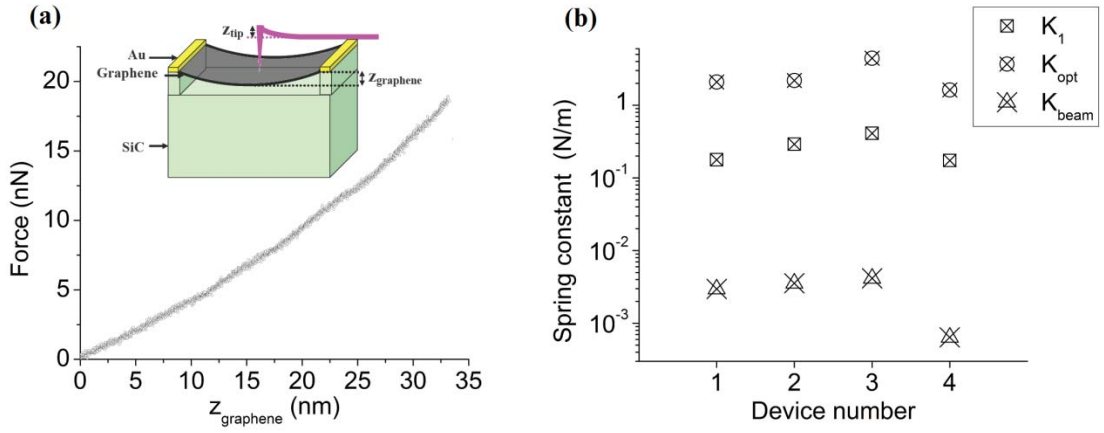

Figure 3.12: (a) Force-displacement curve for a SEG device. Inset shows schematic of the nanoindentation experiment with an AFM cantilever. z_{tip} and $z_{graphene}$ denote the tip deflection and the displacement of the graphene sheet, respectively. (b) Comparison of low-force nanoindentation spring constant, K_1, with spring constant extracted from the optically actuated resonance mode, K_{opt}, and spring constant expected from standard beam theory for a beam under no tension, K_{beam}.

In this experiment, the cantilever tip is pushed against the center of the suspended sheet in the tapping mode. As soon as the tip makes contact with the graphene, the free amplitude of vibration of the cantilever goes to zero. The applied force of the cantilever tip against the sheet causes the tip to deflect and also causes the sheet to bend. The tip displacement, the piezo displacement, and the bending of the graphene sheet are related by $z_{piezo} = z_{graphene} + z_{tip}$, where the positive z-axis points downward and all distances are measured along it.

Experiments were performed using a DI 3100 AFM. The cantilevers used for the experiment were calibrated on an Asylum Research MFP-3D AFM using a thermal noise method. The spring constants of the cantilevers employed were measured to be 9.83 N/m and 2.77 N/m. Force-displacement curves for some FSEG devices showed sudden changes in the tip deflection, suggesting either conformational modification of the device or tip slip [68]. These were not considered in the data analysis.

Figure 3.12(a) presents force-deflection curves for one of the FSEG devices that displayed reproducible behavior using multiple cantilevers. The low-force portion of the nonlinear force-displacement curves may be fit by a linear spring constant K_1. It is seen that K_1 is much larger than the spring constant expected from standard beam theory for beams under no tension, K_{beam}, given by [67] $K_{beam} = (32Ewt^3/L^3)$ (Figure 3.12(b)). We also compare K_1 with the stiffness deduced from laser interferometry experiments postanneal. The spring constant of the mode excited by optical resonance measurements is given by [69] $K\_opt = m_{eff}\omega_0^2 = (0.735\rho Lwt)(2\pi f_0)^2$. Comparing K_1 and K_{opt} for the resonators, we find that K_{opt} is greater than K_1 by roughly an order of magnitude. This suggests that local rigidity is lower than global stiffness for these devices, which is indicative of local bending and stretching during the nanoindentation experiments.

3.7 Summary

In conclusion, this chapter described a method for large-scale production of doubly clamped FSEG resonators from graphene on SiC by a photoelectrochemical wet etch process. The Raman spectrum of the suspended graphene did not suggest extensive

chemical modification by the etch. Both optical resonance measurements and nanoindentation experiments showed that the nanomechanical FSEG resonators are much stiffer than expected on the basis of standard beam theory. This stiffness may be attributed to the buckled and inverted U-shaped cross section of the beams for devices before the Ar/H_2 anneal. The resonators are under biaxial strain before release and it is conceivable that they would like to expand along the width after release. However, it is not clear why they should adopt a U-shaped profile along the width. Tension may play a role in the increased resonance frequencies of the postanneal devices. Isolation of EG from the substrate by this technique paves the way for a variety of mechanical, electronic, and optical experiments to probe the true nature of EG without interference of the substrate.

CHAPTER 4

FREE-STANDING EPITAXIAL GRAPHENE (FSEG): RAMAN SPECTROSCOPY AND ELECTRICAL TRANSPORT STUDIES

In the last chapter, we described fabrication of few-layer FSEG devices using a PEC etching process. In this chapter, we study multi-terminal FSEG devices produced from monolayer graphene on SiC using a combination of Raman spectroscopy and magnetotransport. We collaborated closely with Johannes Jobst in Prof. Heiko Weber's group at the University of Erlangen for samples as well as magnetotransport measurements [70]. From the analysis of Raman data and Shubnikov-de Haas oscillations, we conclude that the buffer layer is converted into a graphene layer and thus, monolayer graphene on SiC gets converted to a free-standing AB-stacked bilayer. The bilayer exhibits inversion-symmetry breaking because of differential doping between the layers. Additionally, lateral inhomogeneities exist in the form of domains with non-uniform mobility. The same PEC process on a pure buffer layer, however, does not yield monolayer graphene. Parts of this chapter have been adapted from a paper published in Physical Review B [71].

4.1 Introduction

It is observed that few-layer epitaxial graphene (EG) on the Si-face of on-axis SiC is AB-stacked (Bernal type) [72]. In addition, as mentioned earlier, scanning tunneling

microscopy and electron diffraction experiments [33] have revealed the presence of a buffer layer below the first graphene layer. To recap: the buffer layer, also called the zeroth layer, is composed entirely of carbon atoms and has a $(6\sqrt{3}\times6\sqrt{3})R30^{o}$ reconstruction on the (0001) Si-face of SiC. It is electrically insulating and angle-resolved photoemission spectroscopy (ARPES) [33] has established the band structure of this layer to be non-graphene-like. However, at elevated temperatures, hydrogen [33], fluorine [73], or gold [74] intercalation can transform the buffer layer into a graphene layer. In particular, hydrogen [33,75] and oxygen [76] intercalation studies of monolayer EG confirm that upon intercalation, the buffer layer is converted to a graphene layer and the multi-band electronic structure of AB stacked bilayer graphene is observed (see Figure 4.1).

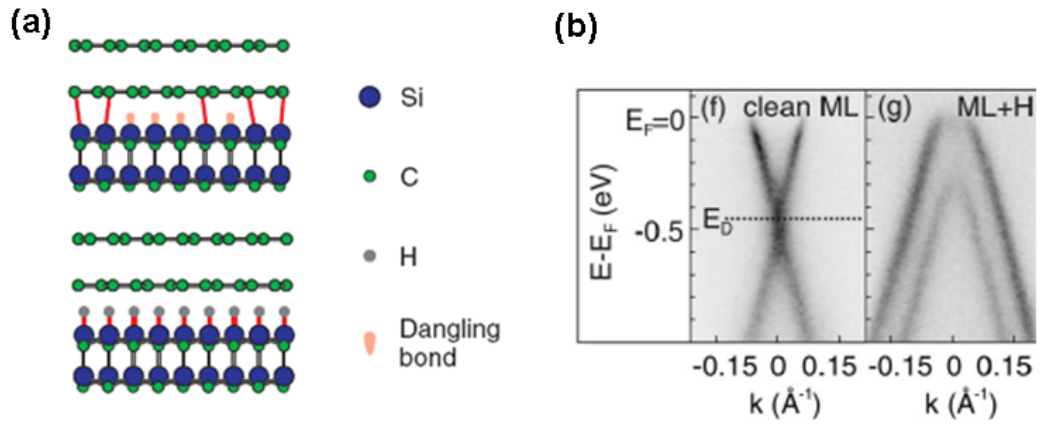

Figure 4.1: (a) Schematic showing conversion of monolayer graphene on SiC into a bilayer upon hydrogen intercalation (b) ARPES bandstructure of monolayer graphene on SiC before and after hydrogen intercalation. After intercalation, the two valence bands of the bilayer bandstructure are observed. Adapted from [32].

The interaction of graphene with the substrate causes a reduction of the charge carrier mobility μ [75]. It has been shown that this coupling can be reduced by the

intercalation procedures described above. However, the achieved mobilites in this quasi-freestanding monolayer graphene (QF-MLG) [75] and quasi-freestanding bilayer graphene (QF-BLG) [77,78] are well below the values observed for suspended exfoliated graphene, devoid of any substrate interactions [10]. It is thus desirable to investigate similar free-standing epitaxial graphene (FSEG) structures electrically.

4.2 Device fabrication

For the PEC etching process, it is important that the graphene is grown on an electrically conductive substrate, whereas for electrical characterization, the substrate needs to be insulating. We, therefore, used three types of substrates: semi-insulating SiC implanted with nitrogen rendering it n-type close to the surface, semi-insulating SiC implanted with aluminum rendering it p-type, and bulk n-type SiC. In the former two substrates, the implanted conductive region is chosen such that it is removed completely during the PEC etch, leaving behind only insulating SiC. The latter becomes insulating below ~70K when the nitrogen dopants freeze out. We describe next our fabrication steps for the different substrates.

4.2.1 Growth and patterning of graphene

EG devices were fabricated on the hydrogen etched Si-face of of n-type 6H-SiC substrates by thermal decomposition at 1750°C under 1 bar of argon atmosphere following the process described in [24]. In addition, we also fabricated samples with only the buffer layer for which the growth temperature was reduced to 1450°C. The structures were patterned using electron-beam lithography where the poly-(methyl

methacrylate) (PMMA) resist served as etch mask during the oxygen-plasma process employed to pattern the graphene. The contact areas were fabricated by evaporation of Ti/Au (5nm/50nm) and lift-off technique. We also fabricated large-area Hall bars and studied the transport properties after exposing them to the PEC etching conditions. This was performed to investigate if the PEC etching process had an adverse effect on the graphene.

For non-conductive substrates, semi-insulating SiC was implanted with nitrogen ions, rendering it n-type. We used seven implantations at energies from 280kV to 20kV (high energies were implanted first in order to prevent a smearing of the profile). The implantation was performed at 500°C to anneal point defects. The dose profile for nitrogen implantation is described in Figure 4.2(a). For p-type implantation, aluminum was used with the associated dose profile shown in Figure 4.2(b). In both cases, the topmost 60 nm of the SiC (depicted by the shaded grey area in Figure 4.2) were removed during the hydrogen etch process prior to graphene growth. Activation of the dopants and graphene growth were performed simultaneously at 1750°C. Subsequently, graphene was patterned and contacts were evaporated as described previously.

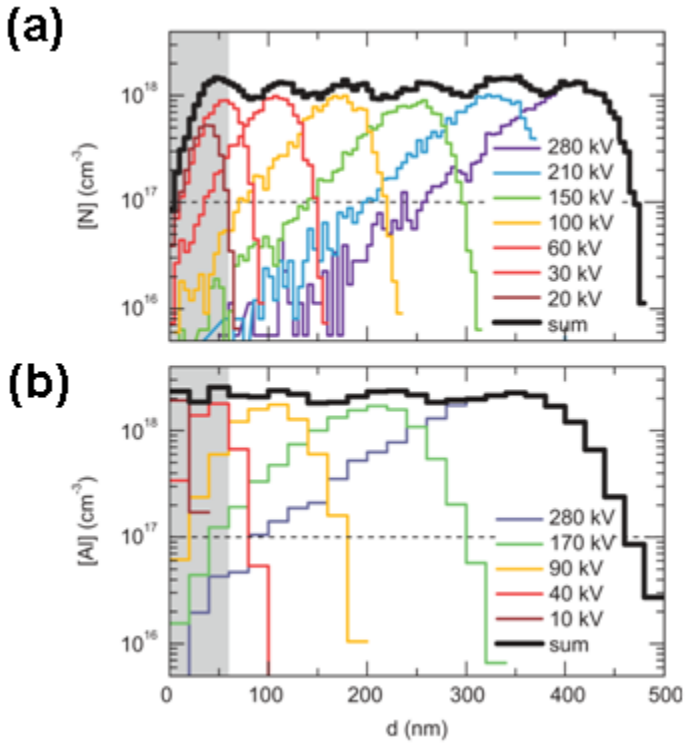

Figure 4.2: The implantation of box profiles with doping concentrations well above the vanadium compensation ($[V] \approx 10^{17}\mathrm{cm}^{-3}$, dashed lines) yields conductive wells at the SiC surface. (a) Implantation of nitrogen ions creates an n-doped region of d ≈ 450nm thickness. We used seven shots at energies from 280kV to 20kV to create a smooth doping profile. (b) Due to shallower profiles of aluminum implantation, less shots are necessary for p-doped wells. The topmost ~60nm of SiC were consumed during a subsequent hydrogen etch of 90s (grey areas).

4.2.2 PEC etching

For n-type SiC – both nitrogen-implanted semi-insulating SiC (NI-SiC) and n-type substrates – the PEC etching followed the procedure described previously in chapter 3. In case of aluminum-implanted semi-insulating SiC (AI-SiC), no ultraviolet light was required for the etching process because the holes required for the reaction that leads to the dissolution of SiC are already present in the p-type SiC [79]. However, the depletion region and the resulting downward bending bands at the p-type

semiconductor/solution interface [80] necessitate much higher voltages (3.5-6.5 V) for the reaction to take place. This has a potential for competing reactions in the form of electrolysis of water or hydrolysis of the metal contact pads. In order to protect the metal contacts, the SiC underneath the contact pads was protected using a metallic shadow mask during ion implantation and thus remained insulating.

4.3 Magnetotransport phenomena and scattering lengths in graphene

In this brief interlude, an introduction to magnetotransport phenomena and various scattering lengths in graphene is provided, which will help understand the results described later in the chapter.

First, Shubnikov-de Haas oscillations (SdHO) are described. These are magnetoresistance oscillations which occur in a two-dimensional electron (or hole) gas under high magnetic fields. In the case of few-layer graphene, the phase of these oscillations is intimately tied to the electronic bandstructure and in fact, may be used to distinguish monolayer and bilayer graphene. The other phenomenon discussed in this section is weak localization (WL). This are related to the wave nature of the electron and is determined by the phase coherence length in the sample.

The discussion follows [81] closely. Electrons have a dual wave and particle nature. The mean free path, l_m, denotes the distance an electron travels before its initial momentum is destroyed. Not every collision destroys the momentum of the electron. Only large-angle scattering events affect the momentum significantly. Thus, momentum relaxation time, τ_m, is usually larger than the time between successive collisions.

The phase coherence length, l_ϕ, denotes the length over which the initial phase of the electron wave is destroyed. The phase of the electron may also be affected by collisions. When the scatterer is static, i.e. has no internal degrees of freedom, the collision is phase-conserving. Most impurity potential scattering does not affect the electron phase. Collisions which randomize electron phase include electron-phonon collisions, electron-electron interactions and electron-magnetic impurity interactions. In summary, phase relaxation is caused not by rigid scatterers, but by fluctuating ones. The phase coherence length is related to the phase relaxation time, τ_ϕ, by the relation $l_\phi = \sqrt{D\tau_\phi}$, where D is the diffusion coefficient.

4.3.1 Shubnikov-de Haas oscillations (SdHOs)

In the presence of a magnetic field, the density of states of a two-dimensional electron gas (2DEG) splits into discrete levels called Landau levels. In case of monolayer graphene, the Dirac-Weyl equation may be solved in the presence of a magnetic field to obtain the energy spectrum [82]

$$E_N = sgn(N)\sqrt{2\hbar v_F^2 eB|N|}, \qquad N = 0, \pm 1, \pm 2, \ldots$$

where N is the Landau level index. The energy is measured with respect to the Dirac point. Positive N corresponds to electrons and negative to holes. Each level has a fourfold degeneracy – 2 from electron spin and 2 from the valley index.

In case of bilayer graphene, the eigenenergies in the presence of a magnetic field are given by [83]

$$E_N = sgn(N)\frac{\hbar eB}{\gamma_1/2v_F^2}\sqrt{|N|(|N|+1)}, \qquad N = 0, \pm 1, \pm 2, \ldots$$

where $\gamma_1$is the interlayer hopping energy. In this case, the $N = 0$ level is eightfold degenerate because of the extra layer degree of freedom, while the others are fourfold degenerate. For a conventional 2DEG, the Landau spectrum is given by [84]

$$E_N = \left(N + \frac{1}{2}\right)\frac{\hbar eB}{m_c} + E_s, \qquad N = 0,1,2, \ldots$$

where m_c is the effective cyclotron mass and E_s is the spin-splitting term. The sequence of the Landau levels in these three systems is compared in Figure 4.3. It may be observed that in case of monolayer and bilayer graphene, there exists a Landau level at zero energy. Additionally, the Landau levels in graphene are not equally spaced in energy.

In the semi-classical picture, electrons confined to a plane in a perpendicular magnetic field travel in circular orbits. Each Landau level may be thought of as being associated with a cyclotron orbit of a certain radius in the semi-classical picture (see Figure 4.4). The number of electron states in each Landau level (excluding spin degeneracy) is given by $n_L = eB/h$. The occupation of Landau levels is characterized by a filling factor $\nu = n/n_L$, where n is the electron density. For a given electron density, a certain number of Landau levels are occupied. As the magnetic field is increased, the number of electron states in each Landau level increases and, as a consequence, the filling factor changes. In the semi-classical picture, this may be interpreted as an increase in the radius of the cyclotron orbit with increase in the magnetic field strength. As the Fermi level of the system passes across a Landau level, an oscillatory behavior in the sample resistance is observed.

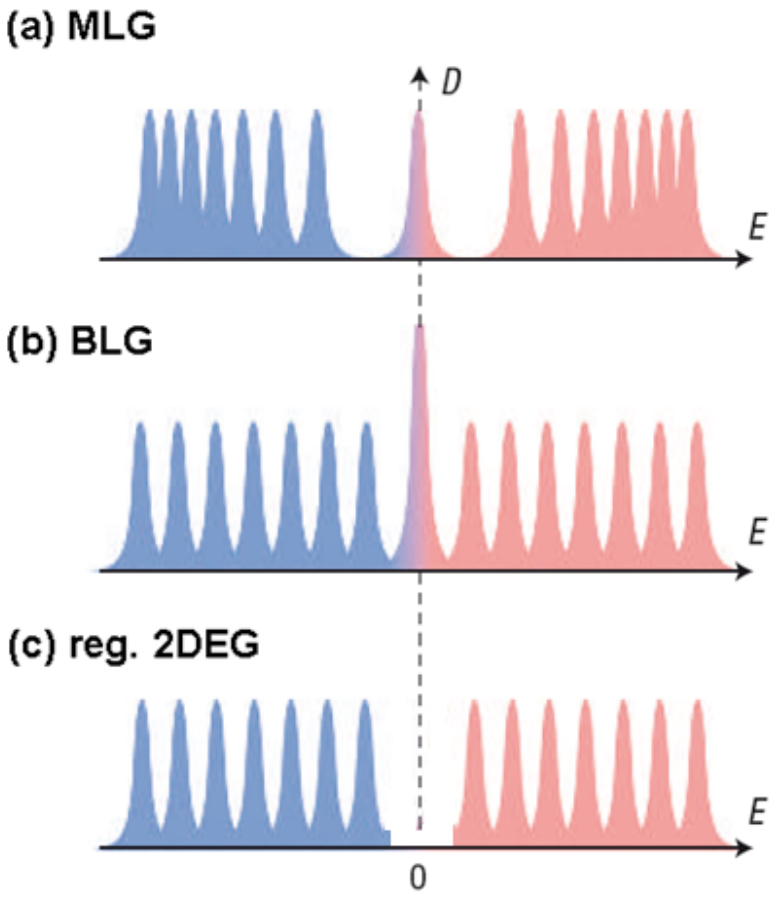

Figure 4.3: Landau level spectrum (a) Monolayer graphene (b) Bilayer graphene (c) Conventional 2DEG (Adapted from [12])

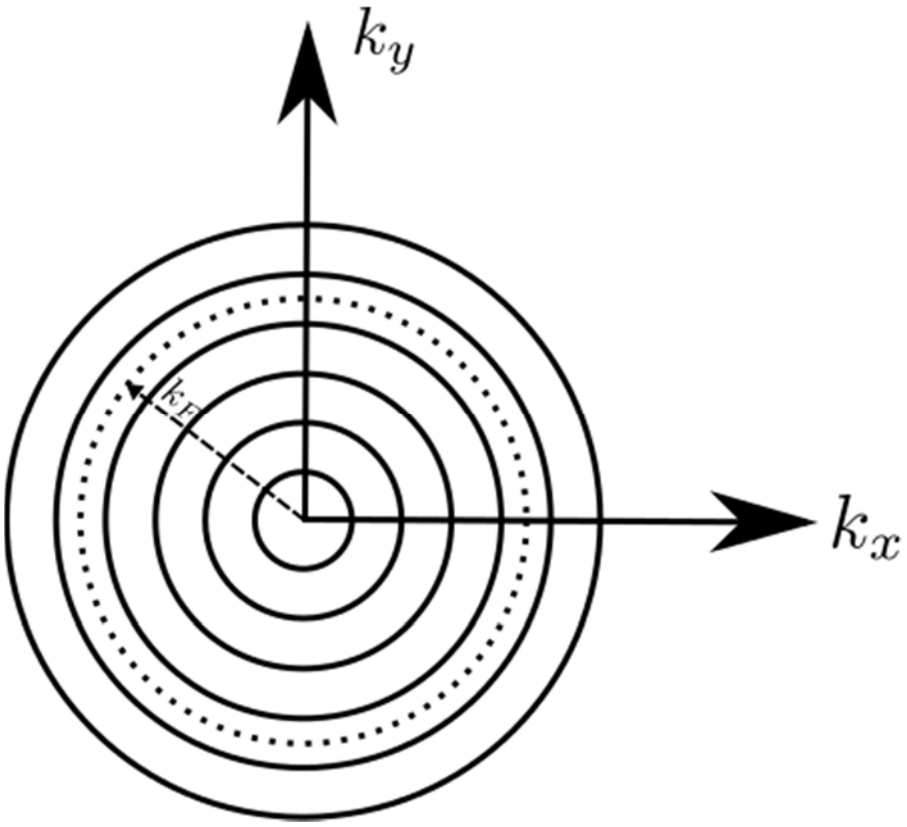

Figure 4.4: Semi-classical picture of electron orbits in a magnetic field. Each Landau level corresponds to a single cyclotron orbit. The Fermi circle is indicated by the dotted line. As the magnetic field increases, the radius of the orbit increases and the Landau levels pass across the Fermi circle. This causes the oscillatory phenomena.

The broadening of a Landau level is related to the scattering of electrons. In order to be able to see the oscillatory behavior, the Landau levels must be well-separated. Since the spacing between the Landau levels is related to the magnetic field, this provides a condition on the strength of the field. For SdHOs to be observed, $B\mu \gg 1$, where μ is the mobility of the charge carriers, which is related to the scattering time [81]. Thus, the emergence of SdHOs provides an estimate for the mobility of the sample.

The oscillating part of the resistance, $\Delta\rho_{xx}$, in the SdH effect has the form [85]

$$\Delta\rho_{xx} \sim \cos\left[2\pi\left(\frac{B_0}{B} - \gamma\right)\right]$$

where B_0 is the characteristic frequency of oscillation and $2\pi\gamma$ is Berry's phase. A fan diagram plots the Landau index N against $1/B_N$, where B_N is the magnetic field at which the maxima or minima of the resistance oscillation occurs. The maxima of resistance occur when the Fermi level lies at the center of a Landau level. Since the number of electron states in a Landau level is known (n_L multiplied by the degeneracy), we can compute the electron density in the sample from the slope of the fan diagram. The slope is, thus, related to the electron density by the expression [81]

$$n_s = \frac{4e}{h}\frac{\Delta N}{\Delta\left(\frac{1}{B_N}\right)}$$

Also, we can see that maximum in $\Delta\rho_{xx}$ corresponding to the Landau level of index N occurs at $B_{N,max}$ given by $2\pi\left(\frac{B_0}{B_{N,max}} - \gamma\right) = 2\pi N$. Thus, the fan diagram yields a second piece of information, namely, Berry's phase modulo 2π, which may be obtained from the axis intercept. This can help distinguish between monolayer and bilayer graphene, which have Berry's phase of π and 2π respectively on account of their linear and quadratic band dispersions [9,86-88].

4.3.2 Weak localization (WL)

When the sample size is comparable to the phase coherence length, l_ϕ, electron transport may not be treated in the diffusive picture. The wave nature of the electron needs to be taken into account. The phenomenon of weak localization (WL) refers to the decrease in magnetoresistance observed at low magnetic fields compared to the

zero field value. It occurs because of the increased probability of backscattering at zero magnetic field. When an electron travels from one point to another in a phase-coherent manner, the probability for the event is obtained by squaring the sum of probability amplitudes for various possible paths: $P(\vec{r} \rightarrow \vec{r}') = |\Sigma A_i|^2$. Usually, the phases of the different paths are random and interference effects cancel out on the average. However, in case of backscattering, the initial and final states are the same. An electron which backscatters to the initial state can always do so via two possible paths while traversing the same set of scatterers as shown in Figure 4.5. One represented by the solid line is in the clockwise (CW) direction, whereas the other shown with dotted lines is counter-clockwise (CCW). In the absence of time-reversal symmetry breaking, the phases of the electron waves along the two paths are identical and hence the square of the sum is equal to the sum of the squares: $P(\vec{r} \rightarrow \vec{r}) = |A_C + A_{CCW}|^2 = |A_C + A_C|^2 = 4|A_C|^2$. Thus, the probability for back-scattering is enhanced and resistance is high at zero field. When a magnetic field is applied, the time-reversal symmetry is broken, which causes the two paths to have different phases and backscattering is reduced.

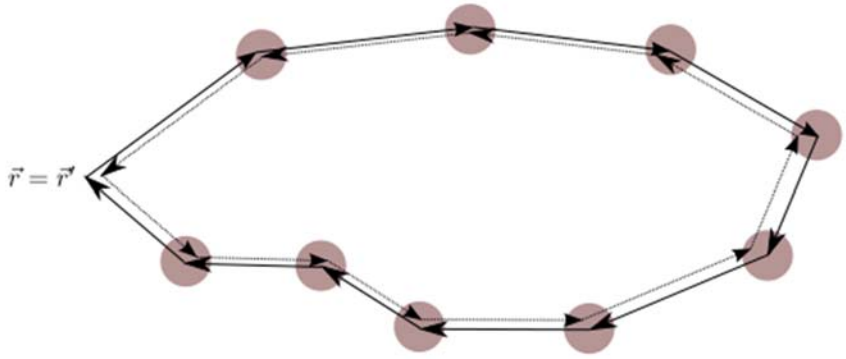

Figure 4.5: In the phase coherent transport regime, electron backscattering event can occur via a clockwise (CW) or a counter-clockwise (CCW) path. In the absence of

time-reversal symmetry breaking, the phases of the two paths are equal and backscattering is enhanced.

In case of monolayer graphene, there is a slight complication. Because of the pseudospin of the charge carriers, in the absence of a magnetic field, the CW and CCW paths have a phase difference of π, which destroys backscattering. So, in fact, weak anti-localization (WAL) is expected in monolayer graphene [89,90]. In case of bilayer graphene, with a Berry's phase of 2π, usual WL behavior is expected [91].

The WAL/WL behavior in graphene is affected by elastic scattering processes [89-92]. In particular, intravalley scattering caused by long-range potential suppresses the localization corrections. However, in the presence of intervalley scattering, WL behavior is restored. Intervalley scattering is caused by point defects or short-range scatterers, which are inevitably present in all but the highest quality graphene samples. Thus, by studying the magnitude of the WL, the phase coherence length, l_ϕ and the intervalley scattering length, $l_{iv} = \sqrt{D\tau_{iv}}$ (τ_{iv} is the intervalley scattering time) can be estimated.

4.4 Results and discussion

Now, we are ready to discuss the results obtained from characterization of the FSEG devices. First, we present results on large-area Hall bars which were fabricated to investigate if the PEC etching process had an adverse effect on the graphene. Next, we present Raman spectroscopy and magnetotransport results on multi-terminal FSEG devices fabricated on n-type SiC substrate. The subsequent section describes results of the PEC process on a sample with just the buffer layer. The final section discusses

devices produced on NI-SiC and AI-SiC, which turned out to be extremely difficult to measure because of electrostatic discharge issues.

4.4.1 Effect of PEC etching conditions on transport properties

In order to investigate the impact of the PEC etching on the transport properties, large-area Hall bars ($1000 \times 200\mu m$) were fabricated, in order to avoid underetching. One Hall bar was studied directly after preparation ($n = 7.8 \cdot 10^{12}$ cm^{-2}, $\mu = 820$ cm^2/V-s); one was immersed in KOH solution for 1.5 hours with a voltage of 900 mV applied ($n = 4.6 \cdot 10^{12}$ cm^{-2}, $\mu = 1250$ cm^2/V-s); the third one was exposed to ultraviolet (UV) light in addition to KOH and the applied voltage ($n = 3.9 \cdot 10^{12}$ cm^{-2}, $\mu = 1670$ cm^2/V-s). From the transport measurements, we conclude that the PEC etching has no negative effect on the mobility (the increased mobility is probably related to the decrease of n, which might be either a doping or an ageing effect). Moreover, evaluation of weak-localization data confirms that the intervalley-scattering length [89,90] $l_{iv} \approx 95$ nm – the average length between two short range scatterers – is similar for all three devices. Consequently, no additional (short-range) defects are created by the PEC treatment in the non-underetched Hall bars.

4.4.2 FSEG devices on n-type SiC substrate

Figure 4.6 shows examples of two-terminal and multi-terminal FSEG devices produced using the PEC etching technique. It is possible to obtain large free-standing devices spanning several tens of microns as demonstrated by the Hall bar in Figure 4.6(b). Sometimes, tears were seen, indicated by the arrows in Figure 4.6(a). It is

unknown if these were present originally in the grown graphene or were developed during the etching process. In addition, small patches with bright contrast (shown encircled in Figure 4.6(a)) were observed occasionally below the graphene in the SEM images. These have been identified as SiC residue using energy-dispersive X-ray spectroscopy (EDX) [93].

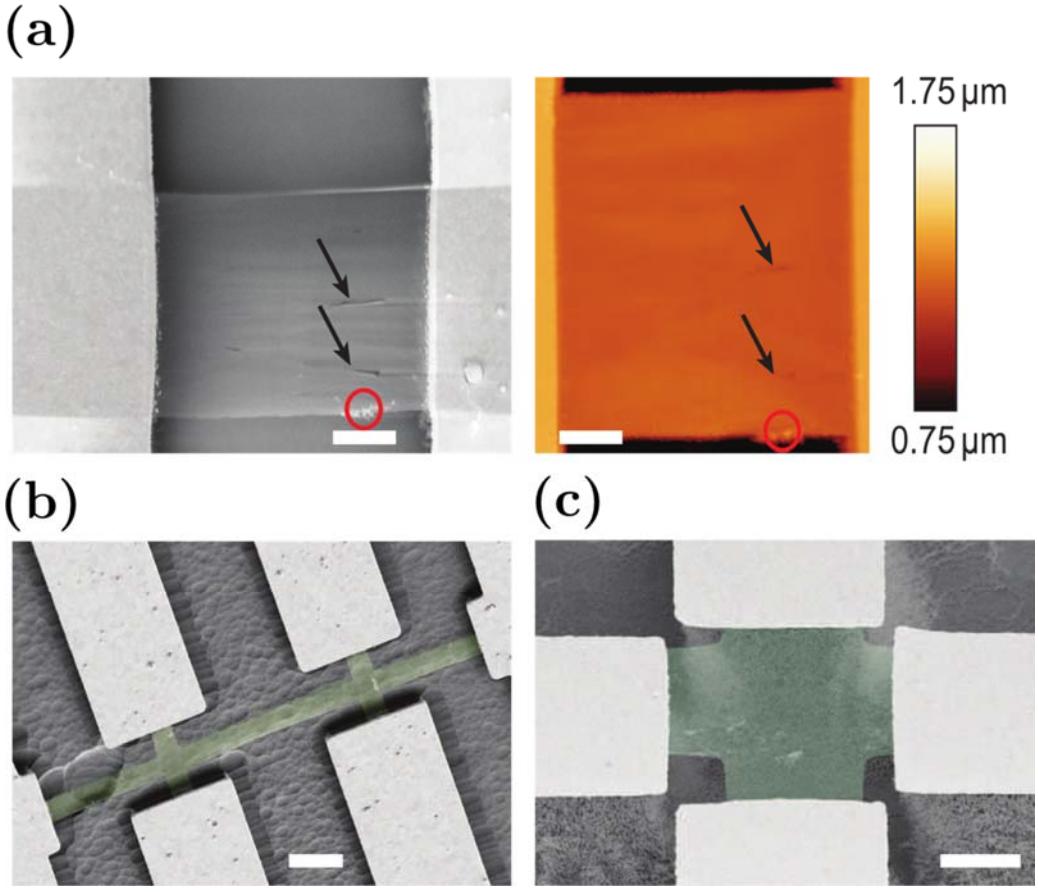

Figure 4.6: Scanning electron microscope (SEM) and atomic force microscope (AFM) images of two-terminal and multi-terminal FSEG devices. (a) Two-terminal device. Left: SEM image taken using a 45^{o} angle stage. Right: AFM image. Scale bars – 1 µm. Tears are visible in the device and are indicated by arrows. The circle marks the location of SiC residues, which are left behind after the etch. (b) Multi-terminal device in Hall bar geometry. Graphene is shown in false color for improved contrast. Scale bar – 5 µm. (c) Multi-terminal device in Hall cross geometry. Scale bar – 2 µm.

4.4.2.1 Raman spectroscopy of FSEG devices

Figure 4.7(a) shows Raman spectra of the graphene on SiC substrate and the free-standing devices obtained using a confocal Raman microscope with a 100 ×(N.A. 0.9) objective and a laser excitation of 488 nm (argon-ion laser). The FSEG devices showed *G* and *2D* bands characteristic of graphene. A small *D* peak was also seen in some cases. Compared to EG on SiC, the *G* and *2D* peaks of FSEG are red-shifted, indicating that the compressive strain present in the graphene on the substrate is released after suspending the structures, as has been noted earlier in Chapter 3. In addition, the signal strength of the peaks was enhanced in the FSEG devices and little background from the second-order SiC Raman peaks was detected, confirming the suspended nature of the devices.

Closer observation reveals that the lineshape of the broad *G* mode in FSEG could be approximated very well as a sum of two Lorentzian components. In fact, spatial Raman mapping revealed explicit splitting of the *G* mode over most area of the devices. We discuss next four possible reasons for the splitting of the *G* band. First, uniaxial strain in monolayer graphene may cause the *G* band to split into two components denoted by G^+ and G^- (G^+/G^- denotes the higher/lower energy component of the *G* peak) [94,95]. For graphene under uniaxial strain, the intensities of the G^+ and G^- modes have a sinusoidal dependence on the angle between incident and scattered polarizations. Thus, the lineshape would be expected to differ significantly for light scattered along orthogonal polarizations [94,95]. Figure 4.7(b) displays Raman spectra acquired with $\widehat{\boldsymbol{e_S}}$ parallel and perpendicular to $\widehat{\boldsymbol{e_I}}$, where $\widehat{\boldsymbol{e_S}}$ and $\widehat{\boldsymbol{e_I}}$ denote the polarization vector of scattered and incident light respectively. We see no

observable dependence of the *G* band lineshape on the polarization direction. In addition, for uniaxially strained graphene, both G^+ and G^- modes would simultaneously red-shift (tensile strain) or blue-shift (compressive strain). However, in FSEG the G^+ and G^- modes shifted in opposite directions from the zero-strain position of ~1580 cm^{-1}. Thus, the model of uniaxial strain in monolayer graphene does not explain the observed splitting of the *G* mode.

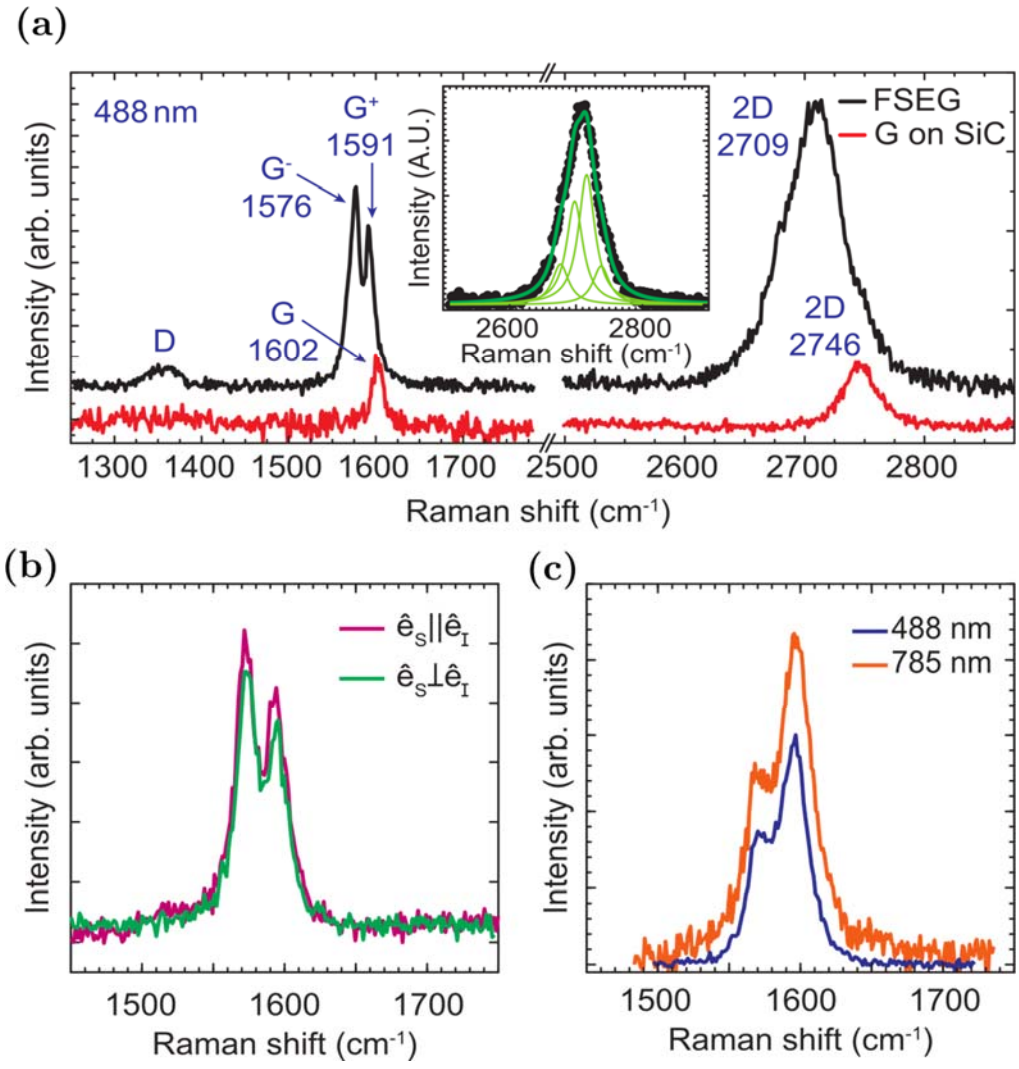

Figure 4.7: (a) Raman spectra using 488 nm excitation for FSEG (black) and graphene on SiC substrate (red). Background from the SiC Raman modes has been subtracted. The *G*, *2D* and *D* bands are indicated. Red-shifts in the FSEG bands are apparent. Inset shows *2D* band of FSEG fit using four Lorentzians of FWHM 30 cm-1. (b)

Polarization-dependent Raman spectra of FSEG. Pink (green) curve shows *G* band when the polarization of scattered light, $\widehat{\boldsymbol{e_S}}$, is parallel (perpendicular) to that of incident light, $\widehat{\boldsymbol{e_I}}$. (c) Raman spectra of FSEG using two different excitation energies – 488 nm (2.54 eV, blue) and 785 nm (1.58 eV, orange). No dispersion was observed.

A second possibility is chemical modification or introduction of defects in the graphene. This causes the appearance of the defect-activated *D'* band in graphene at ~1620 cm^{-1}, which corresponds to an intra-valley scattering event due to a LO phonon [36] and could lead to an apparent modification of the *G* peak lineshape. However, the position of the observed G^+ peak is much below 1620 cm^{-1}. Secondly, because of the larger electron-phonon coupling for the zone-boundary iTO branch in graphene, the intensity of the *D* peak would be higher than the *D'* peak [96], which is not true in our case. In addition, unlike the *D'* peak [97], the G^+ mode does not exhibit any dispersion with excitation energy, as shown in Fig. 4.7(c). Thus, we unambiguously discount the *D'* mode as an explanation. Third, a splitting of the *G* band due to symmetry breaking by molecules [98] in monolayer graphene is also eliminated as a possibility because the *2D* peak width in FSEG is much larger than that expected for monolayer graphene.

Fourth, and in keeping with the recent demonstrations of quasi-free-standing epitaxial graphene by various intercalation procedures [33,73,74,76], we offer an interpretation of our observations by hypothesizing the conversion of monolayer-EG into a free-standing bilayer after the PEC etching process. It has been confirmed by ARPES that hydrogen intercalation converts monolayer EG grown on top of the buffer (zeroth) layer into AB stacked bilayer graphene (Figure 4.1). Thus, it is reasonable to assume that the bilayer graphene obtained after the PEC etching process is also AB

stacked [77]. The splitting of the *G* peak in Bernal stacked bilayer graphene can be a consequence of inversion symmetry breaking [99-102]. Breaking of inversion symmetry may be caused by different charge carrier concentrations in the top and bottom layers [96,99,100,103-106]. In AB stacked bilayer graphene, the phonon modes of the top and bottom layers are coupled. There are two phonon modes at the zone center – one corresponding to the in-phase (IP) motion of atoms in the two layers and another corresponding to an out-of-phase (OP) motion (Figure 4.8(b)). In pristine bilayer graphene, only the IP mode having even parity is Raman active and corresponds to the single *G* peak; the OP mode is infrared active because of odd parity. When inversion symmetry is removed, the new phonon eigenstates of bilayer graphene are superpositions of the original IP and OP modes. Thus, both of the new eigenmodes become Raman active because of the even symmetry IP component. This explains the splitting of the *G* peak into G^+ and G^- modes. Figure 4.8(a) shows how a backgate may be used to induce unequal charges on the top and bottom layers of bilayer graphene causing splitting of the *G* mode [99]. In accordance with observations, for certain doping levels, the G^+ and G^- modes may straddle the pristine bilayer *G* peak at ~1580 cm^{-1} [101]. Similar splitting has been reported for QF-BLG after oxygen intercalation [76]. Further support for the coupled bilayer hypothesis comes from comparison of the *2D* peak before and after the PEC etch. The *2D* peak of the FSEG devices is broader – full-width at half-maximum (FWHM) 56 cm^{-1} vs 31 cm^{-1} for graphene on SiC – and may, in fact, be fit by multiple Lorentzians (see inset of Figure 4.7(a)). It has been shown that, in case of bilayer graphene, high doping can lead to a broad *2D* peak with indistinct and/or reduced splitting because of electron-

electron correlation effects [107,108], which may explain the differences between the *2D* peak lineshape of FSEG and exfoliated bilayer graphene, where the *2D* peak splitting is more explicit.

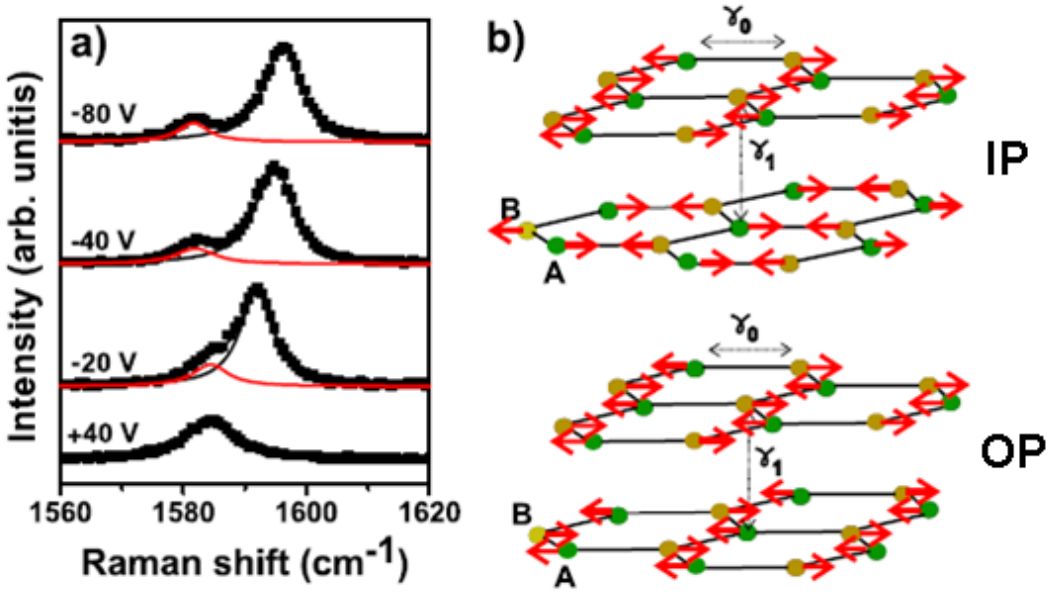

Figure 4.8: (a) Splitting of the *G* peak as a consequence of differential doping between the top and bottom layers of bilayer graphene induced by a backgate (b) Schematic showing the in-phase (IP) and out-of-phase (OP) modes. Adapted from [99].

In order to investigate the splitting of the *G* peak with lateral resolution, we performed Raman maps. Figure 4.9 shows spatial Raman maps for a suspended Hall bar indicating the positions of the two split modes G^+ and G^-, the splitting pos(G^+)-pos(G^-) and the intensity ratio I(G^+)/I(G^-). The maps were obtained along the centerline of the device using 785 nm excitation and a pixel resolution of 0.7 μm. It is obvious that not only the *G*-band splitting, but also the individual positions of the split modes vary strongly across the device. The variation of the positions together with a variation of the intensities suggests significant lateral doping inhomogeneities in the

bilayer sample [101]. This finding is similar to that observed in bilayer graphene intercalate produced using ferric chloride [109]. Moreover, these charge variations are corroborated by the magnetotransport measurements presented below.

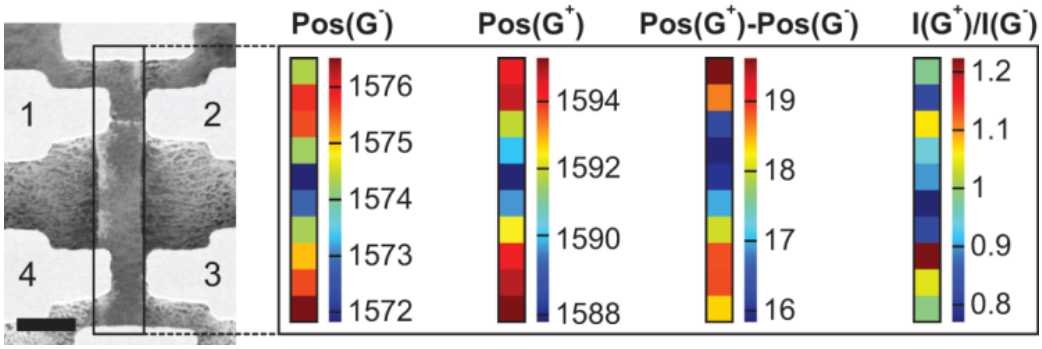

Figure 4.9: Raman maps showing positions of G^- and G^+ modes (*Pos(G⁻)* and *Pos(G⁺)*), the splitting between the peaks (*Pos(G⁺)-Pos(G⁻)*) and ratio of integrated peak intensities (*I(G⁺)/I(G⁻)*) for a FSEG Hall bar device. Maps were produced using a 785 nm excitation, with each pixel corresponding to 0.7 μm. Scale bar for SEM image is 1 μm.

4.4.2.2 Magnetotransport of FSEG devices

We investigated the transport properties of freely suspended Hall bars under cryogenic vacuum in weak and strong fields using low frequency lock-in techniques. In the weak field regime, the Hall effect charge carrier density n_H can be calculated from the slope R_H of the linear trend (cf. Figure 4.10(a)) of the Hall resistance $R_{xy}(B)$, as $n_H = 1/R_H e$ (this procedure assumes a homogeneous conductor). We computed a temperature-independent $n_H \approx 2.5 \cdot 10^{12}$cm^{-2} from the Hall resistance measured in two different contact configurations (i.e. contacts 1-2 or 3-4 in Figure 4.9). From the longitudinal resistivity ρ_{xx} (measured either between contacts 2-3 or 1-4 in Figure 4.9) an average Hall mobility $\mu_H = 1/en_H\rho_{xx} \approx 350$ cm^2/Vs was then calculated.

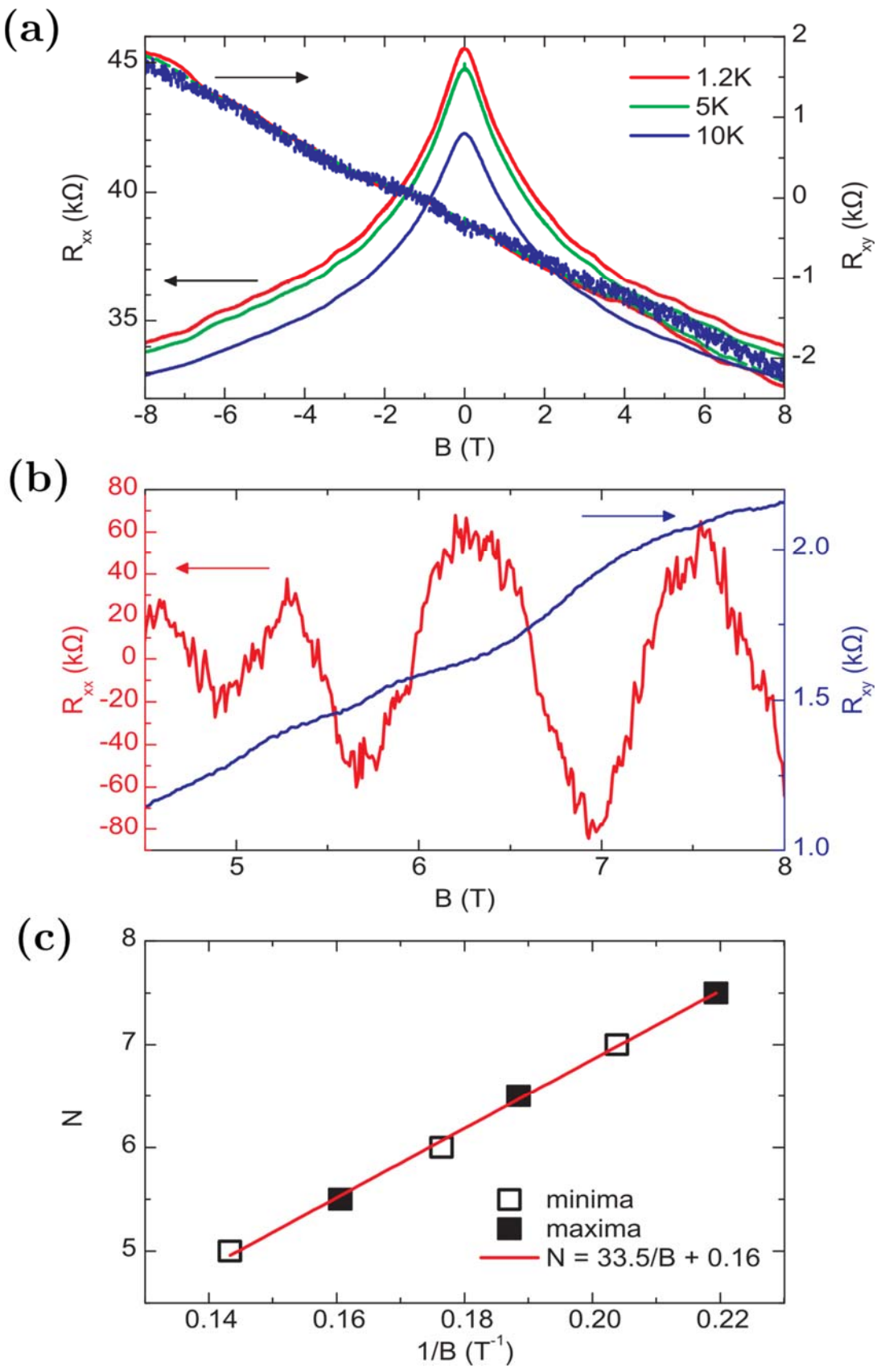
(a)
45
40
35
2
1
0
-1
-2
-8
-6
-4
-2
0
2
4
6
8
B (T)
R_xx (kΩ)
R_xy (kΩ)
1.2K
5K
10K
(b)
80
60
40
20
0
-20
-40
-60
-80
2.0
1.5
1.0
5
6
7
8
B (T)
R_xx (kΩ)
R_xy (kΩ)
(c)
8
7
6
5
N
0.14
0.16
0.18
0.20
0.22
1/B (T^-1)
minima
maxima
N = 33.5/B + 0.16

Figure 4.10: (a) The longitudinal resistance R_{xx} shows a weak-localization peak around $B = 0$ and an oscillatory behavior at high fields and low temperature. The Hall resistance R_{xy} is approximately linear and temperature-independent. (b) A zoom to 1.2K data in (a) reveals pronounced Shubnikov-de Haas oscillations in the longitudinal resistance δR_{xx} after a smooth background is subtracted. No conspicuous plateaus are visible in R_{xy}. (c) The evaluation of the Landau-level index N of the extrema over their $1/B$-positions yields a linear trend (for the maxima N is reduced by 0.5 in this diagram). The charge carrier density can be calculated from the slope of this line as $n \approx 3.3 \cdot 10^{12}$cm^{-2}. The axis intercept of $\beta = 0.16 \pm 0.14$ indicates AB-stacking where $\beta = 0$ is expected.

This rather low mobility value is inconsistent with the occurrence of Shubnikov-de Haas (SdH) oscillations, which were observed for $B > 4.5$T in the sample (Figure 4.10(a,b)). In Fig. 4.10(a), the presence of SdHOs of low amplitude is masked by a large negative magnetoresistance. After subtracting a smooth background, however, SdH oscillations are clearly visible (Figure 4.10(b)). As SdHOs can only develop in high-mobility samples in strong fields when $\mu B \gg 1$, this implies $\mu > 2200$cm^2/Vs for the sample. The fan diagram for the resistance oscillations is shown in Fig. 4.10(c). Here the $1/B$-positions of the resistance extrema are plotted against their corresponding Landau level (LL) index N (note that in Figure 4.10(c), N is reduced by 0.5 for the maxima in order to increase the number of points for the subsequent fit). The linearity of the plot confirms that the observed oscillations are indeed SdH oscillations. Furthermore, the density of the high-mobility charge carriers that cause the oscillations may be computed from the slope B_0, of the fan diagram [86,110] using $n_{SdH} = \frac{2e}{\pi\hbar} B_0$, which yields $n_{SdH} \approx 3.3 \cdot 10^{12}$cm^{-2}. This is close to the carrier density obtained from the weak field regime, but implies a mobility of 270 cm^2/Vs, which is too low to give rise to SdH oscillations, as mentioned before. These discrepant values

of mobility suggest that the sample is electrically inhomogeneous and comprises domains of high mobility which cause SdHOs as well as domains of reduced mobility which give rise to the high resistivity of the FSEG. The occurrence of strong inhomogeneity patterns is in contrast to QF-BLG after hydrogen intercalation. This difference probably arises due to the different temperatures and chemical environments during intercalation and PEC etching. While the former is a high temperature process in a defined ambient, PEC etching is a room-temperature photochemical process in an aqueous solution. Consequently, the graphene may be doped by adsorbates after the sp^3-bonds between SiC and buffer layer are broken.

In addition to information about the charge carrier density, the fan diagram (Figure 4.10(c)) can give insight into the layer number and stacking of the studied graphene material. For bilayer graphene with AB-stacking, an axis intercept of $\beta = 0$ is expected for the linear trend. Note that for monolayer graphene [111] or decoupled layers [112], $\beta = 0.5$ is expected. The observation of $\beta = 0$ in Figure 4.10(c), which corresponds to a Berry's phase of 2π, thus confirms that the FSEG is indeed AB-stacked bilayer graphene. This finding is in line with recent magnetotransport measurements of QF-BLG created via hydrogen intercalation [77,78].

4.4.3 PEC etching of buffer layer

Since MLG is transformed to a freestanding bilayer by the PEC etch, it seems natural to assume that starting from buffer layer will yield a freestanding monolayer. However, we find that a pure buffer layer cannot withstand the PEC etching. The reason for the disappearance of the buffer layer is unclear, but the presence of defects

and tensile strain in the layer [75] could lead to mechanical failure, causing it to collapse during the etching process. Figure 4.11 shows the result of an etching experiment with nominally pure buffer layer. In addition to the vanishing of the buffer layer, we observe graphene nanoribbons. They result from small graphene areas that nucleated at the step edges in addition to the buffer layer [24]. Figure 4.11(b) shows how the nanoribbons follow the topography of the SiC step edges that are visible below the metal contacts. The graphitic nature of the ribbons is confirmed by the Raman spectrum in Figure 4.11(c). This additional finding may provide a route for the production of suspended graphene nanoribbons, which are unaffected by the underlying substrate and thus allow to study in detail the properties of confined electrons in graphene.

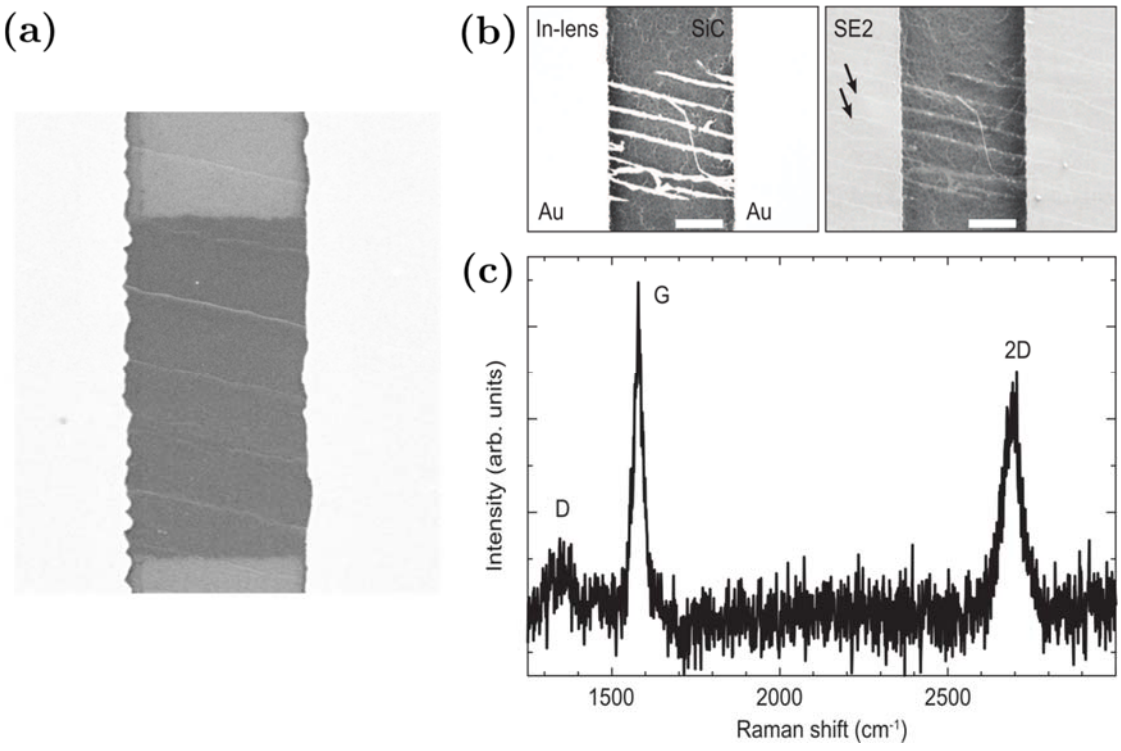

Figure 4.11: PEC etching of buffer layer. (a) SEM image of buffer layer sample on SiC. The device width is ~2.2 μm. (b) SEM images of a buffer layer sample after PEC

etching. The image on the left (right) is acquired with the in-lens (secondary electron SE2) detector. Free-standing graphene nanoribbons suspended between the gold pads can be clearly seen in the left image. In the right image, arrows indicate step edges on the SiC visible through the gold contacts. The alignment of the graphene nanoribbons along the step edges is evident. (c) Raman spectrum showing the graphitic nature of the nanoribbons.

4.4.4 FSEG devices on implanted semi-insulating SiC

4.4.4.1 Results on nitrogen implanted SiC (NI-SiC)

The conditions for PEC etching of NI-SiC were similar to those for the n-type SiC described earlier. Also, the FSEG devices showed very comparable Raman spectra to those obtained on n-type SiC substrates. Transport measurements, in contrast, were more difficult to perform on FSEG structures produced from NI-SiC than from n-type SiC. Structures tended to rupture during electrical contacting, evacuation of the measurement chamber or cool-down. We attribute this to electrostatic discharges where all the power is dissipated in the suspended graphene sheet as the substrate is insulating. Therefore, the measurement yield of FSEG devices from NI-SiC was very low (~1% of the structures could be measured). In contrast, on n-type SiC, which is conductive at room temperature, most of the devices survived contacting and thermal cycling. Nevertheless, Figure 4.12 shows the charge carrier concentration and the mobility of a FSEG Hall cross (SEM micrograph in Figure 4.12) on NI-SiC, extracted using Hall effect and conductivity measurements at low magnetic fields. The transport properties are fairly temperature-independent as expected for suspended graphene [113]. The extracted values are similar to the values for FSEG from n-type SiC. The device was destroyed upon cooling below 150K.

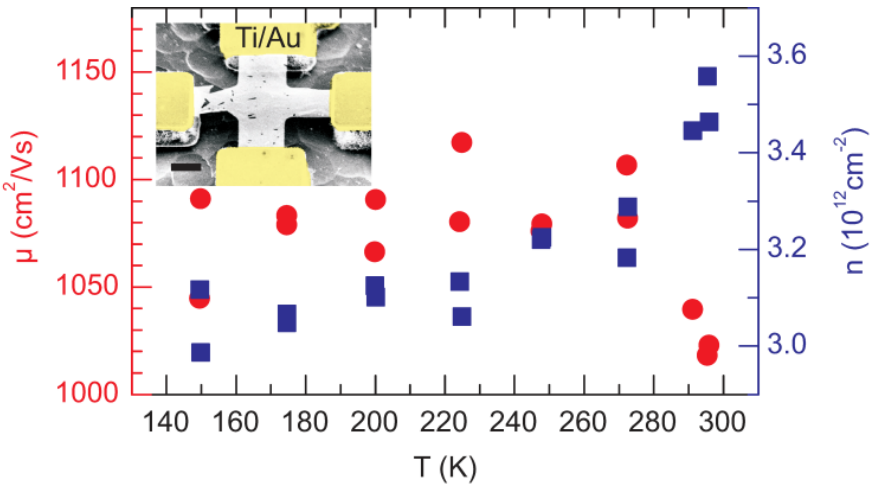

Figure 4.12: Charge carrier concentration (blue rectangles) and mobility (red circles) are derived from Hall effect and conductivity measurements on a FSEG structure from NI-SiC. The transport properties are fairly temperature-independent. The inset shows an SEM micrograph of the examined Hall cross under a tilt angle of 45°. The scale bar corresponds to 2μm.

4.4.4.2 Results on aluminum implanted SiC (AI-SiC)

As mentioned earlier, in case of p-type implanted SiC, no ultraviolet light was required for the etching process. However, much higher voltages (3.5-6.5 V) needed to be applied for the reaction to take place. Raman spectra of FSEG obtained from AI-SiC showed the peaks characteristic of graphene. However, except for a few good devices, a majority of them also showed greater evidence of disorder (Figure 4.13). The broad lineshape near the D and G peaks is strikingly similar to that observed in argon-ion bombarded highly oriented pyrolitic graphite [114], where the relaxed momentum condition for the phonons occurred because of point defects. In the present case, the defects could presumably be a consequence of the higher voltages used during the electrochemical etching process.

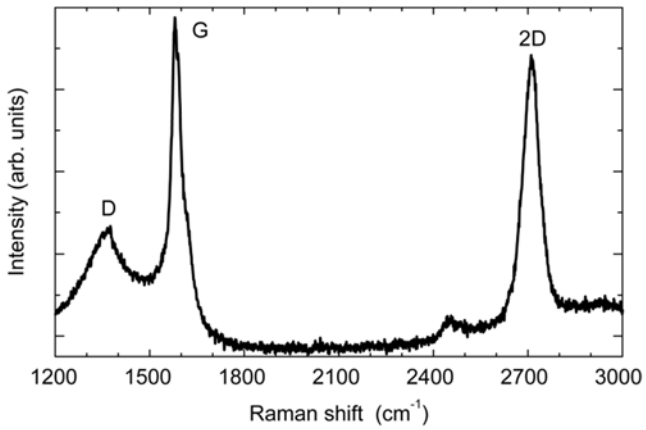

Figure 4.13: Raman spectrum of a FSEG device produced from AI-SiC. The graphene modes are identified. The broad lineshape of the D and G modes are indicative of disorder, presumably caused by the higher voltages used for the p-type electrochemical process.

Similar to the situation on NI-SiC, FSEG devices from AI-SiC tended to rupture due to electrical discharges. In particular, no multi-terminal devices on AI-SiC could be measured, and we focus on the results from two-terminal suspended bridges (cf. inset in Figure 4.14(b)). Figure 4.14(a) shows the magnetoresistivity of a FSEG device for various temperatures. A weak localization peak (WL) is found at low fields (gray area in Figure 4.14(a)). Using equation (1) in Gorbachev et al [91], we extracted the phase coherence length l_ϕ and the elastic scattering lengths l_{iv} for intervalley scattering. Details about how the fit parameters are optimized may be found in my collaborator's thesis [70].

The extracted phase-coherence length $l_\phi \approx 40$nm (at 1.3K) and the intervalley-scattering length $l_{iv} \approx 50$nm for FSEG from AI-SiC are similar to the ones obtained in the multi-terminal FSEG devices from n-type SiC that are discussed in the earlier section ($l_\phi \approx 30$nm at 1.2K and $l_{iv} \approx 25$nm). However, compared to $l_\phi \approx 300$nm at

1.2K and $l_{iv} \approx 100$nm in as-prepared epitaxial graphene or the huge Hall bars discussed in the main text, phase-coherence and intervalley-scattering length are reduced after the PEC etching process. This agrees with the observation of a Raman *D*-peak, which is also related to short-range scattering, in FSEG devices.

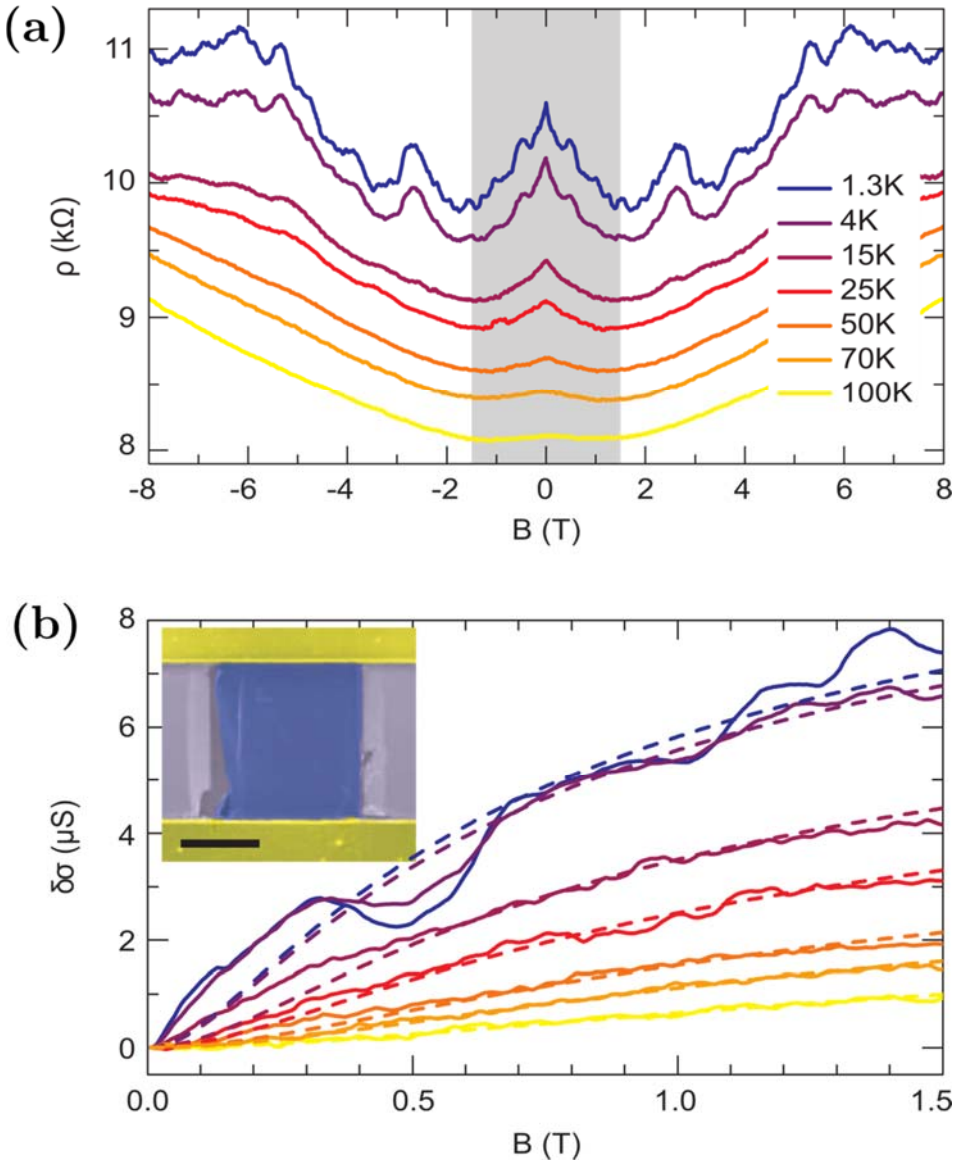

Figure 4.14: (a) Magnetoresistivity of a FSEG sample from AI-SiC. At low fields (gray area), a weak localization peak is observed. (b) The evaluation of the WL correction to the conductivity yields information about phase coherence and elastic

scattering. Therefore, the expected theory [91] (dashed lines) is fitted to the data (solid lines, same color-coding as in (a)). Inset: The SEM micrograph of the two-terminal structure is shown in top view. The scale bar corresponds to 2μm.

4.5 Conclusions

In summary, a combination of Raman spectra and magnetotransport data was used to investigate the properties of FSEG structures. Raman spectroscopy and the evaluation of SdH oscillations give convincing evidence that the free-standing structures behave very similar to AB-stacked bilayer graphene. This leads us to conclude that the buffer layer gets converted to a graphene layer during the PEC etching process. The broken inversion symmetry in the bilayer revealed by the Raman data is a consequence of different charges on the top and bottom layers. In addition, spatial Raman maps and magnetotransport data suggest lateral inhomogeneities in the form of domains with different charge carrier concentrations and mobilities. In contrast to high temperature intercalation techniques, the PEC etching process provides a chemical tool for routine room temperature fabrication of free-standing graphene structures for other scientific explorations. As a comparison, Table 4.1 summarizes the mobilities of PEC etching produced FSEG, QFMLG and QFBLG.

From evaluation of the WL data, one may conclude that the PEC process introduces additional short-range scattering centers in the graphene. Furthermore, the PEC process on a pure buffer layer does not yield a free-standing monolayer. However, it provides an interesting approach to synthesize free-standing graphene nanoribbons.

Table 4.1: Table comparing mobilities of free-standing graphenes (EFSG: Exfoliated free-standing graphene)

Type of graphene	FSEG (this work)	QFMLG [70]	QFBLG [115]	EFSG [10]
Mobility (cm^2/Vs)	2200	3500	1600	230,000

CHAPTER 5

THE EPITAXIAL GRAPHENE-SILICON CARBIDE INTERFACE

This chapter and the following one are devoted to studies of transport barriers in layered materials. The first transport barrier we explore in this chapter is at the interface of EG and SiC. This is an "out-of-plane" transport barrier with respect to the plane of the layered material (graphene in this case). We study the Schottky barrier at the interface of few-layer graphene (FLG) grown epitaxially on n-type 4H-SiC substrates using current-voltage (*I-V*), capacitance-voltage (*C-V*) and photocurrent spectroscopy methods. Parts of this chapter have been adapted from a paper published in Applied Physics Letters [116].

5.1 Introduction

In case of a graphene-semiconductor interface, graphene as a consequence of its zero bandgap, is expected to be analogous to a metal at the contact. Bandstructure of the interface is shown in Figure 5.1. Indeed, a Schottky barrier has been reported at the interface between graphene and various semiconductors including Si [117,118], GaAs [117], SiC [117,119-121], and GaN [122]. Because of the rectifying nature of graphene-semiconductor contacts, they could be useful in metal-semiconductor field effect transistors or high electron mobility transistors. Other possible applications include infrared photodetectors and gas sensing [123].

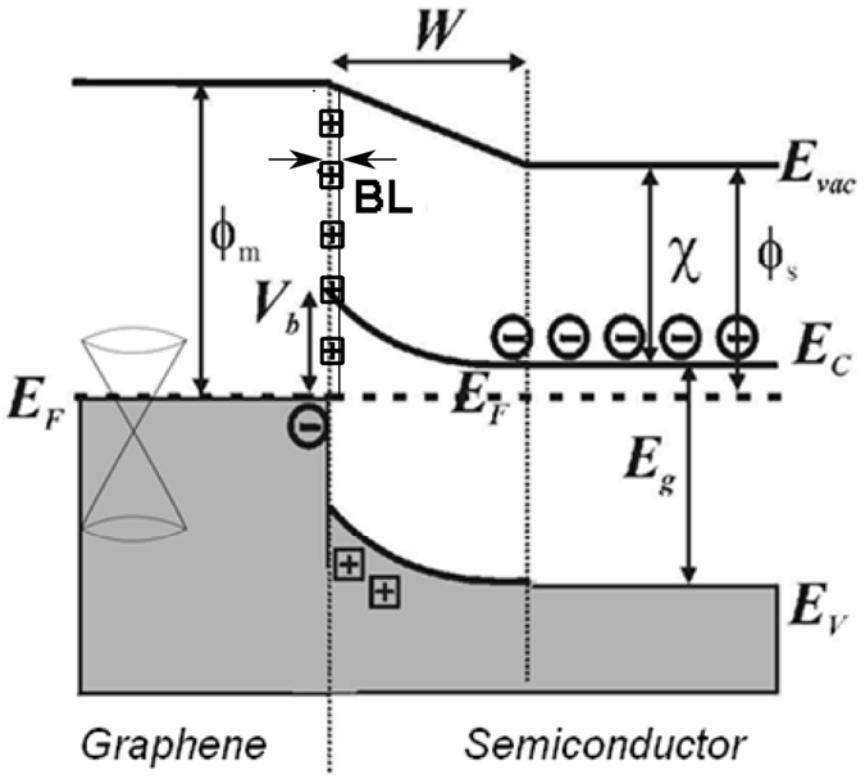

Figure 5.1: Graphene-semiconductor (n-type) interface bandstructure. BL indicates the buffer layer.

5.2 Device fabrication and measurement setup

Si-face of a nitrogen-doped 4° off-axis n^+ 4 H-SiC substrate having a lightly doped n-type epitaxial layer was graphitized by heating at 1400–1500 °C under high vacuum for 1 h. FLG grown on the SiC surface was characterized using a Raman microscope equipped with a 488 nm argon ion laser and spectra were collected in a 180° backscattering geometry. G and 2D peaks corresponding to graphene were seen (Figure 5.2). A small D peak, indicative of defects in the graphene, was also observed. The D/G peak ratio was in the range of 15%–35%. The FLG was patterned using photolithography and oxygen plasma into circular diode structures with varying

diameters from 150–250 μm. 150 nm thick Au was used to contact the FLG. Transfer length method (TLM) structures were also fabricated to measure contact resistance between metal and FLG. 60 nm Ni/100 nm Au was used to make the ohmic back contact to the n^+-SiC substrate. A separate set of control devices with no FLG on the SiC was also fabricated. For these devices, a short 6:1 buffered oxide etch was used to remove any surface oxide. This was followed by evaporation of 150 nm Au to form the diodes.

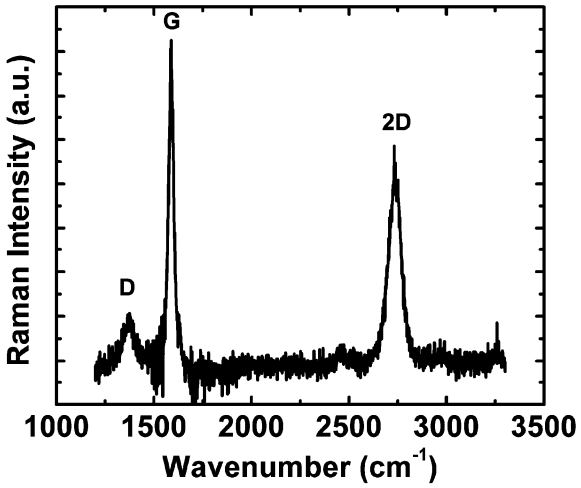

Figure 5.2: Raman spectrum of FLG on SiC. G, 2D and D peaks are identified.

Electrical measurements were performed using a Desert Cryogenics probe station and an Agilent 4156C Semiconductor Parameter Analyzer. Capacitance measurements were performed using an Agilent 4284A Precision LCR Meter in the frequency range 500 Hz to 1 MHz. Photocurrent experiments were conducted using a supercontinuum source (Fianium SC400-4, total power 4 W, 40 MHz) in the energy range 0.75–1.60 eV. Figure 5.3 shows a schematic of the setup. The supercontinuum light was passed through a double-pass monochromator to produce a source with

linewidth 40 nm. A calibrated glass coverslip served as a beam splitter, enabling simultaneous measurement of the short circuit photocurrent at the sample and the incident photon intensity. Optical power was measured using a Si or InGaAs power/wave head. Removal of the gold top contact from portions of the Schottky device enabled light to be incident from the FLG-side of the sample. Photocurrent was measured using lock-in detection at 41 Hz.

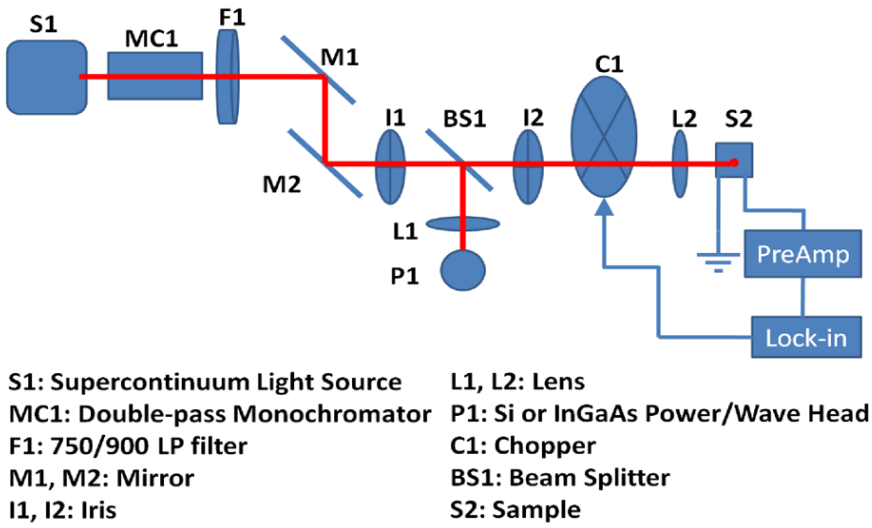

Figure 5.3: Setup of the photocurrent spectroscopy experiment. Path of the light beam is shown in red. Light is incident on the junction from the FLG side.

5.3 Results and discussion

5.3.1 *I-V* and *C-V* measurements

Figure 5.4(a) shows I-V characteristics of a TLM device with 2 μm separation between the pads over a temperature range 4.2 K–298 K. The curves are linear with little change in slope, suggesting that the transport is primarily occurring through the pathway Au/FLG/Au. Thus, we conclude that the Au/FLG interface is non-rectifying. Figure 5.4(b) displays a typical plot of resistance vs pad spacing for Au/FLG devices

at 4.2 K. A sheet resistance $R_s = 1.1\ k\Omega/\square$ and a contact resistance $R_c = 11\ \Omega$ were extracted from the plot for $200 \times 200\ \mu m^2$ contact pads.

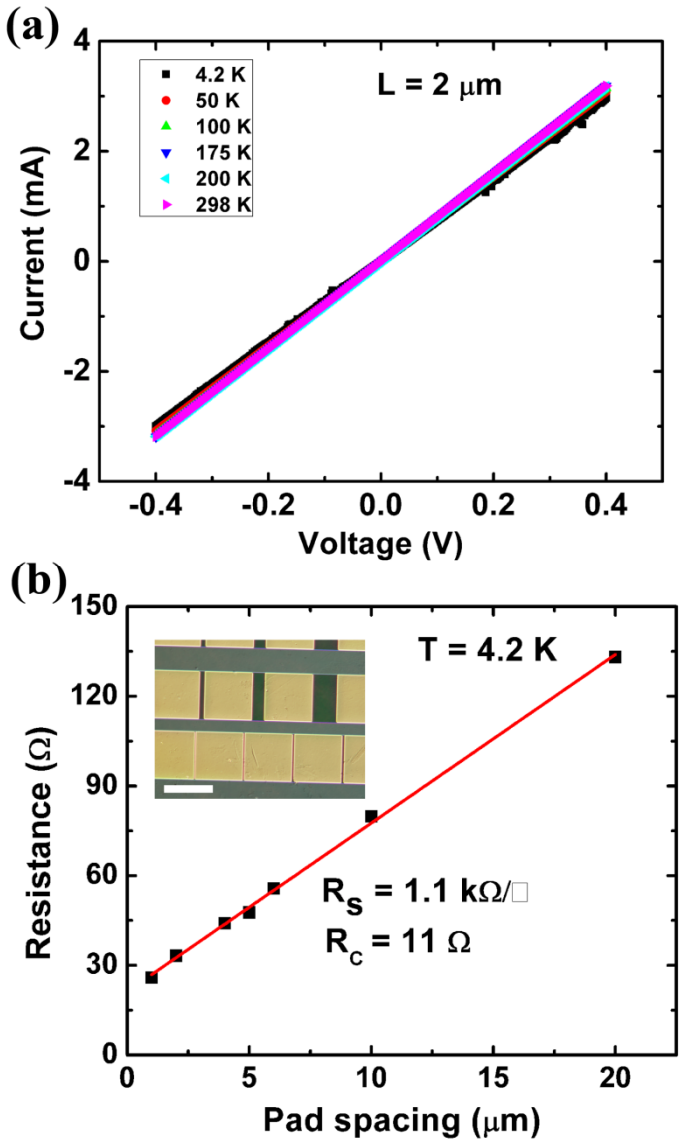

Figure 5.4: (a) *I-V* characteristics of a 2 μm Au/FLG/Au TLM structure over the temperature range 4.2 K–298 K. (b) TLM plot of resistance as a function of pad spacing at 4.2 K. Linear fit is shown using solid line. Inset shows microscope image of the TLM structure. The darker regions, where graphene is present, are still covered with photoresist. Scale bar is 200 μm.

I-V measurements of Au/FLG/SiC devices exhibit rectifying behavior. Forward *I-V* characteristics for a typical device (150 μm diameter) are shown in Figure 5.5(a) over the temperature range 250 K–375 K. Measurements at lower temperatures were unreliable because of freeze-out effects in the SiC [124]. Since the Au/FLG interface is Ohmic, the rectification must arise from the FLG/SiC interface. It is possible, however, the graphene work function could be modified by gold if the graphene is very thin. Figure 5.5(b) is a plot of the diode capacitance as a function of reverse bias voltage at 1 MHz and 298 K. Similar measurements were performed on Au/SiC control samples with no graphene at the interface.

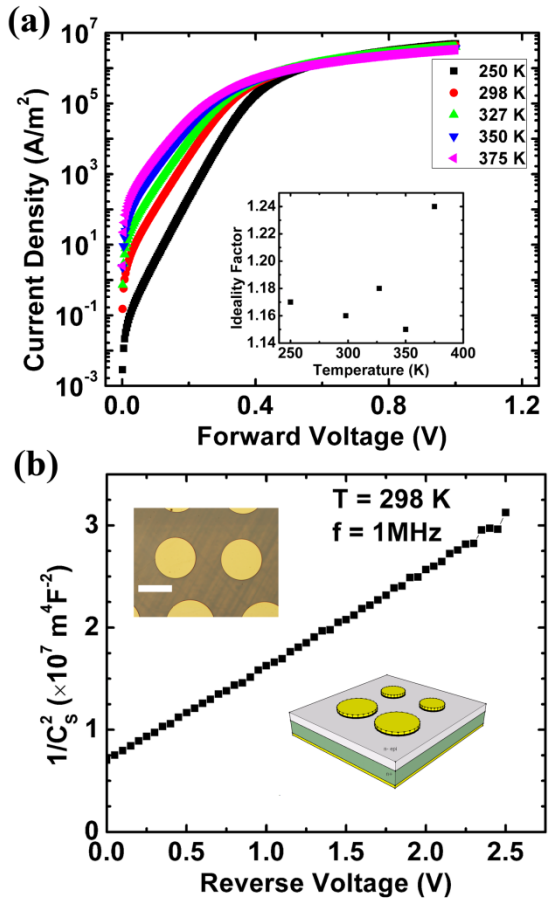

Figure 5.5: (a) Forward *J-V* characteristics of a 150 μm diameter FLG/SiC diode over the temperature range 250 K–375 K. Inset shows ideality factor vs temperature. (b)

Plot of the diode capacitance per unit area as a function of reverse bias voltage at 1 MHz and 298 K. Insets show an optical microscope image and a schematic figure of the diodes. Scale bar is 200 μm.

According to the thermionic emission model, the current, *I*, for a voltage drop, $V \gg \frac{k_B T}{q}$, across the diode at temperature *T* may be expressed as [125]

$$\mathrm{I} = I_0 e^{\frac{qV}{nk_B T}}$$

The pre-factor $\mathrm{I}_0 = SA^{**}T^2 e^{-\frac{q\phi_{E0}}{k_B T}}$ is the saturation current, where *S* is the area of the diode, A^{**} is the modified Richardson constant of the semiconductor, ϕ_{E0} is the effective barrier height at zero bias and *n* is the ideality factor. From the linear portion of the *I-V* characteristics at large forward bias, we obtain an estimate for the series resistance in our devices to lie between 6 – 11 Ω over the entire temperature range. In subsequent analysis, we only consider the portion of the forward bias with $V_A < 0.3$, where the effect of series resistance can be neglected. Using the known values of the diode area *S* and the theoretical value of 4H-SiC Richardson constant A^{**} = 146 $\mathrm{Acm^{-2}K^{-2}}$ [126], the barrier height ϕ_{E0} may be obtained from *I-V* data.

The capacitance per unit area, C_S, of a Schottky diode under reverse bias *V* is given by the depletion capacitance [125]

$$C_S = \left(\frac{q\epsilon_s N_D}{2}\right)^{\frac{1}{2}} \left(V + \frac{\phi_{BC} - \xi - k_B T}{q}\right)^{-\frac{1}{2}}$$

where $\epsilon_s$is the permittivity of the semiconductor (for 4H-SiC, $\epsilon_s = 9.87\epsilon_0$), N_D is the doping density, ϕ_{BC} is the barrier height and ξ is the distance of the Fermi level

below the conduction band in the charge-neutral semiconductor at equilibrium. From a plot $1/C^2$ vs V, one can deduce the barrier height ϕ_{BC} and the doping in the semiconductor. The results of analyses for 12 FLG/SiC and 3 Au/SiC devices at 298 K are presented in Table 5.1. The doping density of the n-SiC layer from the slope of the $1/C_S^2 - V$ plot is $(1.9 \pm 0.1) \times 10^{16} cm^{-3}$, which agrees well with the specified doping $2 \times 10^{16} cm^{-3}$.

Table 5.1: Table showing average parameters for 12 FLG/SiC and 3 Au/SiC devices at 298 K. *C-V* measurements were performed at 1 MHz.

Device	**n**	ϕ_{E0}**(eV)**	ϕ_{BC}**(eV)**
FLG/SiC	1.15±0.04	0.67±0.06	1.06±0.12
Au/SiC	1.07±0.01	1.58±0.07	1.68±0.06

Table 5.1 shows that Au/SiC diodes have low ideality factors. In addition, the barrier heights from *I-V* and *C-V* measurements are comparable. As an example from literature, barrier heights measured on Au/4H-SiC diodes using *I-V* and *C-V* methods were reported to be 1.73 and 1.80 eV respectively [126]. The small discrepancy between $\phi_{E0}$and ϕ_{BC} can be explained as a consequence of the $n > 1$ ideality factor which leads to a difference between the flat-band barrier height measured by the *C-V* method and the zero-bias barrier height measured by the *I-V* method. The barrier heights satisfy the relationship $\phi_{BC} = n\phi_{E0} - (n-1)\left(\xi + \frac{k_B T}{q}\right)$ which was derived in [127] for non-ideal Schottky contacts.

FLG/SiC diodes exhibit a slightly larger ideality factor, but are comparable to reports in literature [119]. However, a much bigger discrepancy between ϕ_{E0} and ϕ_{BC} exists. Unlike above, this cannot be explained as a consequence of non-ideality. The difference was found to persist over the entire temperature range. Such differences have been reported before in previous works examining the FLG/SiC interface [117,119] but have not been studied. In the rest of the chapter, we investigate the reasons for this discrepancy.

5.3.2 Discussion of models to explore discrepancy between *I-V* and *C-V* data

Various models were explored in order to explain the observations. The *C-V* data show little dispersion in the frequency range 500 Hz–1 MHz. This rules out effects due to deep traps in the SiC. Because of the wide bandgap of 4H-SiC viz. 3.23 eV and low doping of the epitaxial layer, we do not expect to have significant contributions from image force lowering, recombination in the depletion region, and field/thermionic-field emission effects [125]. This leaves three possibilities to be considered: (i) presence of an interfacial layer with interface states, (ii) sheet resistance of graphene, and (iii) barrier inhomogeneities. Though it is likely that interface states are the reason for n>1 in the forward bias, interfacial layer models [128] were inadequate to explain the large difference between *I-V* and *C-V* barrier heights. Sheet resistance of the FLG could also lead to over-estimation of the barrier height from *C-V* measurements [129]. However, the measured sheet resistance of FLG was not high enough to account for the discrepancy.

This leads us to consider the possibility of a laterally inhomogeneous barrier. A Gaussian distribution of barrier heights has been proposed on other Schottky barrier systems to explain differences in the barrier heights from current and capacitance measurements (see e.g. [130] and references therein). Two of the earliest works which develop an analytical theory for electron transport by thermionic emission in case of a Gaussian distribution of barrier heights are by Werner and Gűttler [131] and Tung [132]. According to the model, the Schottky barrier is composed of patches with a distribution of barrier heights over a length scale smaller than, or comparable to, the depletion region width. The expression for current through such a junction for $V \gg \frac{k_B T}{q}$ takes the form:

$$I = SA^{**}T^2 e^{-\frac{q\phi_E}{k_B T}} e^{\frac{qV}{nk_B T}}$$

All symbols have the same meanings as before. ϕ_E is the effective barrier height extracted from *I-V* measurements. The *C-V* technique, on the other hand, measures the mean barrier height ϕ_{Bm} of the inhomogeneous junction. The relationship between the two is given by:

$$\phi_E = \phi_{Bm} - \frac{q\sigma^2}{2k_B T}$$

where σ is the standard deviation of the Gaussian distribution. Assuming that σ is temperature-independent, the above equation suggests that a plot of the difference between the barrier heights measured by *C-V* and *I-V* techniques vs *1/T* should yield an estimate for the spread of the distribution [131,133]. Such a plot is shown in Figure 5.6(a), from which we compute $\sigma = 137 \pm 11$ meV. A previous work [121] studying the FLG/SiC interface over sub-micron dimensions using a scanning current probe

method found a similar Gaussian distribution of barrier heights, with the spread being 100 meV. This lends support to our explanation based on lateral barrier inhomogeneities.

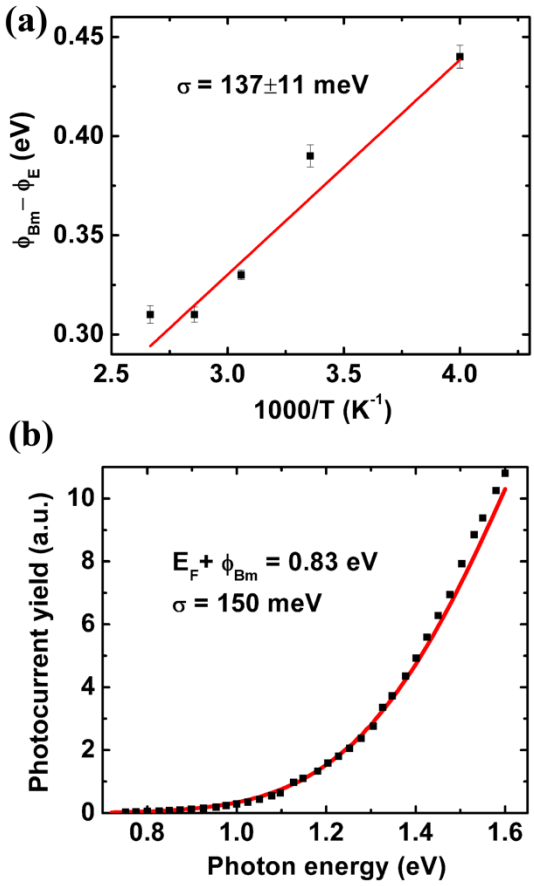

Figure 5.6: (a) Plot of the difference between the *C-V* and *I-V* barrier heights as a function of *1/T*. Linear fit is shown by solid line. (b) Photocurrent yield plotted as a function of photon energy at 298 K. Shown with solid line is a fit using a model which explains the observed photocurrent as an internal photoemission process from FLG to SiC across an inhomogeneous barrier with a Gaussian distribution of barrier heights. Parameters from the fit are shown.

5.3.3 Photocurrent spectroscopy

Further evidence for barrier inhomogeneites is presented by photocurrent measurements. Figure 5.6(b) shows a plot of the photocurrent yield at the FLG/SiC

interface vs incident photon energy. The data is modeled assuming an internal photoemission process from graphene into the SiC. Details of the model are explained next.

5.3.3.1 Photoemission model at graphene-semiconductor junction assuming an atomically rough interface and a unique barrier height

First we develop a basic model assuming a unique barrier height at the interface. Figure 5.7 shows a graphene-semiconductor junction irradiated with light of energy $\hbar\omega$. The electrons in graphene absorb photons and are excited over the barrier ϕ_B into the semiconductor. Our goal is to develop a first-order model for this photoemission, considering only interband transitions in graphene. For a photon of energy $\hbar\omega$, the rate of net stimulated absorption in graphene per unit area may be written as

$$N = \frac{\pi\hbar e^2 v_F^2}{2\epsilon_0 c}\frac{I}{(\hbar\omega)^2} \times 4 \times \int_{FBZ} \frac{d^2\vec{k}}{(2\pi)^2}\left[f_v(\vec{k}) - f_c(\vec{k})\right]\delta\left[E_c(\vec{k}) - E_v(\vec{k}) - \hbar\omega\right]$$

where v_F is the Fermi velocity in graphene, I is the power of incident light per unit area and the factor of 4 accounts for the spin and valley degeneracies in graphene. f_v and f_c are the Fermi functions in the valence and conduction bands of graphene given by $f_v(\vec{k}) = \left[1 + e^{\frac{E_v(\vec{k}) - E_F}{k_B T}}\right]^{-1}$ and $f_c(\vec{k}) = \left[1 + e^{\frac{E_c(\vec{k}) - E_F}{k_B T}}\right]^{-1}$ where E_F is the Fermi level energy. The energy band structure of graphene at low energies may be approximated by a linear dispersion:

$$E_c(k) = \hbar v_F k$$

$$E_v(k) = -\hbar v_F k$$

$$\Rightarrow N = \frac{e^2}{4\epsilon_0 c\hbar}\frac{I}{\hbar\omega}\frac{e^{-\frac{E_F}{k_BT}}\left[e^{\frac{\hbar\omega}{2k_BT}} - e^{-\frac{\hbar\omega}{2k_BT}}\right]}{1 + e^{-\frac{2E_F}{k_BT}} + e^{-\frac{E_F}{k_BT}}\left[e^{\frac{\hbar\omega}{2k_BT}} - e^{-\frac{\hbar\omega}{2k_BT}}\right]}$$

In the limit $\left(\frac{\hbar\omega}{2} - E_F\right) \gg k_BT$,

$$N = \frac{e^2}{4\epsilon_0 c\hbar}\frac{I}{\hbar\omega}$$

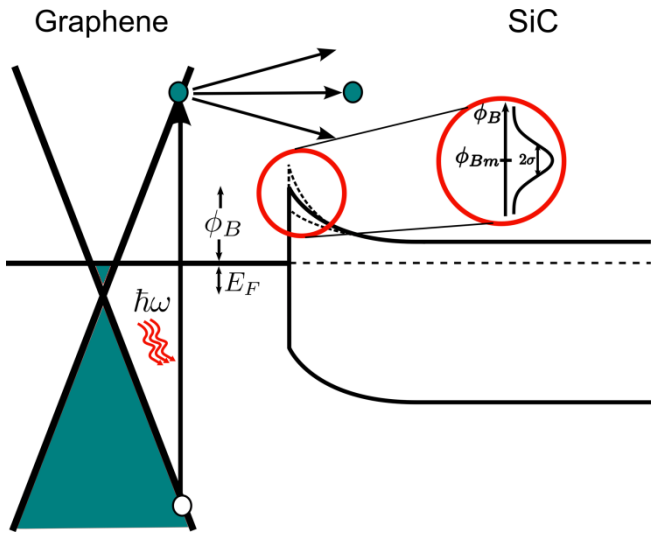

Figure 5.7: Energy band diagram depicting the photoemission process from graphene into SiC across an inhomogeneous barrier with a Gaussian distribution of barrier heights having a mean barrier height ϕ_{Bm} and standard deviation σ.

We assume that the FLG/SiC interface is atomically rough and as a result, the photoexcited electrons are provided transverse momentum perpendicular to the interface. As a consequence, roughly half the excited electrons are emitted into the SiC following a Lambertian distribution. Injected current into SiC may be written as

$$J = \Theta\left[\frac{\hbar\omega}{2} - (\phi_B + E_F)\right]\int_0^{2\pi}\int_0^{\frac{\pi}{2}}\frac{qN\cos^2\theta}{2\pi}\sin\theta d\theta d\phi$$

where $\Theta(x)$ is the Heaviside function which accounts for no emission when the excited electron energy is less than the barrier height ϕ_B.

$$\therefore J = \frac{qN}{3}\,\Theta\left[\frac{\hbar\omega}{2} - (\phi_B + E_F)\right]$$

The photocurrent yield is given by

$$Y = \frac{J}{\left(I/\hbar\omega\right)} = \frac{q^3}{12\epsilon_0 c\hbar}\,\Theta[\hbar\omega - 2(\phi_B + E_F)]$$

This expression does not provide a good fit to the data.

5.3.3.2 Photoemission model at graphene-semiconductor junction assuming an atomically rough interface and a Gaussian distribution of barrier heights

Instead of a single unique barrier height, let us consider a situation where the barrier heights have a Gaussian distribution with mean barrier height ϕ_{Bm} and spread σ. The probability of having a barrier height ϕ_B may be expressed by the function

$$P(\phi_B; \phi_{Bm}, \sigma) = \frac{1}{\sqrt{2\pi\sigma^2}} e^{-\frac{(\phi_B - \phi_{Bm})^2}{2\sigma^2}}$$

Then, the expression for photocurrent yield is given by

$$Y = \frac{J}{\left(I/\hbar\omega\right)} = \int_0^\infty \frac{d\phi_B}{\sqrt{2\pi\sigma^2}} e^{-\frac{(\phi_B - \phi_{Bm})^2}{2\sigma^2}} \times \frac{q^3}{12\epsilon_0 c\hbar}\,\Theta[\hbar\omega - 2(\phi_B + E_F)]$$

$$\therefore Y = \frac{q^3}{12\epsilon_0 c\hbar}\frac{1}{\sqrt{2\pi\sigma^2}}\int_0^\infty d\phi_B e^{-\frac{(\phi_B - \phi_{Bm})^2}{2\sigma^2}}$$

Using this expression, we obtain a fit to the experimental data in Figure 5.6(b).

The fit parameters are E_F, ϕ_{Bm} and σ. It can be seen from the form of the Gaussian distribution function that the majority of injected electrons will have energy

$E_F + \phi_{Bm}$. So, it is not possible to uniquely extract E_F and ϕ_{Bm}. The parameter $E_F + \phi_{Bm}$, however, can be uniquely obtained and is found to be 0.83 eV. We would like to make a note here that the exact nature of the bandstructure of FLG is not important in the energy range in which the measurements have been performed, as the photocurrent in this regime is primarily determined by the Gaussian distribution of the barrier heights. In addition, the value for σ from the fit is $150\, meV$, which agrees satisfactorily with the earlier estimate from electrical measurements. For the mean barrier height ϕ_{Bm} from photocurrent and *C-V* measurements to agree, the Fermi level should lie 0.24 ±0.12 eV below the Dirac point. This suggests an average p-doping of the graphene layer, which has been observed in experiments conducted by other groups [134-136].

Finally, we speculate on the origin of the inhomogeneous barrier at the FLG/SiC interface. It is known that the local barrier at a metal-semiconductor interface is highly dependent on the interfacial structure. Possible reasons for variation in the barrier height include dislocations, grain boundaries and structure-dependent interface dipoles [131,137]. Recently, TEM studies have shown that graphene grown over terrace step edges on the SiC contain a high density of structural defects [138]. The substrates used in this study had a 4^o miscut with respect to the *c*-axis. Thus, we expect a lot of step edges in our devices, the dimensions of which are of the order of several hundred microns. STM studies have also shown existence of hexagon-pentagon-heptagon defects in the interface layer [139]. Such defects could contribute to the observed inhomogeneity. In addition, doping domains in graphene [140,141] could shift the Fermi level and cause variations in the Schottky barrier height.

It has also been shown recently [142] using electron microscopy that the buffer layer on the $(11\bar{2}n)$ facets of off-axis SiC delaminates from the surface conferring it a quasi-free-standing nature. This could be another potential explanation for the observed variation, where the terraces and step-edge facets contribute to different Schottky barrier heights. A caveat for interpretation in this framework for the work presented here is that the buffer layer model is well-understood for graphene grown under argon backpressure, whereas the graphene used for this work was grown under high vacuum conditions, where the nature of the interface might be different. The microscopic nature of the origin of the inhomogeneities requires additional study and is beyond the scope of this work.

5.4 Conclusions

In summary, the Schottky barrier at the interface of FLG/SiC was studied using a combination of electrical and photocurrent measurements. The results can be explained as a consequence of barrier inhomogeneities at the FLG/SiC interface, which may be a consequence of structural imperfections or doping domains. In order to be useful for applications, it is necessary to be able to control the barrier height precisely. Possible ways to achieve such improvement might involve making devices on a single terrace without crossing a terrace step edge or investigating growth conditions which can lead to formation of FLG with minimum compressive stress and defects [139].

CHAPTER 6

TRANSPORT BARRIER AT THE INTERFACE OF DIFFERENT NUMBER OF LAYERS OF MOLYBDENUM DISULFIDE

6.1 Introduction

In this chapter, we discuss a new layered material, molybdenum disulfide (MoS_2). As introduced in Chapter 1, MoS_2 belongs to a class of materials called layered transition metal dichalcogenides (LTMDs). Unlike graphene, the dichalcogenides of Mo and W have a bandgap in the range of 1.1-1.9 eV [143]. This can enable high-performance flexible digital electronics based on LTMDs. Additionally, density functional theory based calculations have shown that the bandstructure of the layered TMDs is affected by quantum confinement and is a function of the number of layers [144]. For example, the evolution of the electronic bandstructure from bulk to monolayer in MoS_2 is shown in Figure 6.1. It can be observed that monolayer MoS_2 is a direct bandgap semiconductor with a bandgap of ~ 1.9 eV. In fact, this observation is true for other LTMDs – they have a direct bandgap in the monolayer state [144-149]. This has useful implications for optoelectronic devices.

In this short chapter, we present results on exploring transport at the interface of different layers of MoS_2 obtained naturally during mechanical exfoliation. Based on the evolution of the electronic bandstructure with different number of layers in LTMDs, we can envision semiconductor heterostructures based on layer number control. Figure 6.2 illustrates the general idea. In contrast to the "out-of-plane" barrier discussed in the previous chapter, these may be thought of as "in-plane" barriers.

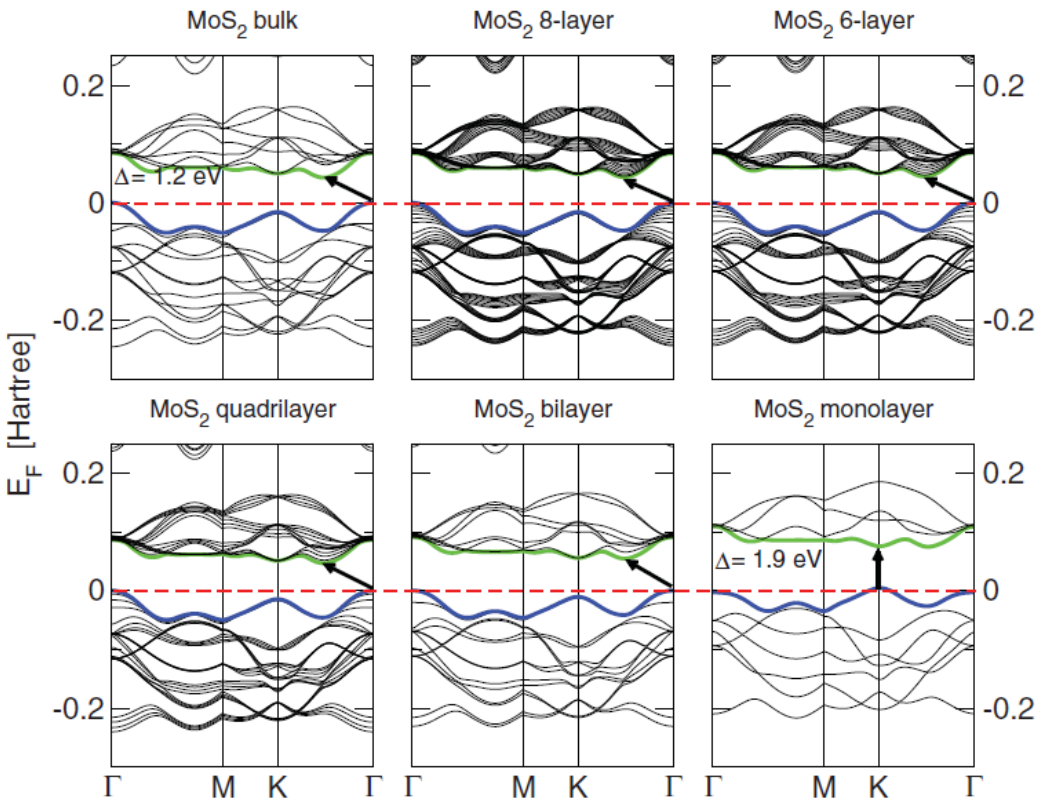

Figure 6.1: Density functional theory (DFT) based calculations showing evolution of MoS_2 bandstructure from bulk to monolayer. Dotted red line indicates position of Fermi level. It is observed that monolayer MoS_2 is predicted to be a direct bandgap semiconductor. Adapted from [144].

The chapter is outlined as follows. First, we describe fabrication techniques employed to obtain the MoS_2 junction devices. Then, the main transport results are presented.

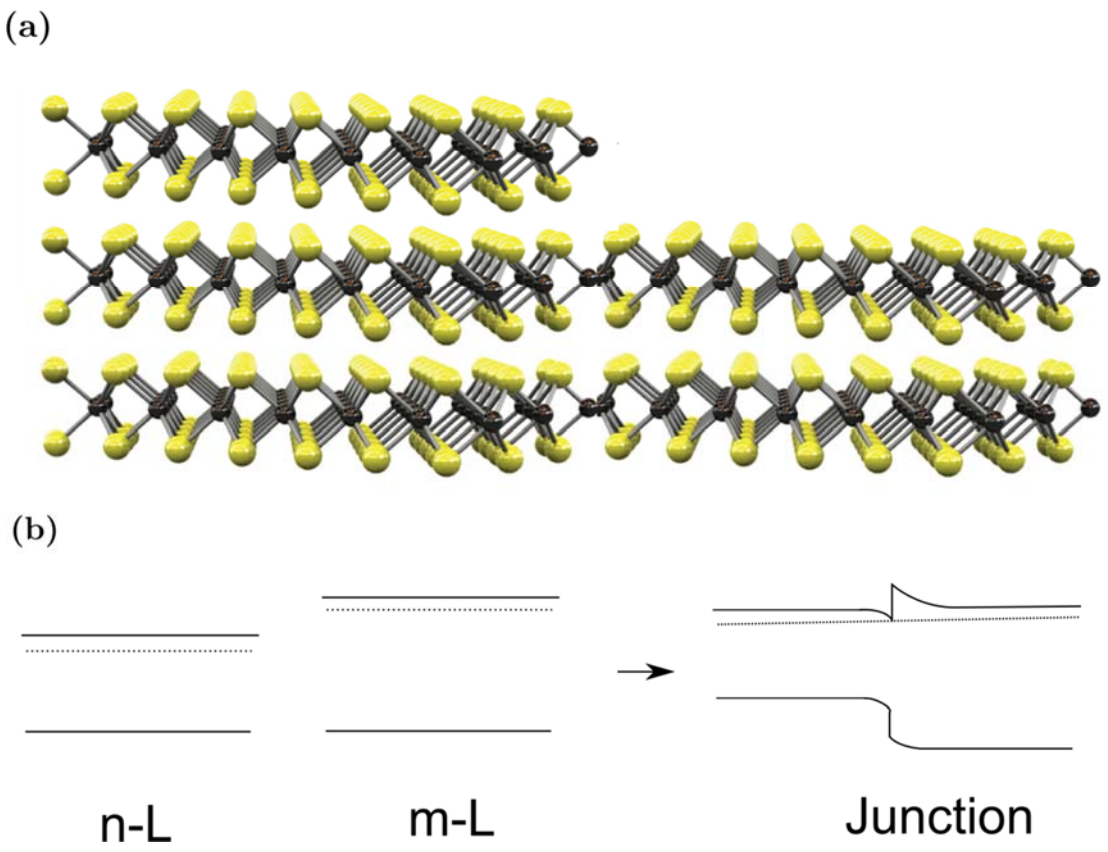

Figure 6.2: (a) Schematic showing a junction between a 3L and 2L MoS_2 device. (b) Example of a semiconductor heterojunction at the interface between n-layers and m-layers of a layered material.

6.2 Fabrication of MoS_2 junction devices

6.2.1 Identification and characterization of MoS_2 flakes

Bulk MoS_2 crystal obtained from SPI Supplies, Inc. was pressed on to adhesive tape obtained from Ultron Systems, Inc. and peeled off. The MoS_2 flakes stuck on the tape were thinned down by repeated peeling on fresh tape sections. After sufficient number of iterations, a piece of tape covered with thin flakes of MoS_2 was pressed down on a $\sim 1.5\ cm \times 1.5\ cm$ Si die with 285 nm of thermally grown oxide. The n-type Si (100) wafer was degenerately doped (resistivity < 0.005 $\Omega - cm$). Before exfoliation on the Si die, a grid was patterned on to the Si die in order to enable locating the exfoliated

flakes on the chip. It consisted of $5\ \mu m \times 5\ \mu m$ squares labeled with letters/numbers separated by $300\ \mu m$ interspersed with smaller $1\ \mu m \times 1\ \mu m$ squares separated by $20\ \mu m$. The grid was patterned using image-reversal photolithography and Cr/Au (3 nm/65 nm) evaporation followed by overnight lift-off in Microposit Stripper 1165.

After exfoliation, the next step is identification of the flakes under an optical microscope. Typically, the chip is scanned using a $50\times$ objective, whose field of view is $\sim 300\ \mu m \times 300\ \mu m$. Because of the optical path difference between light incident on the $MoS_2/SiO_2/Si$ stack versus the bare wafer, thin MoS_2 flakes exhibit a contrast which corresponds with their thickness [150]. Figure 6.3 shows optical microscope images of thin MoS_2 flakes with different number of layers. For this work, candidate flakes were identified based on existence of a step/junction consisting of different number of MoS_2 layers. The additional criterion is that the two different layer portions be individually larger than $\sim 3\ \mu m$ in atleast one dimension in order to enable fabrication of multi-terminal devices. Figure 6.4 shows an example candidate flake, which consists of a junction between bilayer (2L) and trilayer (3L) of MoS_2.

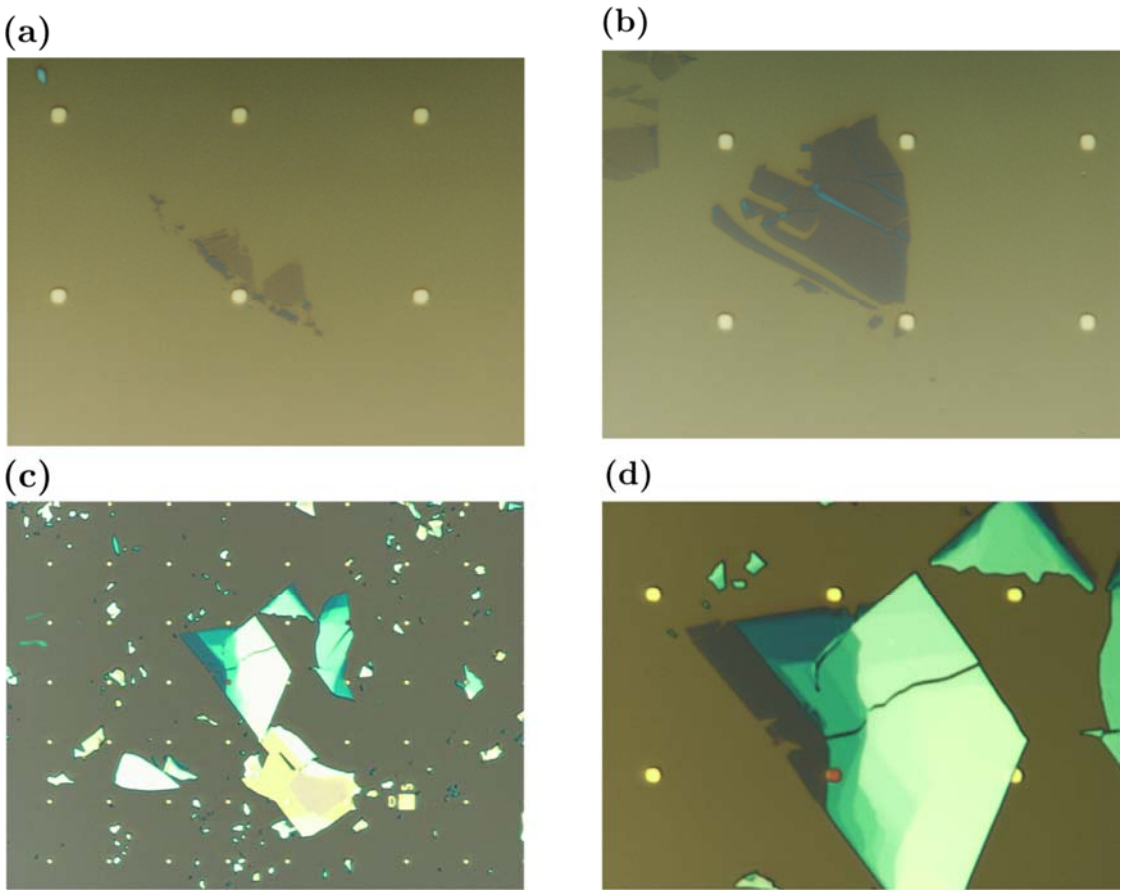

Figure 6.3: Thin MoS_2 (a) Monolayer (b) Bilayer (center), Monolayer (to the left) (c) Zoomed out image of (d) which is a trilayer (left) attached to a thicker MoS_2 region. The small gold squares in the figures are $\sim 1\ \mu m \times\ 1\ \mu m$ and are part of a denser grid spaced apart by $20\ \mu m$ for locating the flakes. In (c), the bigger gold square labeled with D and 5 is part of the sparser grid of $\sim 5\ \mu m \times\ 5\ \mu m$ markers spaced apart by $300\ \mu m$.

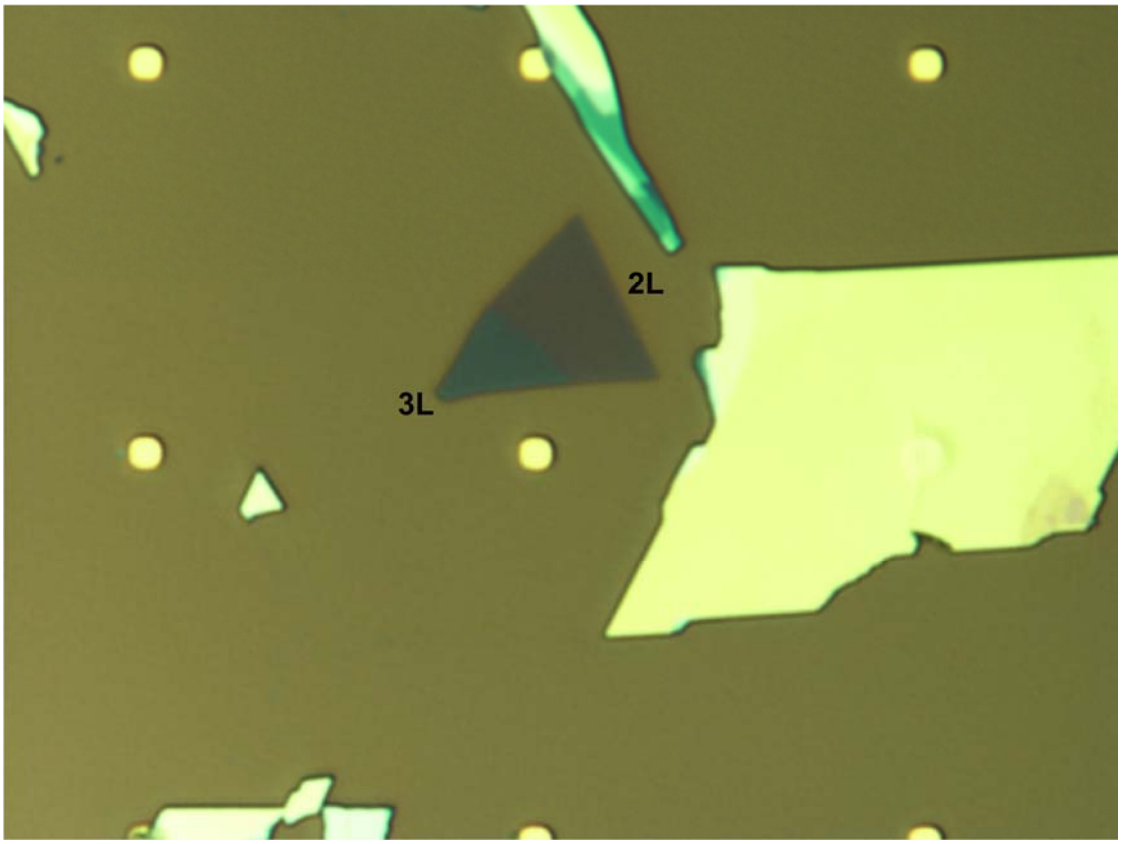

Figure 6.4: Optical microscope image of a 3L – 2L MoS_2 junction. The small squares are $\sim 1\ \mu m$.

After the optical identification process, the next step is to confirm the layer thickness by using Raman spectroscopy and/or photoluminescence. The Raman spectrum of MoS_2 has two prominent peaks at ~ 384 cm^{-1} and ~ 400 cm^{-1} labeled by E^1_{2g} and A_{1g} respectively [151]. The position of these modes depends upon the number of layers for thin flakes. The splitting between the modes is smaller for a monolayer and progressively increases as the thickness increases towards the bulk (Figure 6.5) [151,152]. A second technique which is especially useful in identifying single-layer MoS_2 is photoluminescence. As mentioned earlier, monolayer MoS_2 is a direct bandgap semiconductor and is expected to show highly efficient photoluminescence

[146]. Figure 6.6 shows photoluminescence (PL) spectra obtained using a 488 nm laser. PL from the monolayer (ML) is much more intense compared to that from a bilayer (BL) or thicker MoS_2. Thus, Raman spectroscopy enables identification of layer count and PL further confirms monolayers unambiguously.

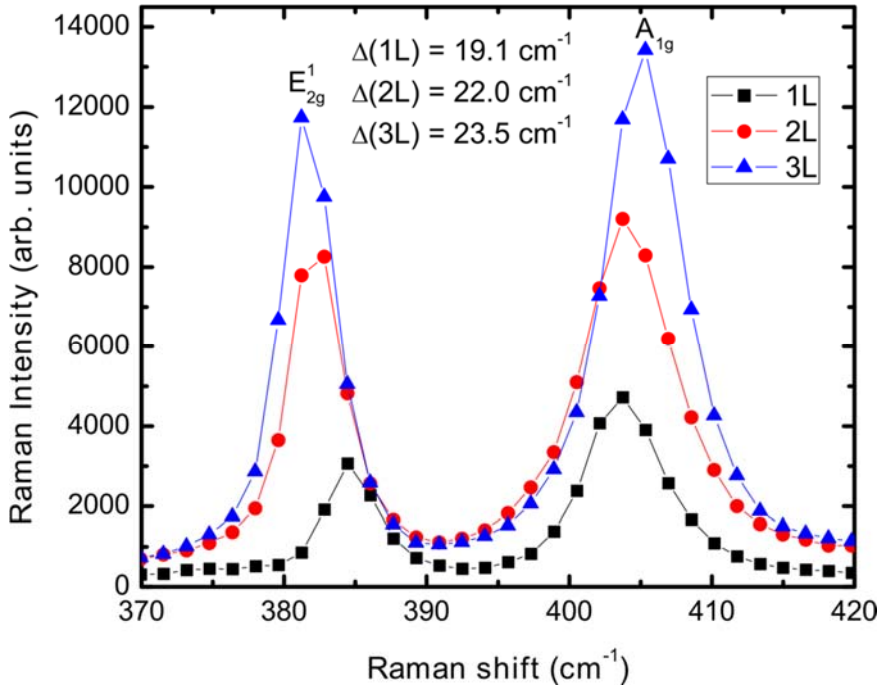

Figure 6.5: Raman spectra of few-layer MoS_2 obtained using 488 nm laser. E^1_{2g} and A_{1g} modes are labeled. The splitting between the modes is a function of layer count and can act as an identifier.

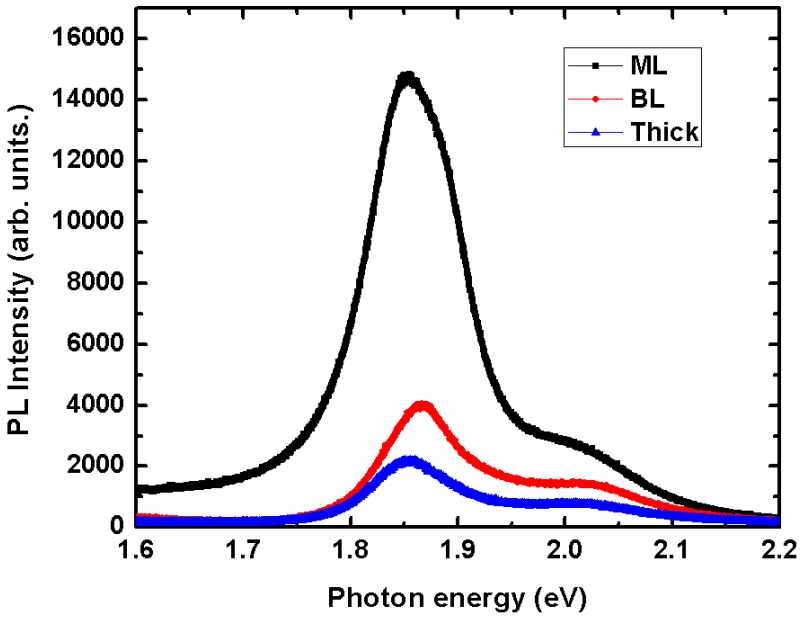

Figure 6.6: Photoluminescence spectra of monolayer (ML), bilayer (BL) and thick MoS_2 obtained using a 488 nm laser. PL intensity of ML MoS_2 is $> 3\times$ that of the bilayer.

Finally, the last step before device fabrication is AFM (Figure 6.7). AFM is performed to further confirm layer thickness and also ensure that the candidate flakes are clean prior to fabrication. As shown in Figure 6.7(d), sometimes unwanted particulates could be present on the surface. Such flakes are avoided in making devices.

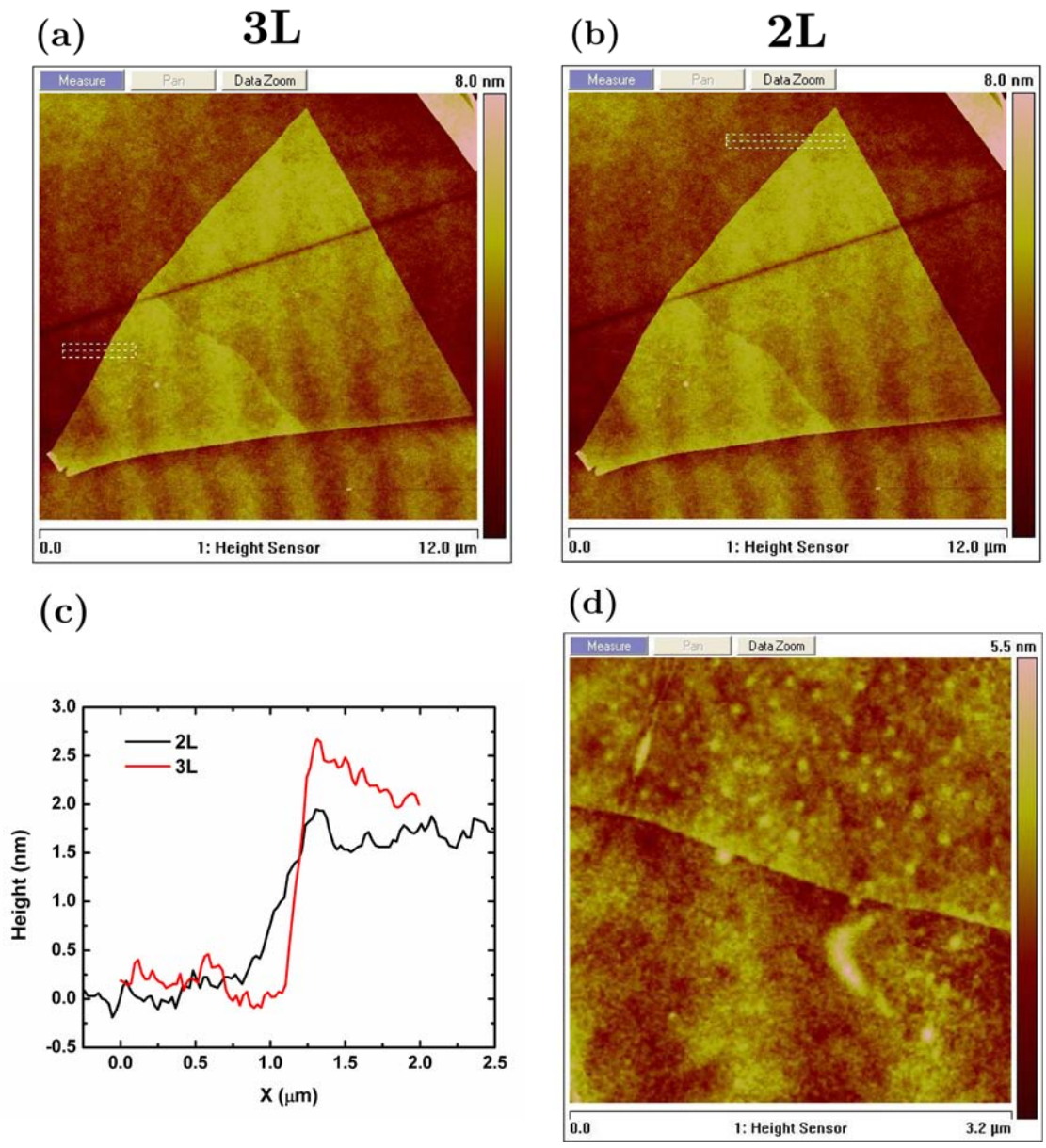

Figure 6.7: AFM scans of MoS_2 flakes. (a) and (b) show regions where line cuts are taken for the profiles in (c). (d) MoS_2 flake where particulates may be observed. Such flakes are avoided.

6.2.2 Nanofabrication steps for the junction device

In this sub-section, we will present fabrication of a junction device comprising 2L and 3L MoS_2. The starting flake is shown in Figure 6.4. Corresponding AFM scan is shown in Figure 6.7(a)/(b). The region of interest in a 150 × image of the flake is then

cut out along with the markers (white regions in Figure 6.8) and imported into the computer-aided drawing software L-Edit on to a blank grid template after appropriate scaling. The cut-out white portions of the image are mapped onto a new layer in L-Edit and aligned with the existing markers on the template grid. This is shown in Figure 6.9. Layers for the various fabrication steps are then drawn on top of this imported image.

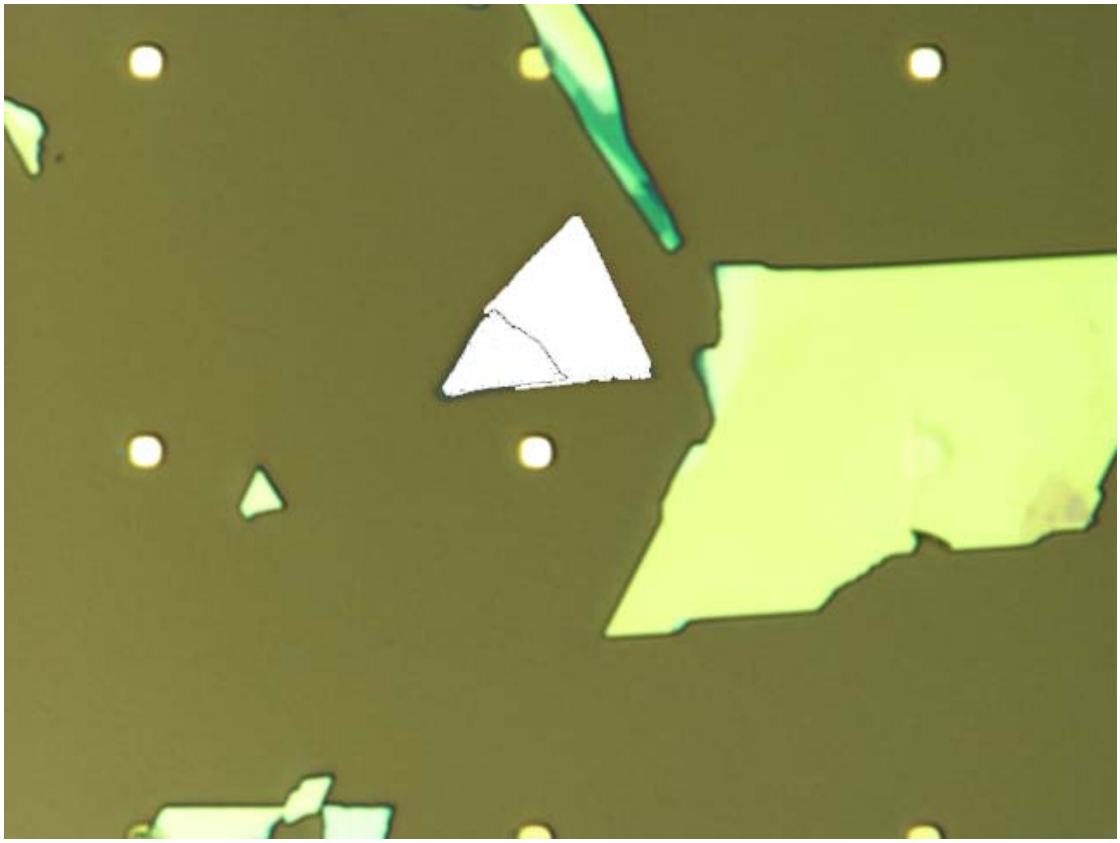

Figure 6.8: Figure showing cut-out regions (white) on a 150 × optical microscope image. Usually, four markers are included along with the cut-out of the flake. Sometimes, it is advantageous to include other neighboring flakes in the cut-out in order to avoid them later during routing of the leads.

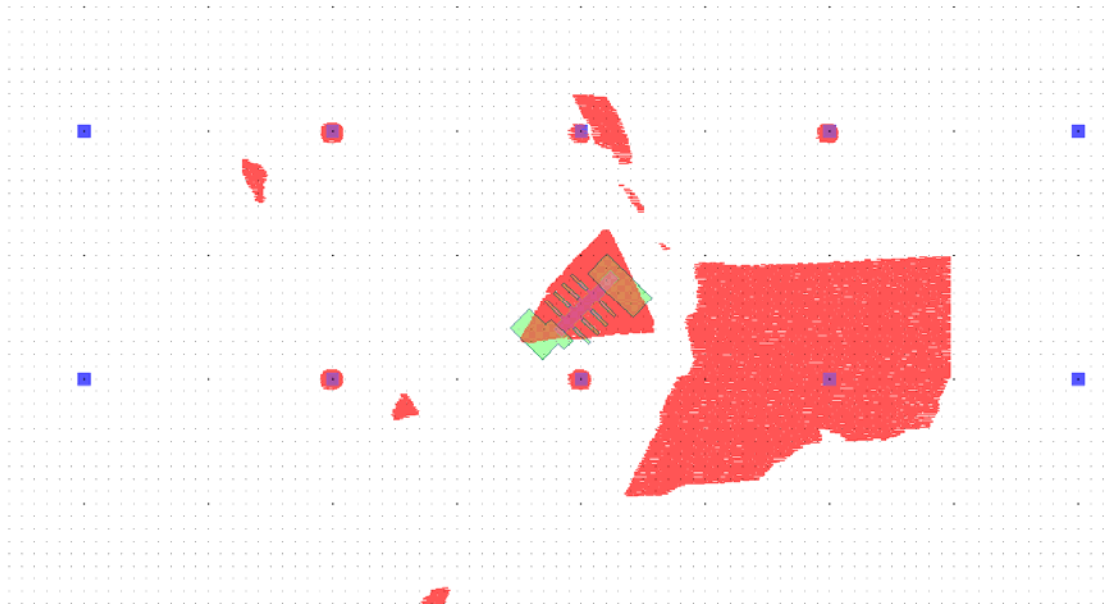

Figure 6.9: Alignment of the flake to the grid - The blue squares are part of the template grid. The imported image of the flake is the red layer. The red squares on the imported image are aligned with the squares on the template grid. Subsequently, the layers for lithography are drawn.

Two or three steps of lithography are needed for making the device. Devices are fabricated using the Nabity SEM-based e-beam lithography tool. A set of four $5\ \mu m \times 5\ \mu m$ markers are identified around the flake of interest and are used as alignment markers. Additional alignment markers may be written during subsequent lithography steps, as required.

The first step is defining short leads to the device. Sometimes, the longer leads and pads could be defined in the same step, if the area around the flake of interest is clean of other potentially interfering flakes and tape residues. Otherwise, the patterning of the MoS_2 flake is performed first using a SF_6/Ar plasma (100 W, 100 mtorr, 40 sccm SF_6, 10 sccm Ar). During the plasma etch, the other interfering flakes and residues are also cleaned up. Subsequently, the longer leads and pads are defined.

These steps are indicated in Figure 6.10 (a)-(c). Figure 6.10(d) shows a zoomed-in picture of the finished device.

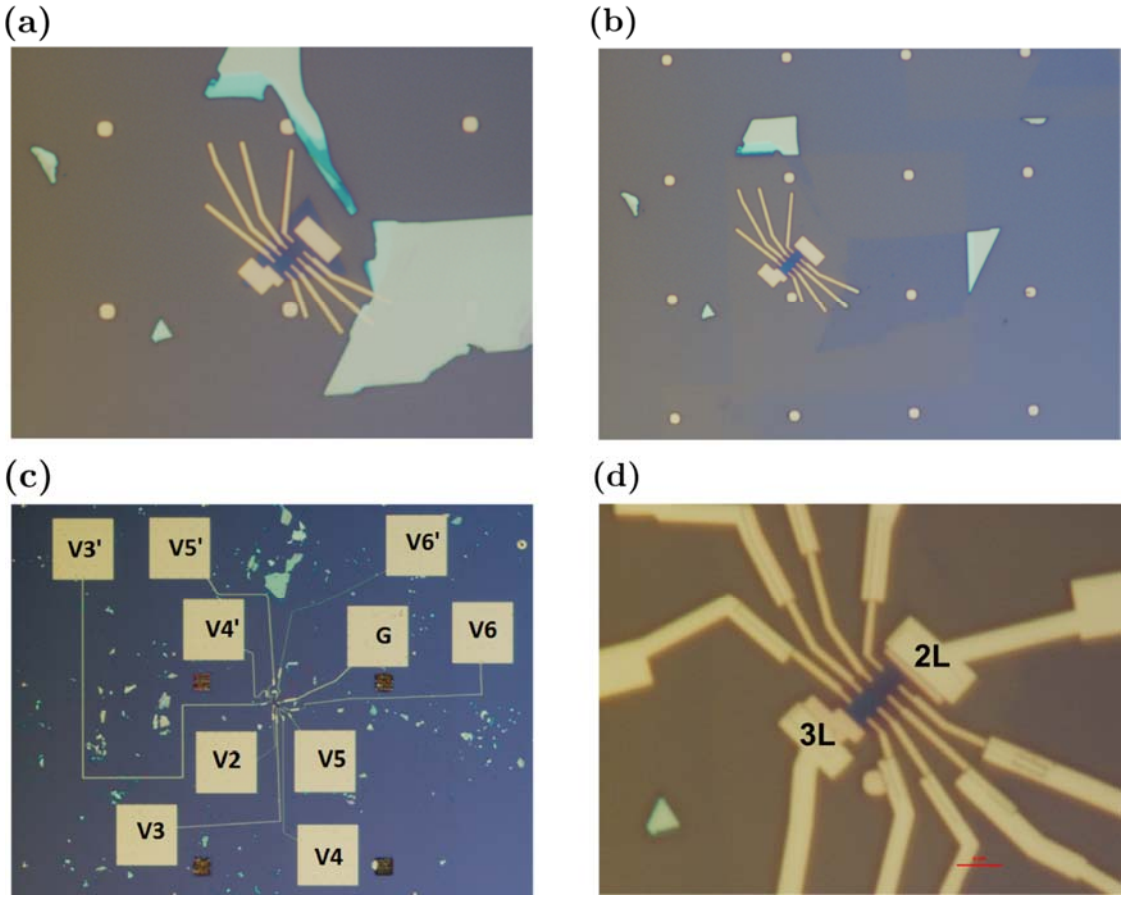

Figure 6.10: Fabrication of MoS_2 junction device. (a) Patterning of short leads to the flake (b) Defining the MoS_2 layer and cleaning up of the surrounding area using a SF_6/Ar plasma etch (c) Connecting the short leads to the contact pads. (d) Zoomed in picture of finished device. The 3L region is to the left and 2L region is to the right.

The various pads in Figure 6.10(c) are labeled as follows: V_2 and G are the current leads; V_2 is connected to 3L region and G to 2L region. V_3/V_3' and V_4/V_4' are voltage leads connected to the 3L portion. V_5/V_5' and V_6/V_6' are voltage leads connected to the 2L portion.

Initially, Ti/Au (3 nm/100 nm) was used for contacting early devices. Then, a stack of Al/Cr/Au (16 nm/ 3 nm/ 25 nm) was tried [153]. However, it was realized that the Al got oxidized over time and could be a source of increased contact resistance. In the final device presented here, Au contacts (50 nm) were used. It was realized that for good adhesion to SiO_2, Ti/Au (1 nm/100 nm) was necessary for the contact pads.

6.3 Transport measurements across the junction

Transport measurements were performed using a probe station and a semiconductor parameter analyzer (Agilent B1500A). The measurements were performed in a four-probe configuration for the different regions of the device. Specifically, V_2 and G acted as current leads and voltages were measured at V_3, V_4, V_5 and V_6. The current was swept from $-0.2\,\mu A$ to $+0.2\,\mu A$. The voltage drops across the various regions were then computed as $V_{ij} = V_i - V_j$. Such a plot at room temperature and various backgate voltages is shown in Figure 6.11. It can be observed that the resistance across the junction R_{45} is much higher than that of the individual layers. In case of the non-linear $V_{45} - I$ curves, the resistance is estimated from the linear portion of the curve near zero bias. In addition, it is seen that the resistance decreases as the backgate bias is increased to positive values i.e. as the layers become more conductive.

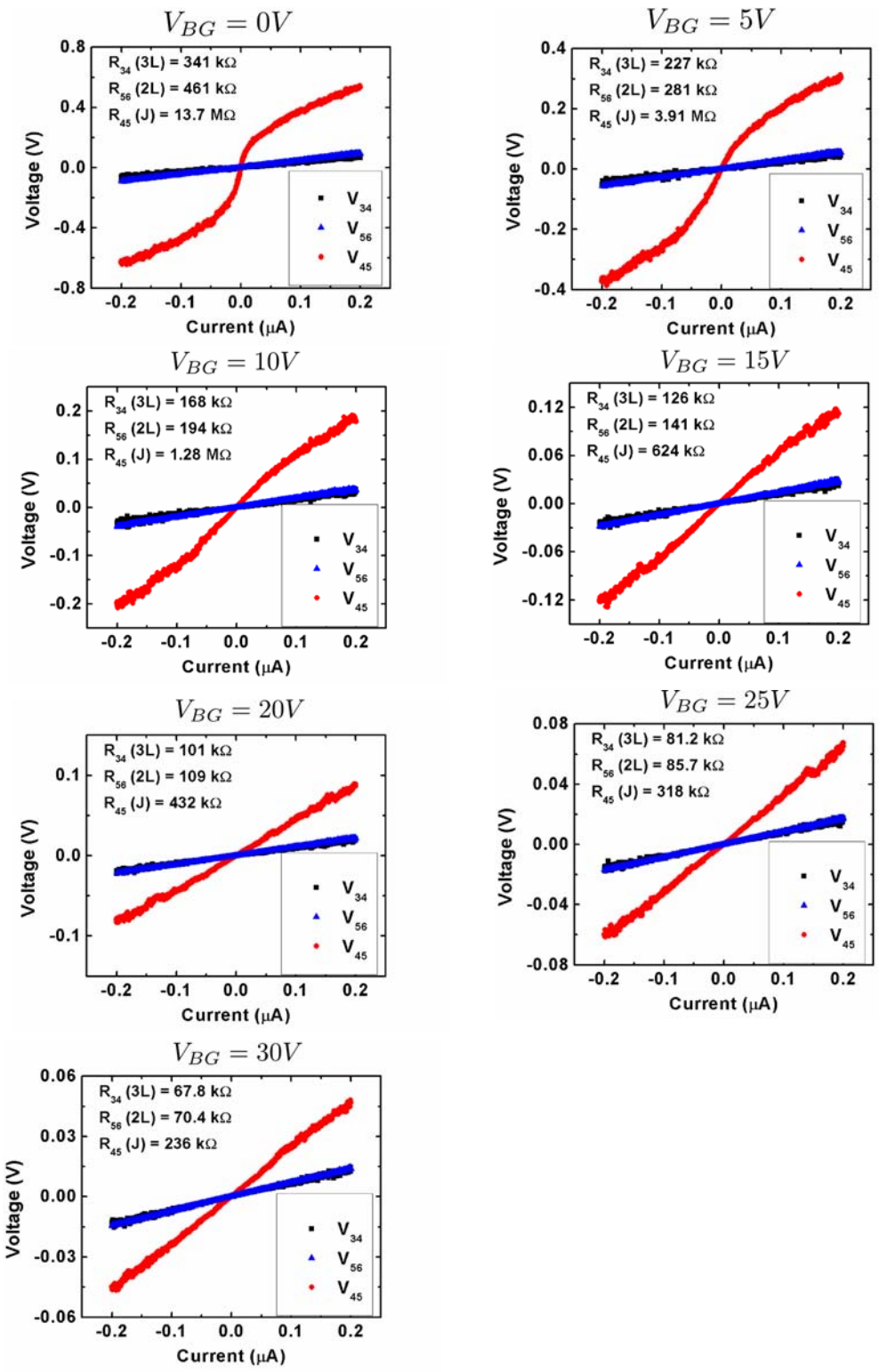

Figure 6.11: Plot of I vs voltage drops across various regions of the device. The resistance of the 3L (R_{34}) and 2L (R_{56}) regions is much smaller than that of the junction (J).

Figure 6.12 shows conductance of the various regions plotted as a function of backgate bias. The data is obtained by applying a constant voltage of 0.5V between V_2 and G and varying V_{BG}. The current I through the device is measured and conductances are computed using $G_{ij} = I/V_{ij}$. It is seen that the junction region turns on at much higher positive bias than the 2L/3L regions. The "true" junction conductance in Figure 6.12 is defined as $G_J^{-1} = G_{45}^{-1} - \frac{G_{34}^{-1}+G_{56}^{-1}}{2}$. Thus, $G_J$isolates the behavior of the junction by subtracting out the resistances of the 2L and 3L regions. The factor of 2 assumes a symmetrical junction (i.e. length of 2L region = length of 3L region between contacts V_4 and V_5).

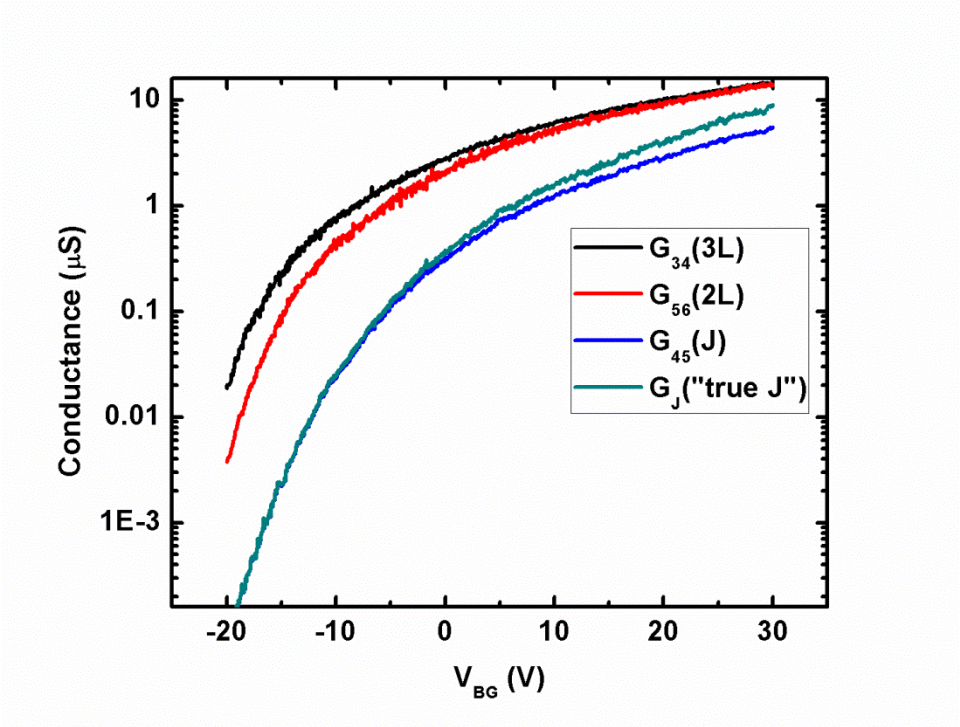

Figure 6.12: Conductance vs backgate bias

Figure 6.13 shows how the voltage drops across the different regions as the backgate bias is changed. It is observed that at negative V_{BG}, the majority of the

voltage drop occurs across the junction (i.e. between V_4 and V_5). As the backgate bias is increased to positive values, the voltage drops across the various regions becomes more equitable. As a result, it must be noted that the conductance values extracted for G_{45} in Figure 6.12 are larger than the conductance at zero bias (because of the non-linear behavior seen in Figure 6.11 for V_{45} vs I). Ideally, using smaller voltages across $V_2 - G$ would help. However, this causes practical problems in the measurement of V_{45} and V_{34}/V_{56} simultaneously because of the large resistance mis-match between R_{45} and R_{34}/R_{56} especially at low V_{BG}.

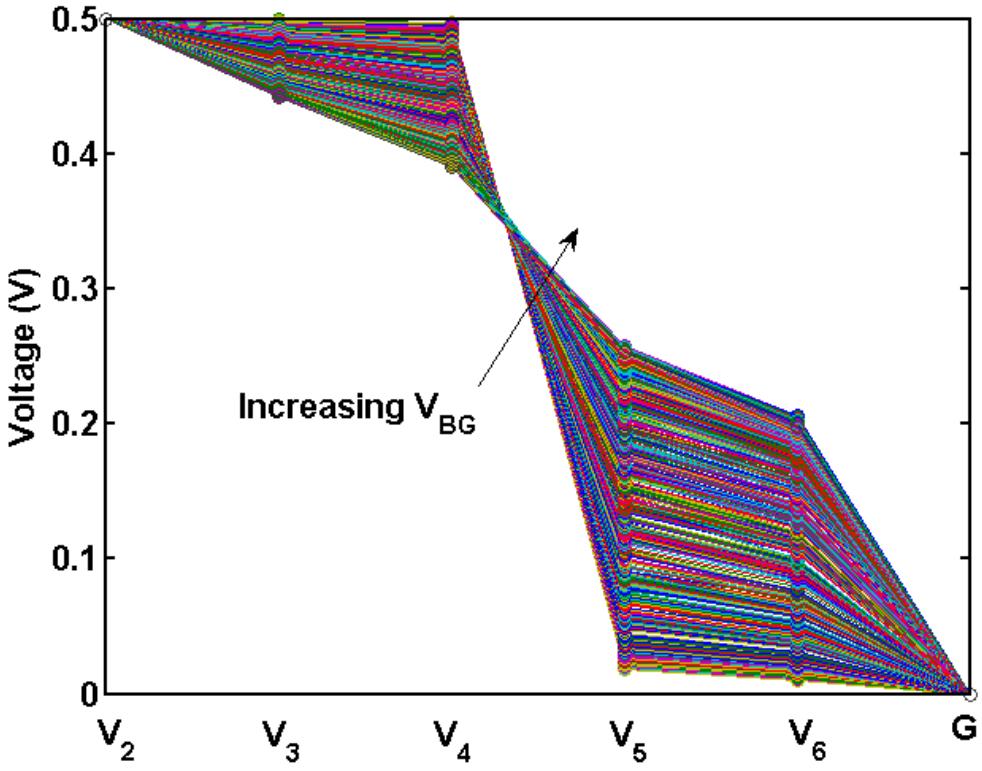

Figure 6.13: Plot showing voltage drops across the device as the backgate bias V_{BG} is varied from -20 V to +30 V.

For this device, because of issues with the cryostat, measurements could be performed at only 2 other temperature values – 197 K and 77 K. Plots of conductance vs backgate voltage at the three temperatures are shown in Figure 6.14. It may be noted that the turn-on happens for higher positive gate voltage biases as the temperature is lowered.

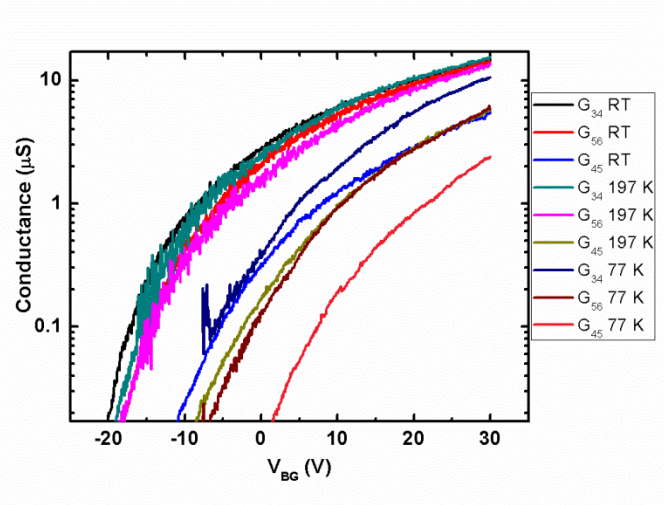

Figure 6.14: Conductance vs backgate bias for different temperatures

Figures 6.15, 6.16 and 6.17 plot low-bias conductances (apropos values obtained in Figure 6.11) G_{34}, G_{56} and $G_J$as a function of $1/T$ for various values of V_{BG}. In case of G_{34} and G_{56}, we observe an activated behavior with temperature for $V_{BG} = 0V$. This may be fitted using an activation energy E_A such that $G = G_0 e^{-\frac{E_A}{k_B T}}$. At $V_{BG} = 0V$, the extracted value of E_A are 16.6 meV and 20.2 meV for G_{34} and G_{56} respectively. For higher values of V_{BG}, the activated behavior weakens and even non-monotonic behavior of conductance with temperature is observed. The junction region G_J does not exhibit activated behavior in the range of measured temperatures and V_{BG}.

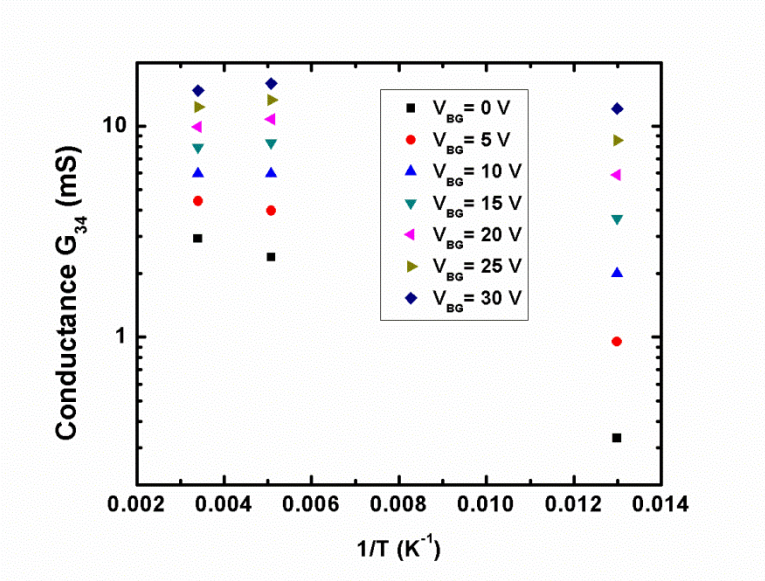

Figure 6.15: G_{34} for 3L region vs $1/T$ for various V_{BG}

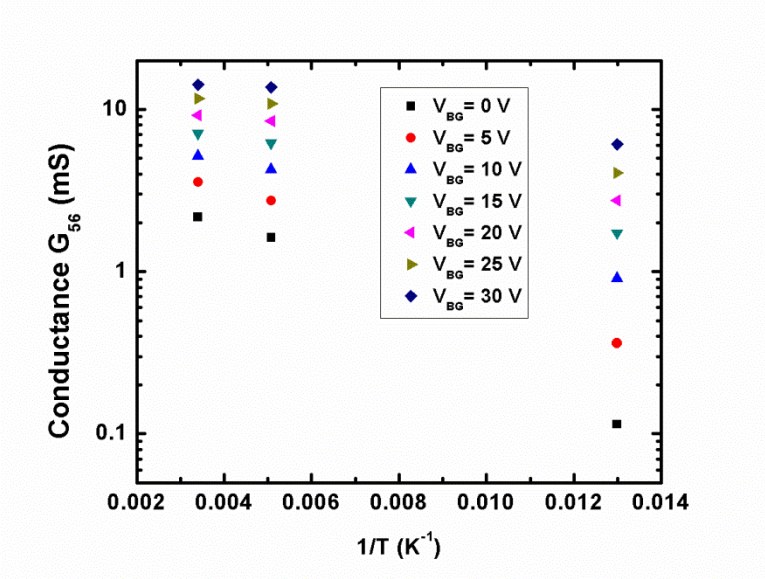

Figure 6.16: G_{56} for 2L region vs $1/T$ for various V_{BG}

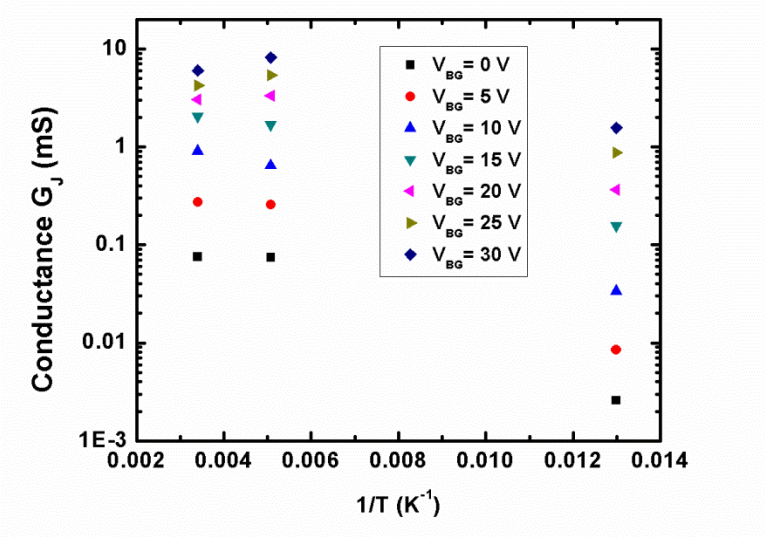

Figure 6.17: G_J for junction region vs $1/T$ for various V_{BG}

In order to figure out if the conduction happens exclusively in the top layer of MoS_2 onto which contacts are deposited or happens in all layers simultaneously, we plot dG/dV_{BG} vs V_{BG} for the 3L and 2L regions. If conduction happens exclusively in the top layer, we would expect dG/dV_{BG} for the 3L region to be lower than that of the 2L region (assuming equal mobility in the top layers of both), because lesser charges would be induced in the topmost layer. However, as Figure 6.18 shows the differential change in conductance of the 3L region is greater than that of the 2L region for a substantial portion of the V_{BG} sweep. Thus, we may deduce that transport occurs through all layers of MoS_2.

Finally, we speculate on the origin of the transport barrier. It is known that grain boundaries and edges have dangling bonds and uncompensated charges. It is conceivable that at the junction between the 2L and 3L region, there exist charges which locally deplete the MoS_2 region on either side of the junction. This causes the

junction to turn on at increased positive gate voltages. A simple model for the junction may be made by considering the junction as a region with a delayed turn-on voltage V_D and having an "effective number of squares" N_J.

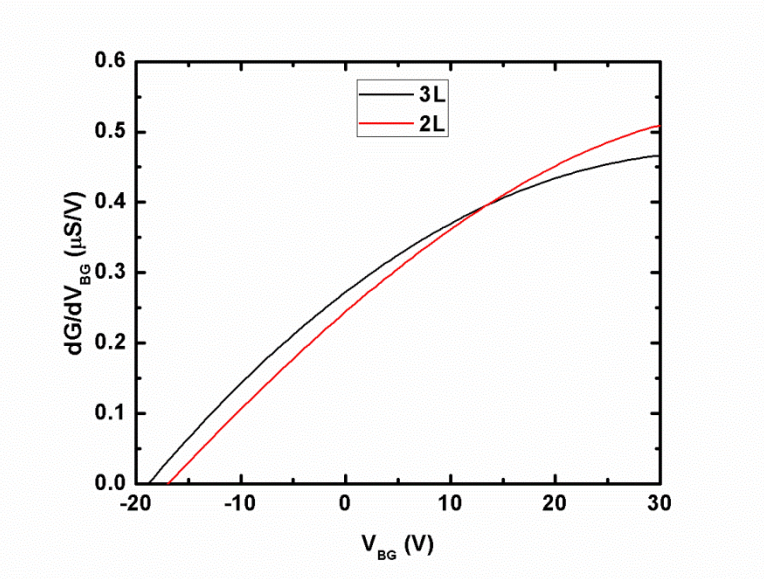

Figure 6.18: dG/dV_{BG} for 3L and 2L MoS_2

These parameters may be extracted by comparing G_J with G_{34}. Figure 6.19 shows how G_{34} may be shifted by $V_D = +9\,V$ and scaled by $1/N_J = 0.5$, in order to approximately coincide with G_J. Thus, the junction region has an "effective length" equal to twice the length of the individual layer regions. This indicates degraded mobility at the interface. Thus, the junction maybe considered as a region with shifted threshold voltage and degraded mobility.

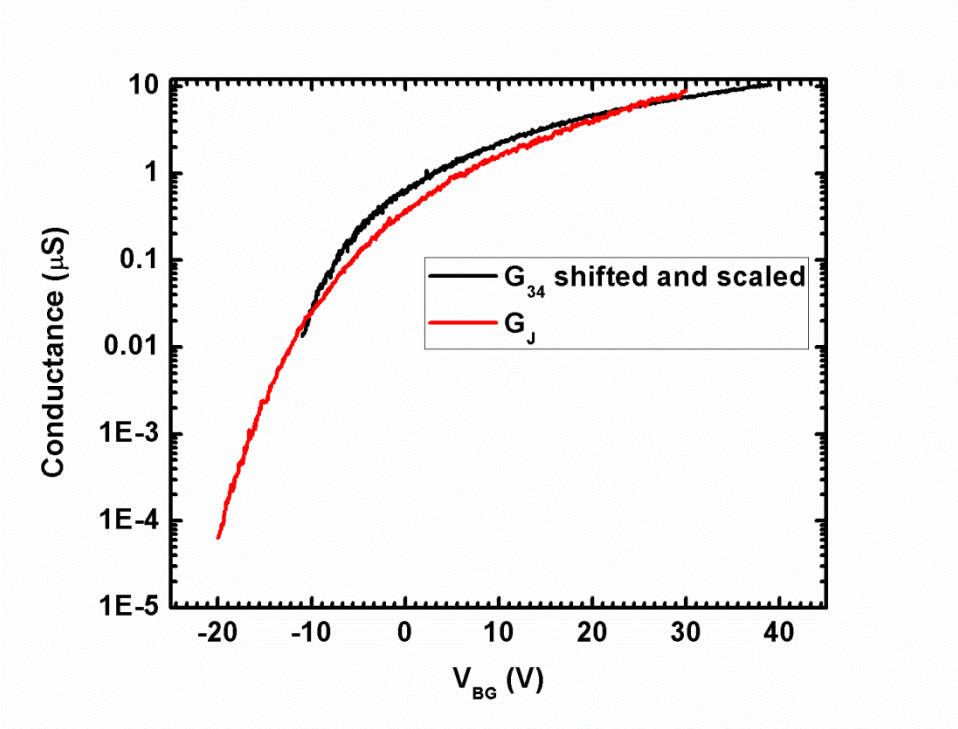

Figure 6.19: G_{34} shifted by $V_D = +9\ V$ and scaled by 0.5 × to coincide with G_J.

6.4 Conclusions

We have successfully fabricated devices to explore transport between different number of layers of MoS_2. The transport data suggests that there exists a significant barrier for electron transport at the junction between the layers at low values of V_{BG} i.e. when the individual layers are resistive. The junction may be modeled as region with increased threshold voltage and degraded mobility. Further studies will be needed in order to identify the origin of the barrier at the interface.

CHAPTER 7

OTHER RELATED PROJECTS ON LAYERED MATERIALS

In this chapter, we describe three short related projects using layered materials:

1. Fabrication and characterization of dual-gated bilayer graphene devices
2. Characterization of the graphene-Si interface
3. h-BN balloons

7.1 Dual-gated bilayer graphene

The crystal structure of bilayer graphene is shown in Figure 7.1. It consists of two graphene monolayers stacked in an AB configuration. Pristine bilayer graphene has a unique low energy bandstructure consisting of four parabolic bands two of which are degenerate at the K and K' points [154]. It has been shown that in the presence of a vertical electric field between the layers of bilayer graphene, a bandgap is induced in the material (see Figure7.2) [155-158]. In optical experiments, a tunable bandgap of upto ~250 meV has been observed [156,158].

I undertook a project trying to study the photoresponse of bilayer graphene as the bandgap is tuned using top and bottom gates. However, it was found that the lamp in the Fourier transform infrared (FTIR) spectrometer was not powerful enough to induce a photoresponse in the bilayer graphene device. Also, around this time, a hot electron bolometer using dual-gated bilayer graphene was demonstrated at University of Maryland [159]. So, the project was not pursued further. In the following, we describe device fabrication and a few salient results obtained during the project.

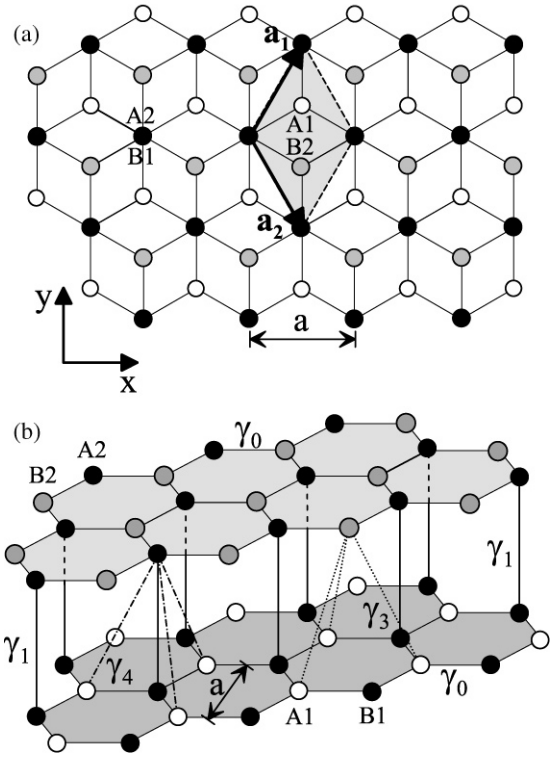

Figure 7.1: (a) Top-view (b) Side-view of bilayer graphene crystal structure. Atom A2 in layer 2 has a corresponding atom B1 in layer 1. Atom B2 in layer 2 and atom A1 in layer 1 are rotated from each other by 60°. Adapted from [154].

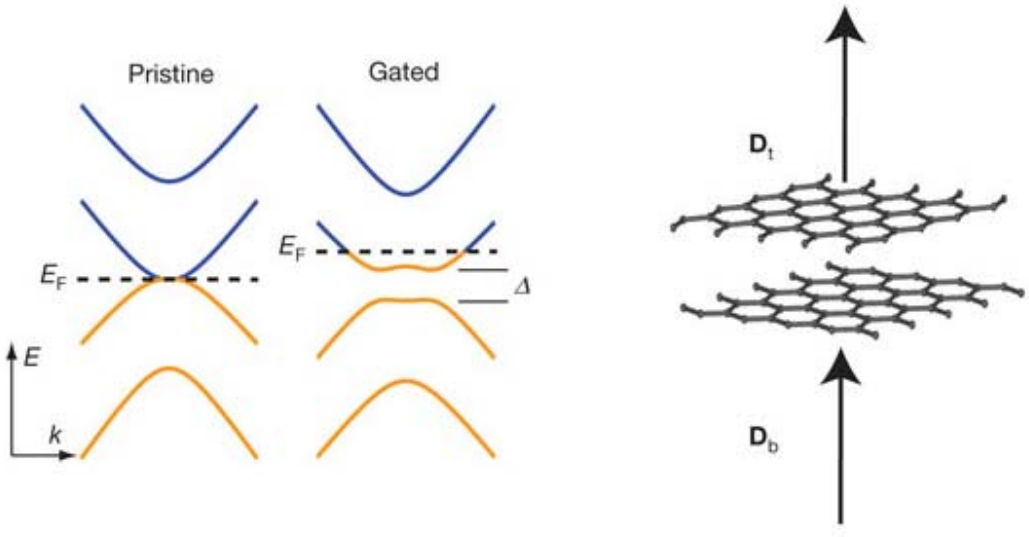

Figure 7.2: Low energy bandstructure of bilayer graphene under pristine and gated conditions. A vertical electric field creates a gapped material. Adapted from [156].

Bilayer graphene was obtained by mechanical exfoliation onto SiO_2/Si using a process similar to that described in Section 6.2 (Figure 7.3). Bilayer graphene was then identified optically and using Raman spectroscopy. The Raman *2D* band of bilayer graphene has a unique shape which can be fit by four Lorentzians (Figure 7.4) [36].

Figure 7.3: Optical micrograph of bilayer graphene exfoliated on SiO_2/Si. The gold square on the image is $\sim 5\ \mu m \times 5\ \mu m$.

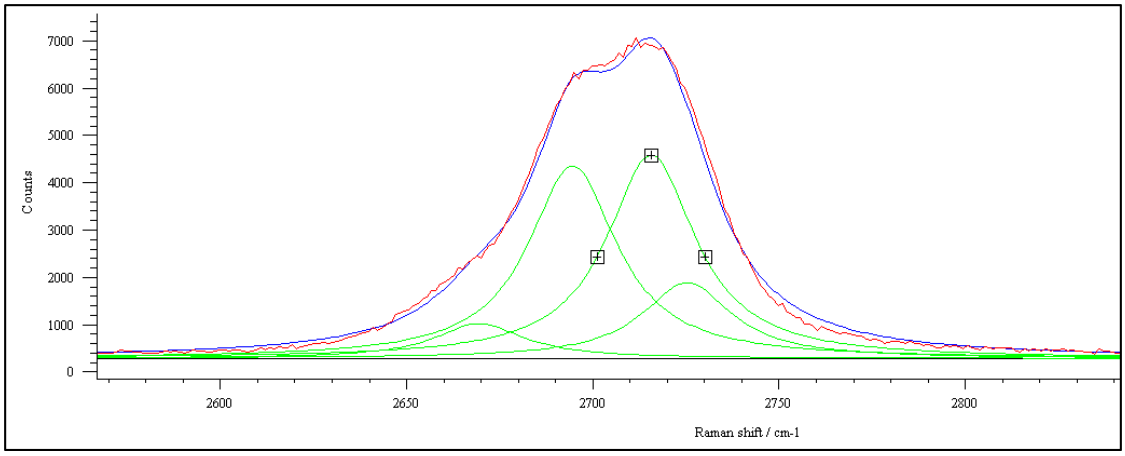

Figure 7.4: Raman *2D* peak lineshape of bilayer graphene. Fit using four Lorentzians is shown.

In addition, reflection spectroscopy was used to confirm layer number. This was performed using a halogen lamp and monochromator based setup shown in Figure 7.5(a). A motorized stage was used to move between the sample and the substrate at each wavelength. The contrast $\left|\frac{R(BLG)-R(SiO_2)}{R(SiO_2)}\right|$ is plotted in Figure 7.5(b). The fit was obtained using Fresnel equations and assuming a value of optical conductivity $\sigma_G = \frac{e^2}{4\hbar}$ per layer of graphene [160-162].

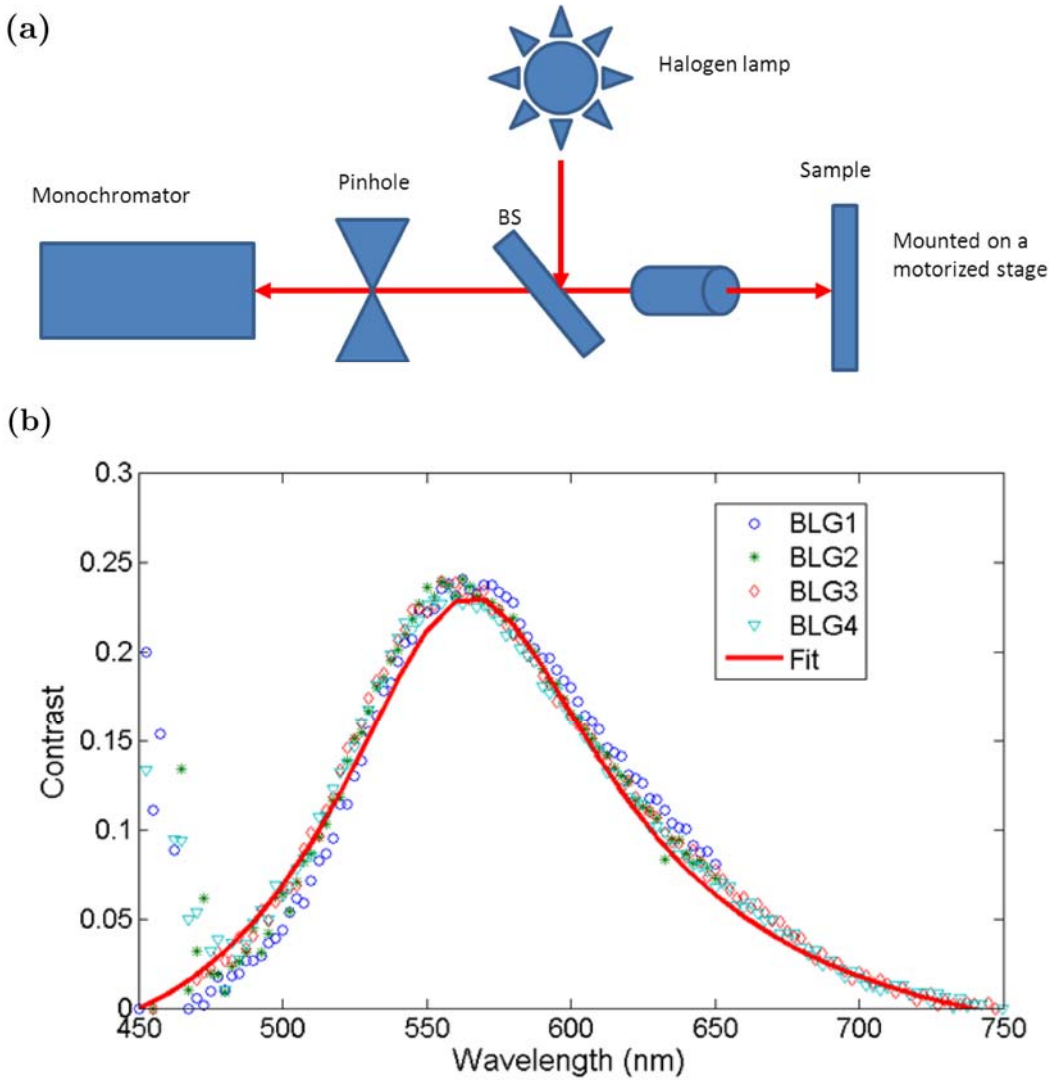

Figure 7.5: Identification of a bilayer using reflection spectroscopy. (a) Schematic of reflection spectroscopy setup. (b) Data for four bilayer graphene flakes (BLG1-BLG4) and fit using Fresnel equations.

Subsequently, the device was fabricated using photolithography or e-beam lithography. Contacts were made to the flakes using Cr/Au (1 nm/100 nm). E-beam evaporated alumina (2.5 nm on crystal monitor, 4.4 nm from ellipsometer) was used to seed the top gate dielectric layer, which was followed by ~20 nm of ALD alumina (200 ^{o}C thermal process) and a thin (15 nm) top gate metal layer of Au. Shown below

is a picture of a fabricated device. Figure 7.6 shows an optical image of fabricated device.

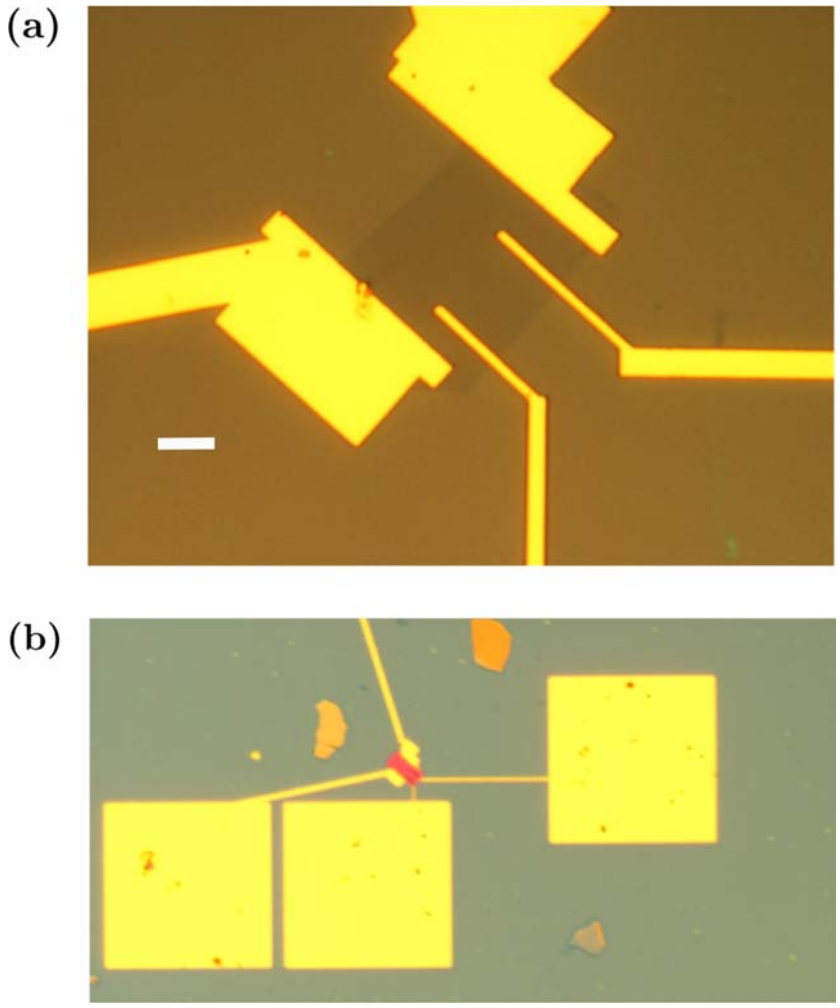

Figure 7.6: (a) Picture of a bilayer device after deposition of contacts and ALD alumina (b) Picture of dual-gated bilayer graphene device after deposition of thin top gate metal.

Electrical characterization of the devices was performed in a liquid He-cooled cryostat (Figure 7.7). Devices showed top and bottom gate modulation as exhibited in the plots below. Devices usually show hysteresis at room temperature, probably

because of trapped charges in the dielectric layers (see Figure 7.8). Upon cooling down to T < 10 K, hysteresis is negligible (Figure 7.9).

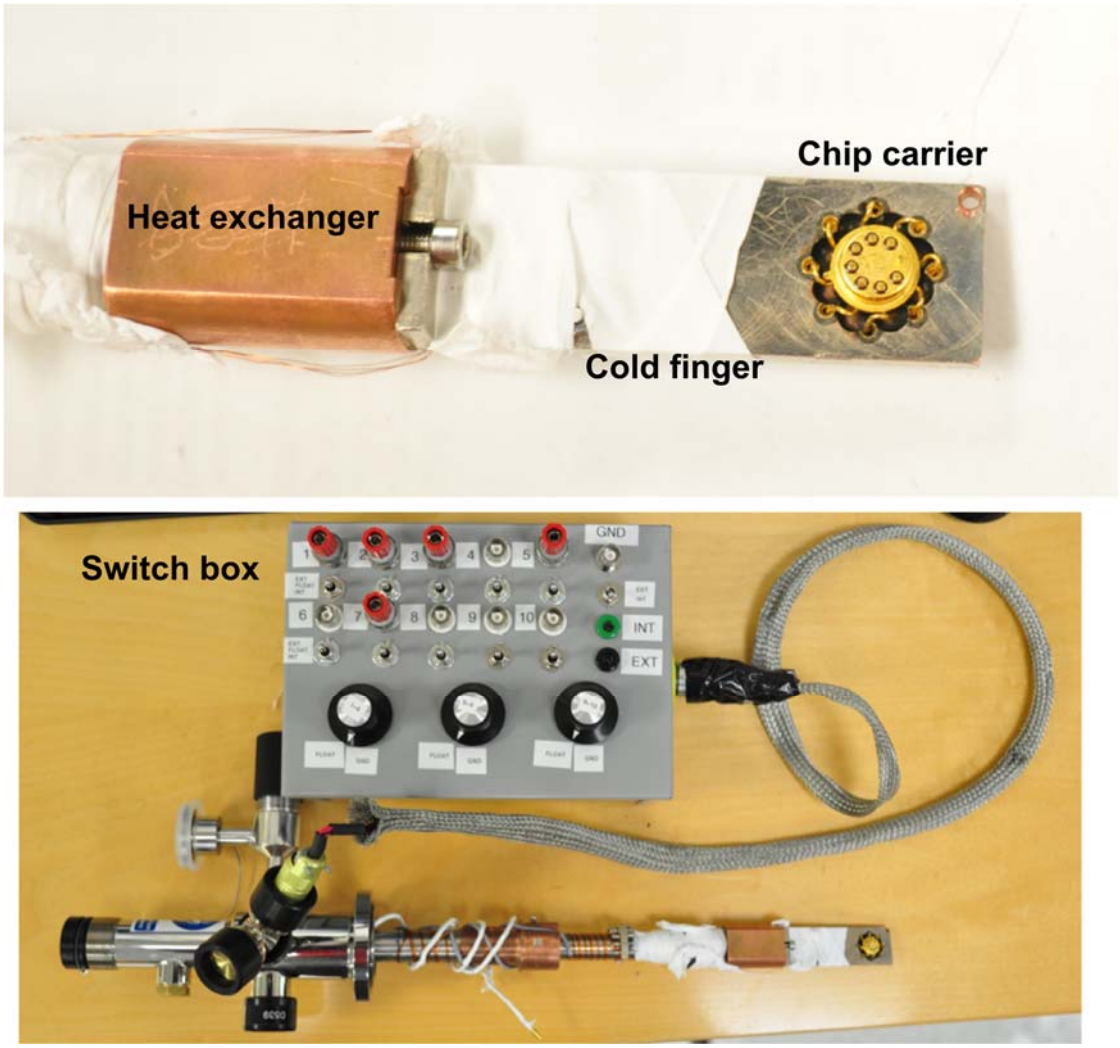

Figure 7.7: Cryostat and switchbox for electrical characterization of bilayer graphene device

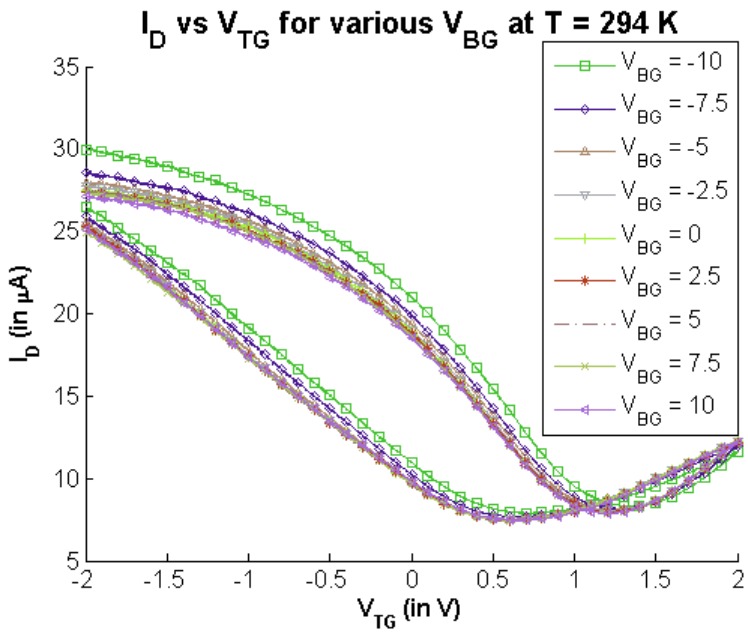

Figure 7.8: Drain current I_D vs top gate voltage V_{TG} for various back gate voltages V_{BG} from $-10\,V$ to $10\,V$. The two curves corresponding to the same color represent forward and backward sweeps. Hysteresis is clearly observed.

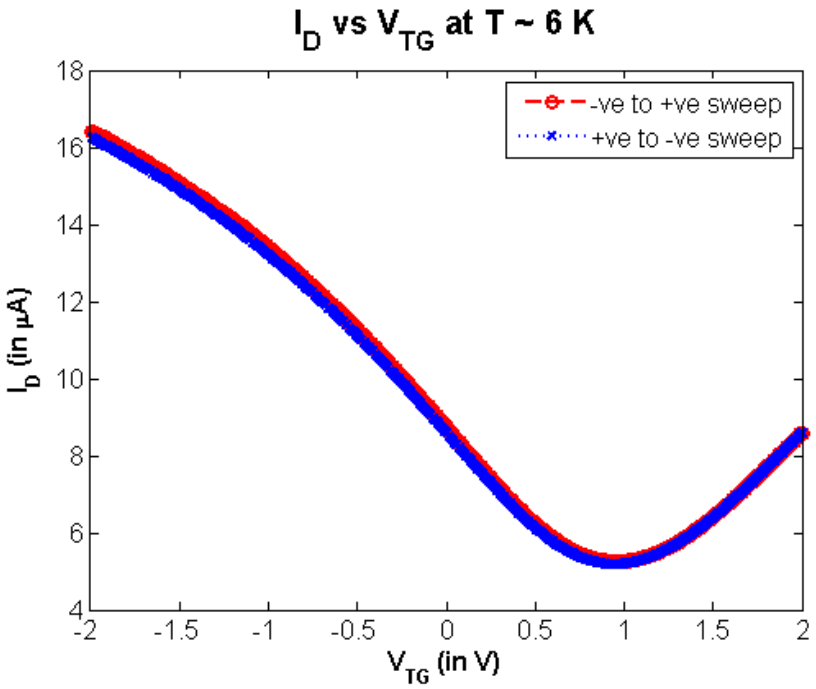

Figure 7.9: Low temperature sweep of top gate voltage V_{TG} showing no observable hysteresis.

Subsequent characterization was performed at low temperature. Figure 7.10 shows resistance of the device plotted as a function of top gate voltage V_{TG} for various back gate biases V_{BG}. The position of the charge neutrality point increases to more positive V_{TG} as V_{BG} increases. A two-dimensional plot of R vs $V_{TG} - V_{BG}$ is shown in Figure 7.11. The positions of the maxima in resistance are plotted in Figure 7.12. From the slope of the plot, the ratio between the top and bottom gate capacitances may be obtained. Also, the offset values of the top and back gate voltages for ~zero bandgap are marked on the plot. This corresponds to the point on the megasweep plot (Figure 7.11) where the resistance at the charge neutrality point is the minimum.

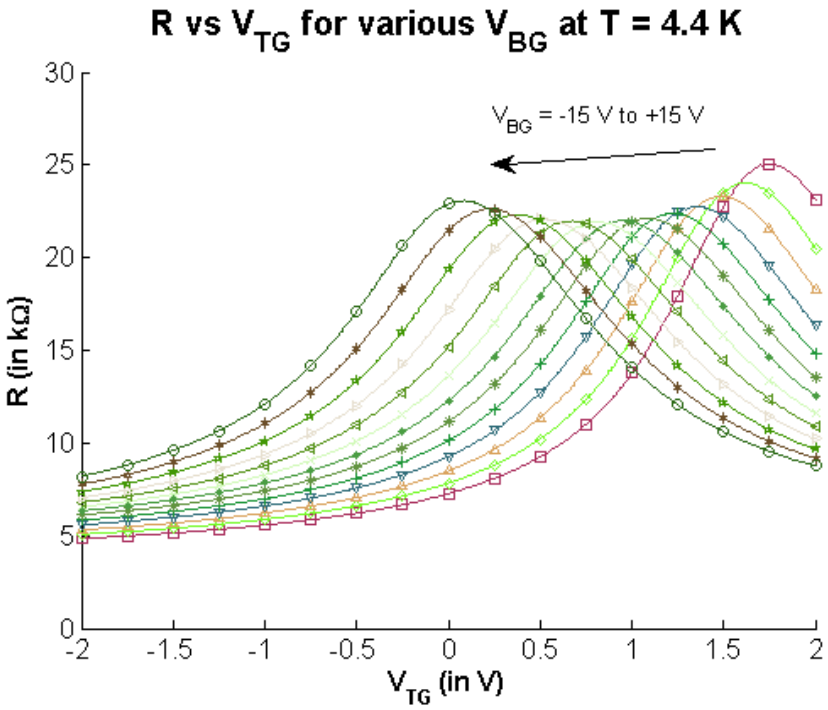

Figure 7.10: Bilayer graphene device resistance R vs V_{TG} for different V_{BG} at 4.4 K.

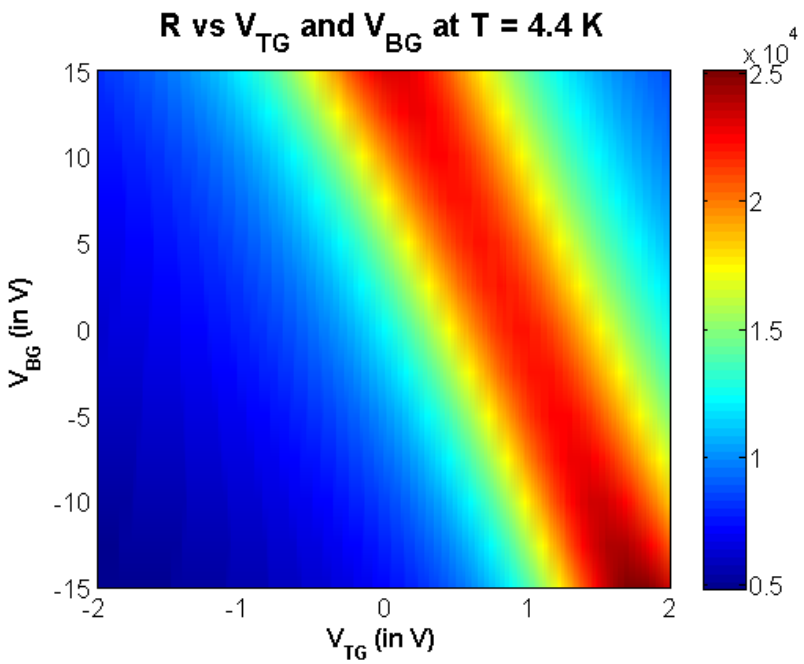

Figure 7.11: Two dimensional plot of R vs $V_{TG} - V_{BG}$

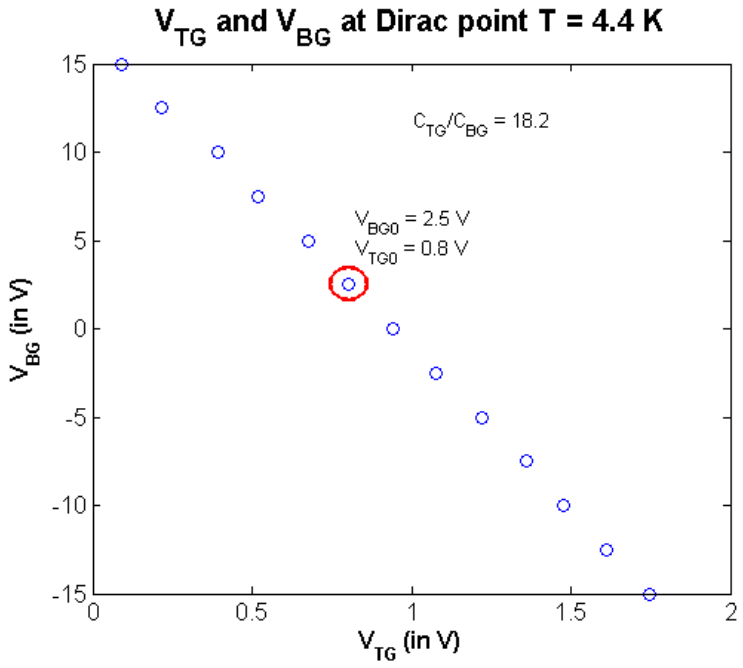

Figure 7.12: Plot of V_{BG} vs V_{TG} at the charge neutrality points. Ratio of top gate to back gate capacitance is 18.2.

Evidence of band opening may be obtained from the $I-V$ sweeps of the device at the charge neutrality points. Such a sweep is shown in Figure 7.13 for a different device and demonstrates the effect of a gap opening at the contacts. The $I-V$ characteristics change from almost linear to non-linear as the magnitude of the gap increases. This is similar to the data reported in [163].

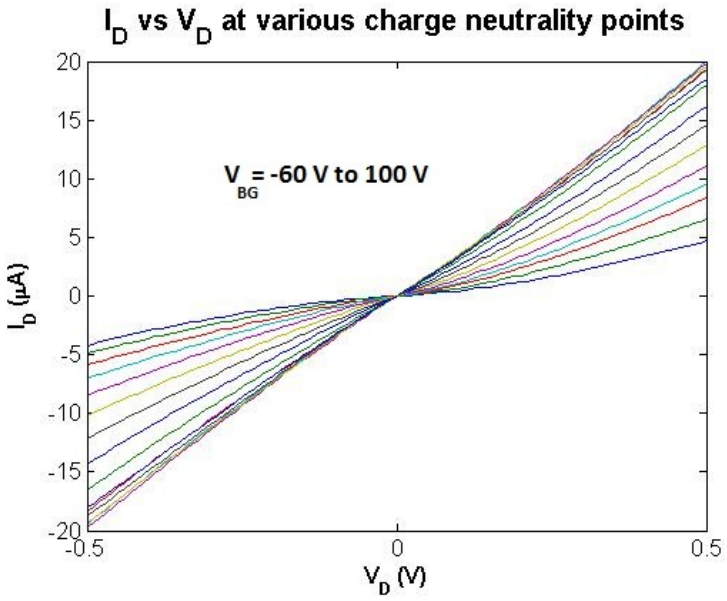

Figure 7.13: $I-V$ characteristics at the charge neutrality points. As the magnitude of the gap increases, the sweeps become increasingly non-linear.

7.2 Characterization of graphene-Si interface

A project was undertaken to study the Schottky barrier at the graphene-Si interface using CVD graphene grown on Cu foil. A description of this study is presented next.

Graphene was grown on Cu foil obtained from Alfa Aesar. Growth details are presented in [164]. The graphene on Cu foil was then coated with PMMA on one side. The back side of the Cu foil was exposed to oxygen plasma to remove the graphene on

that side. Cu was then etched away using Transene Cu etchant. The PMMA/graphene stack was then scooped up and rinsed multiple times in DI water. Simultaneously, $1-5\ \Omega cm$ n-Si substrates were immersed in BOE 6:1 to remove the native oxide. The PMMA/graphene stack was then transferred on to the Si wafer and left to dry. Subsequently, PMMA was removed by dissolving in acetone/dichloromethane. Devices were fabricated using photolithography and oxygen plasma etching to isolate the devices. Au was used as the contact metal. In addition to the Au/graphene/Si experimental devices, a set of control devices with Au/Si were also fabricated.

Results of *I-V* and *C-V* measurements are shown in Figure 7.14 and Figure 7.15. The *I-V* plots showed rectifying behavior which was modeled using a Schottky diode equation. Ideality factors for the graphene-Si diode were typically > ~2, indicating that the interface was not ideal. From the *C-V* plots, Schottky barrier heights were extracted using a procedure similar to that described in Chapter 5. The graphene-Si interface was found to exhibit a barrier height of 0.59 eV.

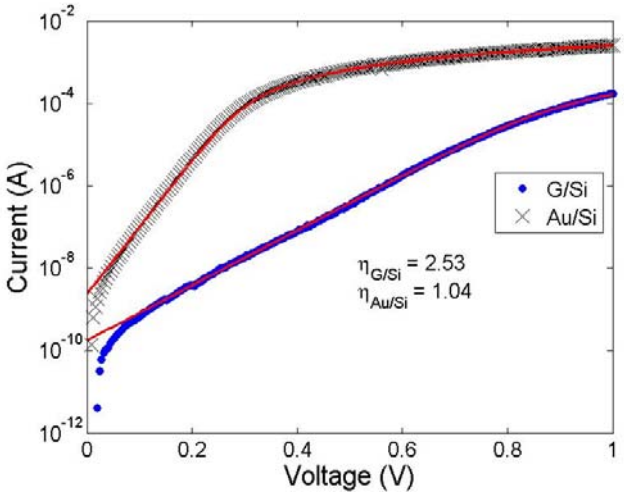

Figure 7.14: *I-V* plot of graphene-Si and Au-Si Schottky diodes.

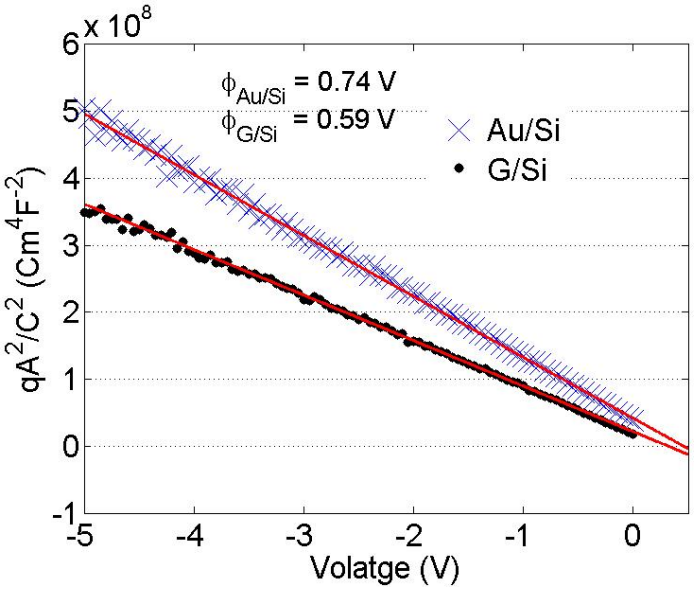

Figure 7.15: Reverse bias *C-V* plot of graphene-Si and Au-Si diodes.

7.3 h-BN balloons

In this section, we describe a fun project similar to that published in [17], where we employ hexagonal boron nitride (h-BN) as impermeable atomic membranes to contain gases.

Silicon wafers with 80 nm thermal oxide were etched using reactive ion etching to create arrays of holes ~ 1 μm deep. The diameters of the holes ranged from 1 μm – 10 μm. Hexagonal boron nitride single crystals were mechanically exfoliated on top of the trenches using scotch tape. Holes spanned by thin boron nitride layers were identified using optical microscopy (Figure 7.16). Raman spectroscopy on the layers confirmed their hexagonal crystal structure, which exhibits a prominent E_{2g} stretching mode at ~ 1366 cm^{-1} [165] (Figure 7.17). Atomic force microscopy (AFM)

on the covered holes suggested that the few-layer h-BN was depressed into the hole by ~ 200 nm (Figure 7.18).

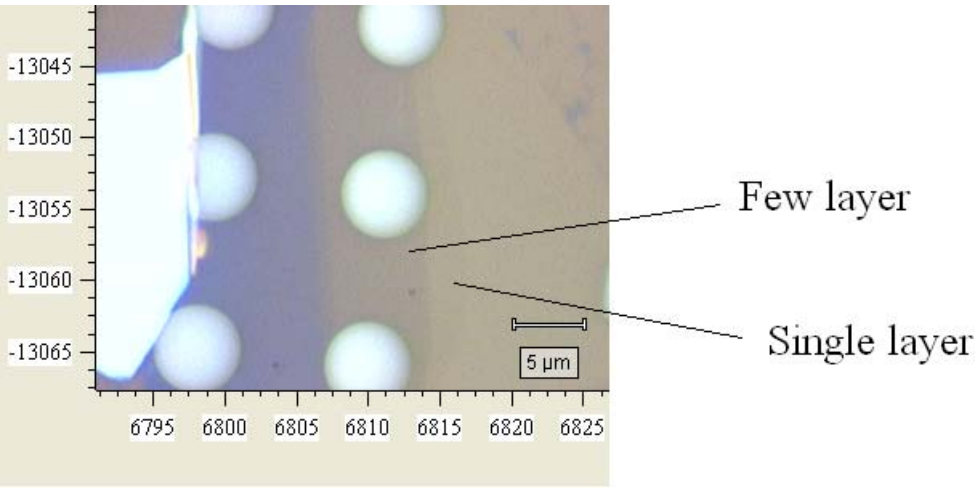

Figure 7.16: Optical microscope image showing trenches in SiO2/Si covered by few layer h-BN.

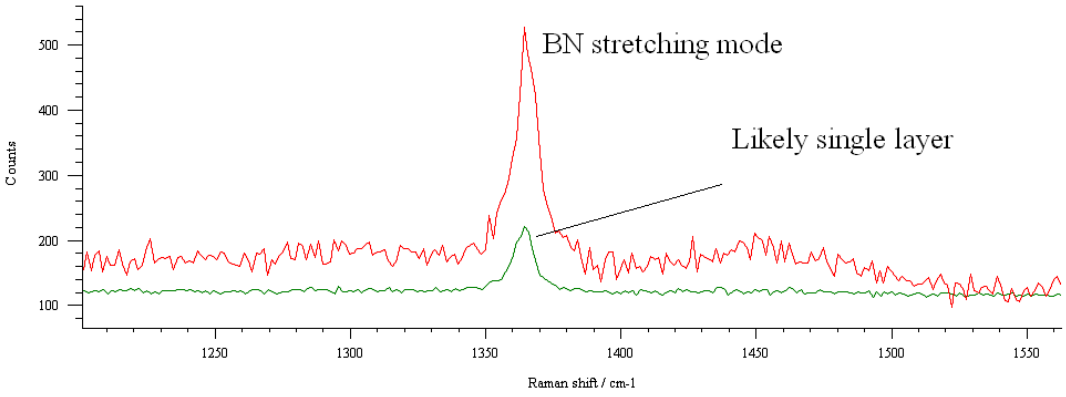

Figure 7.17: Raman spectra of h-BN showing the prominent stretching mode at ~ 1366 cm^{-1}.

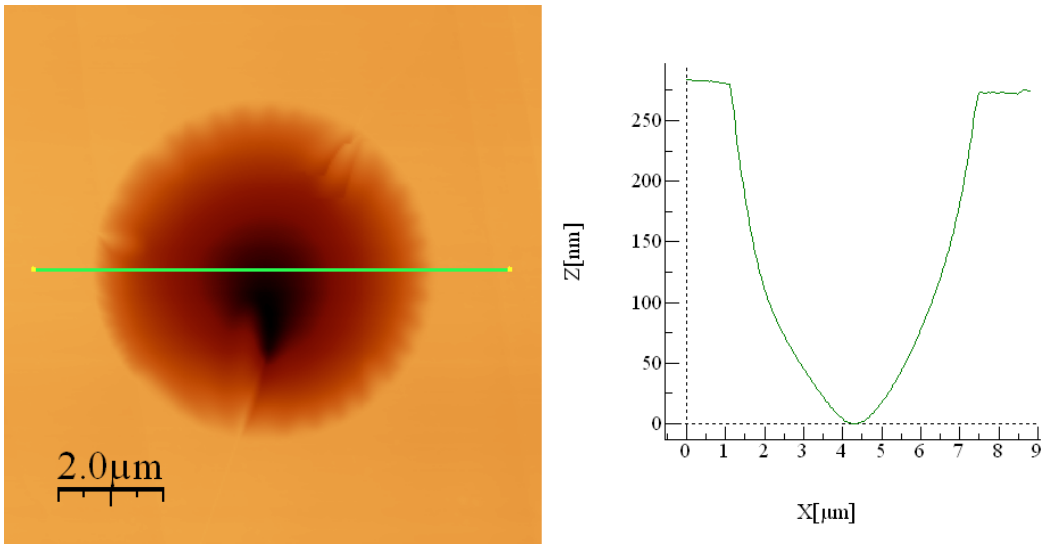

Figure 7.18: AFM image of an as-prepared BN micro-chamber. The BN film appears to be depressed inside the hole.

In order to find out the gas-containing capability and monitor leak rates of the few-layer h-BN micro-chambers, the chip was kept inside an enclosed chamber under 35 psi (2.4 atm) of N_2 for 24 hours. Upon removal from the chamber, the micro-chambers were observed using AFM. The N_2 contained inside the chamber at higher pressure caused the BN membrane to balloon up (Figure 7.19). The membrane was monitored over the course of 76 hours and the leak rate was found to be extremely low, as evidenced by the small reduction of the bulge (282 nm – 262 nm = 20 nm) (Figure 7.20).

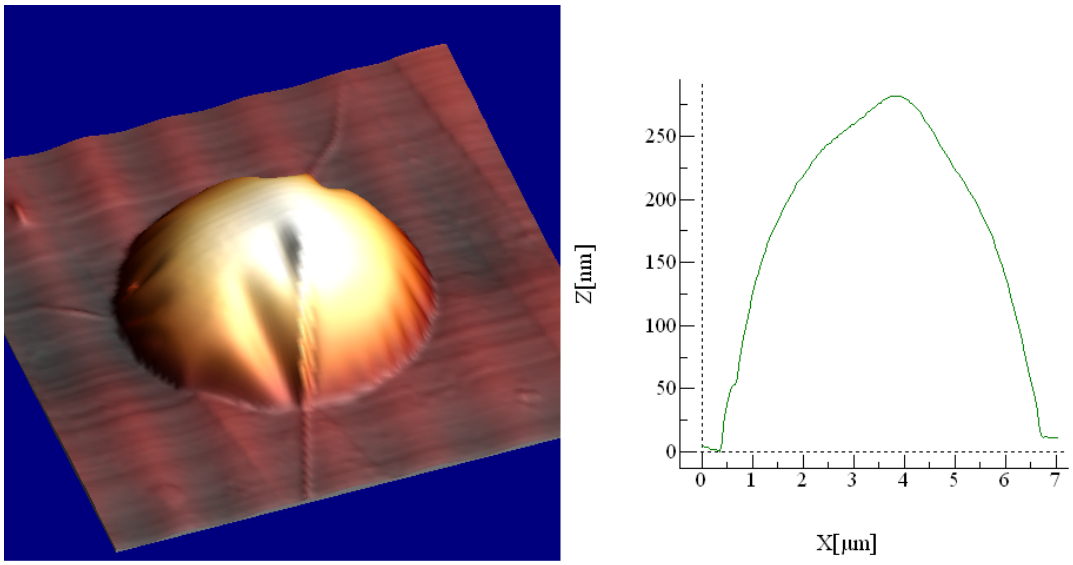

Figure 7.19: Inflated BN micro-chamber at time t = 0.

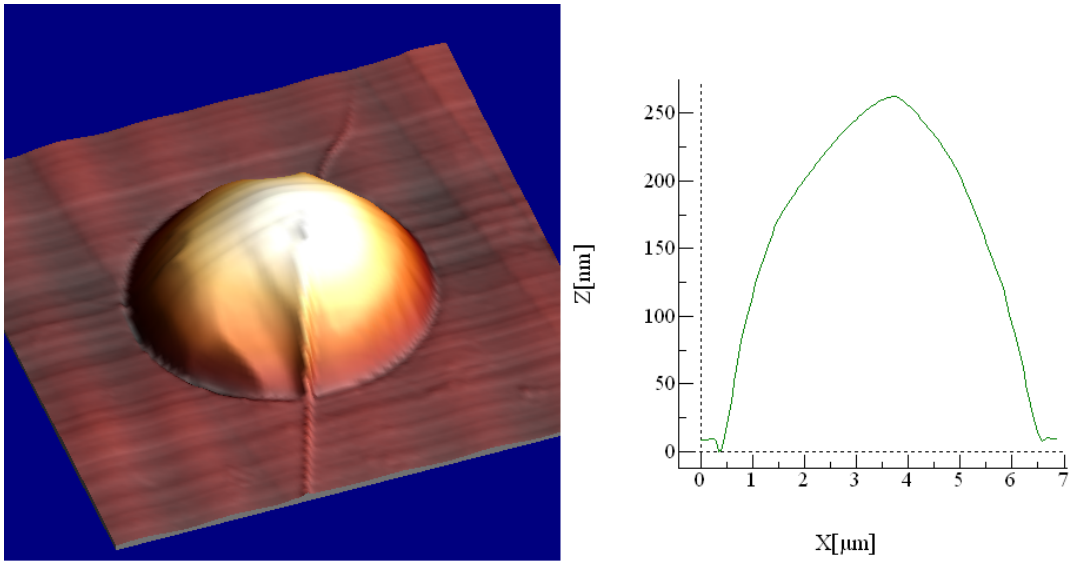

Figure 7.20: BN micro-chamber after t = 76 h. The very small reduction in the bulge indicates a miniscule leak rate.

BIBLIOGRAPHY

[1] J. C. Meyer, C. O. Girit, M. F. Crommie, and A. Zettl, Nature **454**, 319 (2008).

[2] B. Radisavljevic, A. Radenovic, J. Brivio, V. Giacometti, and A. Kis, Nature Nanotech **6**, 147 (2011).

[3] K. S. Novoselov, A. K. Geim, S. V. Morozov, D. Jiang, Y. Zhang, S. V. Dubonos, I. V. Grigorieva, and A. A. Firsov, Science **306**, 666 (2004).

[4] A. H. Castro Neto, F. Guinea, N. M. R. Peres, K. S. Novoselov, and A. K. Geim, Rev.Mod.Phys. **81**, 109 (2009).

[5] F. Bonaccorso, Z. Sun, T. Hasan, and A. C. Ferrari, Nature Photon. **4**, 611 (2010).

[6] A. A. Balandin, S. Ghosh, W. Bao, I. Calizo, D. Teweldebrhan, F. Miao, and C. N. Lau, Nano Letters **8**, 902 (2008).

[7] C. Lee, X. Wei, J. W. Kysar, and J. Hone, Science **321**, 385 (2008).

[8] Eva Y Andrei and Guohong Li and,Xu Du, Reports on Progress in Physics **75**, 056501 (2012).

[9] K. S. Novoselov, A. K. Geim, S. V. Morozov, D. Jiang, M. I. Katsnelson, I. V. Grigorieva, S. V. Dubonos, and A. A. Firsov, Nature **438**, 197 (2005).

[10] K. I. Bolotin, K. J. Sikes, Z. Jiang, M. Klima, G. Fudenberg, J. Hone, P. Kim, and H. L. Stormer, Solid State Communications **146**, 351 (2008).

[11] C. R. Dean, A. F. Young, I. Meric*, et al*, Nature Nanotech **5**, 722 (2010).

[12] A. K. Geim and K. S. Novoselov, Nature Mater **6**, 183 (2007).

[13] I. Meric, M. Y. Han, A. F. Young, B. Ozyilmaz, P. Kim, and K. L. Shepard, Nature Nanotech **3**, 654 (2008).

[14] K. S. Novoselov, A. K. Geim, S. V. Morozov, D. Jiang, M. I. Katsnelson, I. V. Grigorieva, S. V. Dubonos, and A. A. Firsov, Nature **438**, 197 (2005).

[15] Y. Zhang, Y. Tan, H. L. Stormer, and P. Kim, Nature **438**, 201 (2005).

[16] C. Lee, X. Wei, J. W. Kysar, and J. Hone, Science **321**, 385 (2008).

[17] J. S. Bunch, S. S. Verbridge, J. S. Alden, A. M. van der Zande, J. M. Parpia, H. G. Craighead, and P. L. McEuen, Nano Letters **8**, 2458 (2008).

[18] J. S. Bunch, A. M. van der Zande, S. S. Verbridge, I. W. Frank, D. M. Tanenbaum, J. M. Parpia, H. G. Craighead, and P. L. McEuen, Science **315**, 490 (2007).

[19] F. Schedin, A. K. Geim, S. V. Morozov, E. W. Hill, P. Blake, M. I. Katsnelson, and K. S. Novoselov, Nature Mater **6**, 652 (2007).

[20] R. R. Nair, P. Blake, A. N. Grigorenko, K. S. Novoselov, T. J. Booth, T. Stauber, N. M. R. Peres, and A. K. Geim, Science **320**, 1308 (2008).

[21] F. Rana, Nanotechnology, IEEE Transactions on **7**, 91 (2008).

[22] C. Berger, Z. Song, T. Li*, et al*, The Journal of Physical Chemistry B **108**, 19912 (2004).

[23] C. Berger, Z. Song, X. Li*, et al*, Science **312**, 1191 (2006).

[24] K. V. Emtsev, A. Bostwick, K. Horn*, et al*, Nature Materials **8**, 203 (2009).

[25] J. Hwang, V. B. Shields, C. I. Thomas, S. Shivaraman, D. Hao, M. Kim, A. R. Woll, G. S. Tompa, and M. G. Spencer, J. Cryst. Growth **312**, 3219 (2010).

[26] M. A. Fanton, J. A. Robinson, C. Puls*, et al*, ACS Nano **5**, 8062 (2011).

[27] J. Hwang, M. Kim, D. Campbell*, et al*, ACS Nano **7**, 385 (2013).

[28] Q. Yu, J. Lian, S. Siriponglert, H. Li, Y. P. Chen, and S. Pei, Appl. Phys. Lett. **93**, 113103 (2008).

[29] X. Li, W. Cai, J. An*, et al*, Science **324**, 1312 (2009).

[30] R. M. Tromp and J. B. Hannon, Phys. Rev. Lett. **102**, 106104 (2009).

[31] T. Ohta, N. C. Bartelt, S. Nie, K. Thürmer, and G. L. Kellogg, Physical Review B **81**, 121411 (2010).

[32] C. Riedl, C. Coletti, T. Iwasaki, A. A. Zakharov, and U. Starke, Phys. Rev. Lett. **103**, 246804 (2009).

[33] C. Riedl, C. Coletti, and U. Starke, Journal of Physics D **43**, 374009 (2010).

[34] U. Starke and C. Riedl, Journal of Physics: Condensed Matter **21**, 134016 (2009).

[35] C. H. Lui, Z. Li, Z. Chen, P. V. Klimov, L. E. Brus, and T. F. Heinz, Nano Letters **11**, 164 (2011).

[36] L. M. Malard, M. A. Pimenta, G. Dresselhaus, and M. S. Dresselhaus, Physics Reports **473**, 51 (2009).

[37] S. Shivaraman, M. V. S. Chandrashekhar, J. Boeckl, and M. Spencer, Journal of Electronic Materials **38**, 725 (2009).

[38] E. Rollings, G.-H. Gweon, S. Y. Zhou, B. S. Mun, J. L. McChesney, B. S. Hussain, A. V. Fedorov, P. N. First, W. A. de Heer, and A. Lanzara, Journal of Physics and Chemistry of Solids **67**, 2172 (2006).

[39] J. M. Dawlaty, S. Shivaraman, J. Strait, P. George, M. Chandrashekhar, F. Rana, M. G. Spencer, D. Veksler, and Y. Chen, Applied Physics Letters **93**, 131905 (2008).

[40] S. Tanuma, C. J. Powell, and D. R. Penn, Surf. Interface Anal. **37**, 1 (2005).

[41] E. D. Palik, *Handbook of optical constants of solids* (Academic Press, Orlando, 1985).

[42] F. Tuinstra and J. Koenig, J. Chem. Phys. **53**, 1126 (1970).

[43] A. Ferrari and J. Robertson, Physical Review B **61**, 14095 <last_page> 14107 (2000).

[44] B. Hornetz, H. Michel, and J. Halbritter, J. Mater. Res. **9**, 3088 (1994).

[45] P. J. Cumpson, Surf. Interface Anal. **29**, 403 (2000).

[46] J. Burton, L. Sun, F. Long, Z. Feng, and I. Ferguson, Physical Review B **59**, 7282 (1999).

[47] I. Meric, C. R. Dean, A. F. Young, N. Baklitskaya, N. J. Tremblay, C. Nuckolls, P. Kim, and K. L. Shepard, Nano Lett. **11**, 1093 (2011).

[48] S. Kim, J. Nah, I. Jo, D. Shahrjerdi, L. Colombo, Z. Yao, E. Tutuc, and S. K. Banerjee, Appl. Phys. Lett. **94**, 062107 (2009).

[49] S. Shivaraman, R. A. Barton, X. Yu*, et al*, Nano Letters **9**, 3100 (2009).

[50] A. Sakhaee-Pour, M. T. Ahmadian, and A. Vafai, Solid State Commun. **145**, 168 (2008).

[51] J. L. Weyher, S. Lazar, J. Borysiuk, and J. Pernot, physica status solidi (a) **202**, 578 (2005).

[52] J. S. Shor and A. D. Kurtz, J. Electrochem. Soc. **141**, 778 (1994).

[53] M. Kato, M. Ichimura, E. Arai, and P. Ramasamy, Japanese Journal of Applied Physics **42**, 4233 (2003).

[54] J. S. Shor, A. D. Kurtz, I. Grimberg, B. Z. Weiss, and R. M. Osgood, J. Appl. Phys. **81**, 1546 (1997).

[55] X. Yu, *Novel free standing graphene membrane and photoelectrochemical etching of SiC*, Master's thesis, Cornell University (2008).

[56] D. H. van Dorp and J. J. Kelly, J Electroanal Chem **599**, 260 (2007).

[57] S. Rysy, H. Sadowski, and R. Helbig, Journal of Solid State Electrochemistry **3**, 437 (1999).

[58] N. Ferralis, R. Maboudian, and C. Carraro, Phys. Rev. Lett. **101**, 156801 (2008).

[59] K. N. Kudin, B. Ozbas, H. C. Schniepp, R. K. Prud'homme, I. A. Aksay, and R. Car, Nano Letters **8**, 36 (2008).

[60] N. Mounet and N. Marzari, Phys.Rev.B **71**, 205214 (2005).

[61] B. Ilic, S. Krylov, K. Aubin, R. Reichenbach, and H. G. Craighead, Appl. Phys. Lett. **86**, 193114 (2005).

[62] J. S. Bunch, *Mechanical and electrical properties of graphene sheets*, Ph.D. Dissertation, Cornell University (2008).

[63] S. Timoshenko, D. H. Young, and W. Weaver, *Vibration problems in engineering* (Wiley, New York, 1974).

[64] I. W. Frank, D. M. Tanenbaum, A. M. v. d. Zande, and P. L. McEuen, J. Vac. Sci. Technol. B **25**, 2558 (2007)

[65] J. T. Robinson, M. Zalalutdinov, J. W. Baldwin, E. S. Snow, Z. Wei, P. Sheehan, and B. H. Houston, Nano Letters **8**, 3441 (2008).

[66] M. Ishigami, J. H. Chen, W. G. Cullen, M. S. Fuhrer, and E. D. Williams, Nano Letters **7**, 1643 (2007).

[67] S. D. Senturia, *Microsystem design* (Kluwer Academic Publishers, Boston, 2001).

[68] J. D. Whittaker, E. D. Minot, D. M. Tanenbaum, P. L. McEuen, and R. C. Davis, Nano Letters **6**, 953 (2006).

[69] K. L. Ekinci and M. L. Roukes, Rev. Sci. Instrum. **76**, 061101 (2005).

[70] J. Jobst, *Quantum transport in epitaxial graphene on silicon carbide (0001)* Ph.D. Dissertation, Universität Erlangen-Nürnberg (2013).

[71] S. Shivaraman, J. Jobst, D. Waldmann, H. B. Weber, and M. G. Spencer, Phys. Rev. B **87**, 195425 (2013).

[72] A. Bostwick, K. V. Emtsev, K. Horn, E. Huwald, L. Ley, J. L. McChesney, T. Ohta, J. Riley, E. Rotenberg, F. Speck, and T. Seyller, *Photoemission Studies of Graphene on SiC: Growth, Interface, and Electronic Structure* (Springer Berlin Heidelberg, 2008), 47, p. 159.

[73] A. L. Walter, K. Jeon, A. Bostwick*, et al*, Applied Physics Letters **98**, 184102 (2011).

[74] I. Gierz, T. Suzuki, R. T. Weitz*, et al*, Phys. Rev. B **81**, 235408 (2010).

[75] F. Speck, J. Jobst, F. Fromm, M. Ostler, D. Waldmann, M. Hundhausen, H. B. Weber, and T. Seyller, Applied Physics Letters **99**, 122106 (2011).

[76] M. H. Oliveira Jr., T. Schumann, F. Fromm, R. Koch, M. Ostler, M. Ramsteiner, T. Seyller, J. M. J. Lopes, and H. Riechert, Carbon **52**, 83-89 (2013).

[77] K. Lee, S. Kim, M. S. Points, T. E. Beechem, T. Ohta, and E. Tutuc, Nano Letters **11**, 3624 (2011).

[78] S. Tanabe, Y. Sekine, H. Kageshima, and H. Hibino, Japanese Journal of Applied Physics **51**, 02BN02 (2012).

[79] D. H. v. Dorp, J. L. Weyher, and J. J. Kelly, J Micromech Microengineering **17**, S50 (2007).

[80] K. Rajeshwar, *Fundamentals of Semiconductor Electrochemistry and Photochemistry* (Wiley-VCH, Weinheim; [Cambridge], 2002), 6, p. 6-8.

[81] S. Datta, *Electronic transport in mesoscopic systems* (Cambridge University Press, Cambridge, UK; New York, 1997).

[82] J. W. McClure, Phys.Rev. **104**, 666 (1956).

[83] E. McCann and V. I. Fal'ko, Phys. Rev. Lett. **96**, 086805 (2006).

[84] L. D. Landau and E. M. Lifshitz, *Quantum Mechanics Non-Relativistic Theory Volume 3.* (Elsevier Science, Oxford, 1981).

[85] A. A. Taskin and Y. Ando, Phys.Rev.B **84**, 035301 (2011).

[86] Y. Zhang, Y. W. Tan, H. L. Stormer, and P. Kim, Nature **438**, 201 (2005).

[87] K. S. Novoselov, E. McCann, S. V. Morozov, V. I. Fal'ko, M. I. Katsnelson, U. Zeitler, D. Jiang, F. Schedin, and A. K. Geim, Nature Phys **2**, 177 (2006).

[88] C. Park and N. Marzari, Phys.Rev.B **84**, 205440 (2011).

[89] E. McCann, K. Kechedzhi, V. I. Fal'ko, H. Suzuura, T. Ando, and B. Altshuler, Phys. Rev. Lett. **97**, 146805 (2006).

[90] F. V. Tikhonenko, A. A. Kozikov, A. K. Savchenko, and R. V. Gorbachev, Phys. Rev. Lett. **103**, 226801 (2009).

[91] R. V. Gorbachev, F. V. Tikhonenko, A. S. Mayorov, D. W. Horsell, and A. K. Savchenko, Phys. Rev. Lett. **98** (2007).

[92] K. Kechedzhi, V. I. Fal'ko, E. McCann, and B. L. Altshuler, Phys. Rev. Lett. **98**, 176806 (2007).

[93] D. Waldmann, B. Butz, S. Bauer*, et al*, ACS Nano **7**, 4441 (2013).

[94] M. Huang, H. Yan, C. Chen, D. Song, T. F. Heinz, and J. Hone, Proceedings of the National Academy of Sciences **106**, 7304 (2009).

[95] T. M. G. Mohiuddin, A. Lombardo, R. R. Nair*, et al*, Phys. Rev. B **79**, 205433 (2009).

[96] W. Zhao, P. H. Tan, J. Liu, and A. C. Ferrari, Journal of the American Chemical Society **133**, 5941 (2011).

[97] M. A. Pimenta, G. Dresselhaus, M. S. Dresselhaus, L. G. Cancado, A. Jorio, and R. Saito, Phys. Chem. Chem. Phys. **9**, 1276 (2007).

[98] X. Dong, Y. Shi, Y. Zhao*, et al*, Phys. Rev. Lett. **102**, 135501 (2009).

[99] L. M. Malard, D. C. Elias, E. S. Alves, and M. A. Pimenta, Phys. Rev. Lett. **101**, 257401 (2008).

[100] J. Yan, T. Villarson, E. A. Henriksen, P. Kim, and A. Pinczuk, Phys. Rev. B **80**, 241417 (2009).

[101] P. Gava, M. Lazzeri, A. M. Saitta, and F. Mauri, Phys. Rev. B **80**, 155422 (2009).

[102] T. Ando and M. Koshino, Journal of the Physical Society of Japan **78**, 034709-034716 (2009).

[103] M. Bruna and S. Borini, Phys. Rev. B **81**, 125421 (2010).

[104] W. Zhao, P. Tan, J. Zhang, and J. Liu, Phys. Rev. B **82**, 245423 (2010).

[105] S. S. Lin, B. G. Chen, C. T. Pan, S. Hu, P. Tian, and L. M. Tong, Applied Physics Letters **99**, 233110 (2011).

[106] A. C. Crowther, A. Ghassaei, N. Jung, and L. E. Brus, ACS Nano **6**, 1865 (2012).

[107] C. Attaccalite, L. Wirtz, M. Lazzeri, F. Mauri, and A. Rubio, Nano Letters **10**, 1172 (2010).

[108] M. Bruna and S. Borini, Phys. Rev. B **83**, 241401 (2011).

[109] N. Kim, K. S. Kim, N. Jung, L. Brus, and P. Kim, Nano Letters **11**, 860 (2011).

[110] K. S. Novoselov, A. K. Geim, S. V. Morozov, D. Jiang, M. I. Katsnelson, I. V. Grigorieva, S. V. Dubonos, and A. A. Firsov, Nature **438**, 197-200 (2005).

[111] J. Jobst, D. Waldmann, F. Speck, R. Hirner, D. K. Maude, T. Seyller, and H. B. Weber, Physical Review B **81**, 195434 (2010).

[112] C. Berger, Z. Song, X. Li*, et al*, Science **312**, 1191 (2006).

[113] K. I. Bolotin, K. J. Sikes, J. Hone, H. L. Stormer, and P. Kim, Phys. Rev. Lett. **101**, 96802 (2008).

[114] A. Jorio, M. M. Lucchese, F. Stavale, and C. A. Achete, physica status solidi (b) **246**, 2689 (2009).

[115] L. Barreto, E. Perkins, J. Johannsen, S. Ulstrup, F. Fromm, C. Raidel, T. Seyller, and P. Hofmann, Appl. Phys. Lett. **102**, 033110 (2013).

[116] S. Shivaraman, L. H. Herman, F. Rana, J. Park, and M. G. Spencer, Appl. Phys. Lett. **100**, 183112 (2012).

[117] S. Tongay, T. Schumann, and A. F. Hebard, Appl. Phys. Lett. **95**, 222103 (2009).

[118] C. Chen, M. Aykol, C. Chang, A. F. J. Levi, and S. B. Cronin, Nano Letters **11**, 1863 (2011).

[119] S. A. Reshanov, K. V. Emtsev, F. Speck, K. Gao, T. K. Seyller, G. Pensl, and L. Ley, physica status solidi (b) **245**, 1369 (2008).

[120] T. Seyller, K. V. Emtsev, F. Speck, K. -. Gao, and L. Ley, Appl. Phys. Lett. **88**, 242103 (2006).

[121] S. Sonde, F. Giannazzo, V. Raineri, R. Yakimova, J. -. Huntzinger, A. Tiberj, and J. Camassel, Phys.Rev.B **80**, 241406 (2009).

[122] S. Tongay, M. Lemaitre, T. Schumann, K. Berke, B. R. Appleton, B. Gila, and A. F. Hebard, Appl. Phys. Lett. **99**, 102102 (2011).

[123] M. Shafiei, P. G. Spizzirri, R. Arsat, J. Yu, J. du Plessis, S. Dubin, R. B. Kaner, K. Kalantar-zadeh, and W. Wlodarski, The Journal of Physical Chemistry C **114**, 13796 (2010).

[124] A. V. Los and M. S. Mazzola, J Electron Mater **30**, 235 (2001).

[125] Rhoderick, E. H., Williams,R.H., *Metal-semiconductor contacts* (Clarendon Press ; Oxford University Press, Oxford [England]; New York, 1988).

[126] A. Itoh, T. Kimoto, and H. Matsunami, Electron Device Letters, IEEE **16**, 280 (1995).

[127] V. G. Bozhkov, N. A. Torkhov, and A. V. Shmargunov, J. Appl. Phys. **109**, 073714 (2011).

[128] S. J. Fonash, J. Appl. Phys. **54**, 1966 (1983).

[129] T. Æ Myrtveit, J. Appl. Phys. **78**, 7170 (1995).

[130] R. T. Tung, Materials Science and Engineering: R: Reports **35**, 1 (2001).

[131] J. H. Werner and H. H. Guttler, J. Appl. Phys. **69**, 1522 (1991).

[132] R. T. Tung, Phys.Rev.B **45**, 13509 (1992).

[133] H. von Wenckstern, G. Biehne, R. A. Rahman, H. Hochmuth, M. Lorenz, and M. Grundmann, Appl. Phys. Lett. **88**, 092102 (2006).

[134] T. Hofmann, A. Boosalis, P. Kuhne, C. M. Herzinger, J. A. Woollam, D. K. Gaskill, J. L. Tedesco, and M. Schubert, Appl. Phys. Lett. **98**, 041906 (2011).

[135] J. L. Tedesco, B. L. VanMil, R. L. Myers-Ward, J. M. McCrate, S. A. Kitt, P. M. Campbell, G. G. Jernigan, J. C. Culbertson, C. R. E. Jr., and D. K. Gaskill, Appl. Phys. Lett. **95**, 122102 (2009).

[136] A. E. Curtin, M. S. Fuhrer, J. L. Tedesco, R. L. Myers-Ward, C. R. E. Jr., and D. K. Gaskill, Appl. Phys. Lett. **98**, 243111 (2011).

[137] R. T. Tung, Phys. Rev. Lett. **52**, 461 (1984).

[138] J. Robinson, X. Weng, K. Trumbull, R. Cavalero, M. Wetherington, E. Frantz, M. LaBella, Z. Hughes, M. Fanton, and D. Snyder, ACS Nano **4**, 153 (2010).

[139] Y. Qi, S. H. Rhim, G. F. Sun, M. Weinert, and L. Li, Phys. Rev. Lett. **105**, 085502 (2010).

[140] C. Casiraghi, S. Pisana, K. S. Novoselov, A. K. Geim, and A. C. Ferrari, Appl. Phys. Lett. **91**, 233108 (2007).

[141] C. Stampfer, F. Molitor, D. Graf, K. Ensslin, A. Jungen, C. Hierold, and L. Wirtz, Appl. Phys. Lett. **91**, 241907 (2007).

[142] G. Nicotra, Q. M. Ramasse, I. Deretzis, A. La Magna, C. Spinella, and F. Giannazzo, ACS Nano **7**, 3045 (2013).

[143] Q. H. Wang, K. Kalantar-Zadeh, A. Kis, J. N. Coleman, and M. S. Strano, Nature Nanotech **7**, 699 (2012).

[144] A. Kuc, N. Zibouche, and T. Heine, Phys. Rev. B **83**, 245213 (2011).

[145] K. F. Mak, C. Lee, J. Hone, J. Shan, and T. F. Heinz, Phys. Rev. Lett. **105**, 136805 (2010).

[146] A. Splendiani, L. Sun, Y. Zhang, T. Li, J. Kim, C. Chim, G. Galli, and F. Wang, Nano Letters **10**, 1271 (2010).

[147] S. Tongay, J. Zhou, C. Ataca, K. Lo, T. S. Matthews, J. Li, J. C. Grossman, and J. Wu, Nano Letters **12**, 5576 (2012).

[148] W. Zhao, Z. Ghorannevis, L. Chu, M. Toh, C. Kloc, P. Tan, and G. Eda, ACS Nano **7**, 791 (2013).

[149] P. Tonndorf, R. Schmidt, P. Böttger*, et al*, Opt.Express **21**, 4908 (2013).

[150] M. M. Benameur, B. Radisavljevic, J. S. Héron, S. Sahoo, H. Berger, and A. Kis, Nanotechnology **22**, 125706 (2011).

[151] C. Lee, H. Yan, L. E. Brus, T. F. Heinz, J. Hone, and S. Ryu, ACS Nano **4**, 2695 (2010).

[152] A. Molina-Sánchez and L. Wirtz, Phys.Rev.B **84**, 155413 (2011).

[153] A. M. van der Zande, P. Y. Huang, D. A. Chenet, T. C. Berkelbach, Y. You, G. Lee, T. F. Heinz, D. R. Reichman, D. A. Muller, and J. C. Hone, Nature Materials **12**, 554 (2013).

[154] M. K. Edward McCann and, Reports on Progress in Physics **76**, 056503 (2013).

[155] F. Wang, Y. Zhang, C. Tian, C. Girit, A. Zettl, M. Crommie, and Y. R. Shen, Science **320**, 206 (2008).

[156] Y. Zhang, T. Tang, C. Girit, Z. Hao, M. C. Martin, A. Zettl, M. F. Crommie, Y. R. Shen, and F. Wang, Nature **459**, 820 (2009).

[157] E. V. Castro, K. S. Novoselov, S. V. Morozov, N. M. R. Peres, J. M. B. L. dos Santos, J. Nilsson, F. Guinea, A. K. Geim, and A. H. C. Neto, Phys. Rev. Lett. **99**, 216802 (2007).

[158] K. F. Mak, C. H. Lui, J. Shan, and T. F. Heinz, Phys. Rev. Lett. **102**, 256405 (2009).

[159] J. Yan, M. Kim, J. A. Elle, A. B. Sushkov, G. S. Jenkins, H. M. Milchberg, M. S. Fuhrer, and H. D. Drew, Nature Nanotech **7**, 472 (2012).

[160] T. Stauber, N. M. R. Peres, and A. K. Geim, Phys.Rev.B **78**, 085432 (2008).

[161] Z. H. Ni, H. M. Wang, J. Kasim, H. M. Fan, T. Yu, Y. H. Wu, Y. P. Feng, and Z. X. Shen, Nano Letters **7**, 2758 (2007).

[162] D. S. L. Abergel, A. Russell, and V. I. Fal'ko, Appl. Phys. Lett. **91**, 063125 (2007).

[163] T. Taychatanapat and P. Jarillo-Herrero, Phys. Rev. Lett. **105**, 166601 (2010).

[164] P. Y. Huang, C. Ruiz-Vargas, A. M. van der Zande*, et al*, Nature **469**, 389 (2011).

[165] R. V. Gorbachev, I. Riaz, R. R. Nair*, et al*, Small **7**, 465 (2011).